Cortical bone characterization using guided wave ultrasonography

by

Tho Nguyen Hoang Thi TRAN

A thesis submitted in partial fulfillment of the requirements for the degree of

Doctor of Philosophy

Medical Sciences - Radiology and Diagnostic Imaging

University of Alberta

Abstract

Osteoporosis is currently the most common metabolic musculoskeletal disease which causes brittle bones with a consequent increase in bone fragility and susceptibility to fracture. This "silent epidemic" is mainly characterized by the loss of bone mass, micro-structural deterioration, and cortical thinning, resulting in changes to the mechanical properties of bone. The disease has significant morbidity and mortality affecting over 200 million people throughout the world, especially the elderly and post-menopausal women. The prevalence of osteoporosis and osteoporotic fractures rises up exponentially with the rapid growth of the aged population, which significantly increases the associated health-care costs. Due to the serious impact of osteoporosis and its related fractures on the quality of life, there is a huge call for reliable diagnostic approaches to assess osteoporosis and the fracture risk.

Dual-energy X-ray absorptiometry (DXA) is today the gold standard to measure bone mineral density (BMD) for osteoporosis assessment. The technique is based on photon absorptiometry to measure the attenuation of photon energy by different tissues using X-ray source. DXA exposes patients to ionizing radiation and only measures bone mass thus is incapable of providing the bone mechanical properties, most notably elastic parameters, which are important determinants of bone quality especially in the early stage of osteoporosis.

Ultrasound is an indispensable imaging modality to study soft tissues in diagnostic radiology. The use of ultrasound to study hard tissues is not yet common. But over the last two decades, the idea of using quantitative ultrasound to characterize bone properties has been evolving. Ultrasound has the merits over the other medical imaging modalities because it is portable, cost-effective, lack of ionizing radiation, and sensitive to the mechanical stiffness of cortical bones. Particularly, axial transmission ultrasonography (ATU) has shown great potential to be a non-invasive diagnostic tool to evaluate cortical thinning at multiple peripheral skeletal sites, e.g. radius and tibia. ATU excites ultrasonic guided waves (UGW) propagating in bone. Guided wave techniques have been successfully used in non-destructive testing (NDT) to study waveguide structures such as plates, cylinders, and pipes. Quantitative guided wave ultrasonography (GWU) is attractive because of the

sensitivity of guided waves to the geometric, architectural, and material properties of the cortex. The cortex of long bones is a hard tissue layer bounded above and below by soft tissue and marrow, resulting in high impedance contrast interfaces, and therefore is a natural waveguide for ultrasonic energy to propagate.

The aim of this thesis is to develop a model-based inversion scheme for parametric characterization of cortical bone tissues. The dispersion inversion problem is formulated in the frequency-phase velocity domain. The developed algorithm extracts cortical thickness and elastic velocities from the multi-frequency UGW signals and is applied to numerical simulation data, *ex-vivo* bone phantom data, and *in-vivo* human data.

To image the dispersive energy of UGW, a sparsity-promoting Radon transform method is implemented. This signal processing technique not only provides high-resolution dispersion map but also can be used for signal-to-noise ratio (SNR) enhancement, wave field filtering, and guided mode extraction.

In order to simulate the velocity dispersion of UGW, semi-analytical finite element (SAFE) method is used. The formulation works fine for both free and immersed solid media. The dispersion curves of the UGW propagating in cortical bone coupled with soft tissues can be accurately computed. This work is the first in the bone ultrasound research community to consider a multi-layered long bone model with the cortex surrounded by soft tissues.

To solve the nonlinear inverse problem, the grid search technique is chosen. It simultaneously reconstructs the cortical thickness and compression and shear wave speeds in the bone from UGW data. The inversion scheme is validated based on the combination of numerical and experimental benchmark tests and is subsequently applied to *in-vivo* bone data.

In conclusion, this research demonstrates that using guided wave ultrasonography to characterize osteoporotic cortical thinning is feasible. The cortical properties can be inverted reliably from UGW signals to assess the bone health status and osteoporotic fracture risk prediction. This study increases our fundamental understanding of ultrasound interaction of bone tissue under the impact of the overlying soft tissue and the governing physical principles involved.

Preface

This thesis is an original work by Tho N.H.T. Tran. The research project, of which this thesis is a part, received research ethics approval from the University of Alberta - Health Research Ethics Board, Project Name "Using ultrasound to study bone quality", No. Pro00047967, 2015.

Portions of the material in this thesis can be found in the following papers:

1. Lawrence H. Le, **Tho N.H.T. Tran**, Dean Ta. *Ultrasonic guided waves in long bones: a decade of advancement*, IEEE Access, 2019 (internal review).

2. **Tho N.H.T. Tran**, Mauricio D. Sacchi, Dean Ta, Vu-Hieu Nguyen, Edmond Lou, Lawrence H. Le. *Nonlinear inversion of ultrasonic dispersion curves for cortical bone thickness and elastic velocities*, Annals of Biomedical Engineering, 2019 (accepted, available online:https://doi.org/10.1007/s10439-019-02310-4).

3. **Tho N.H.T. Tran**, Lawrence H. Le, Mauricio D. Sacchi, Vu-Hieu Nguyen. *Sensitivity analysis of ultrasonic guided waves propagating in trilayered bone models: a numerical study*, Biomechanics and Modeling in Mechanobiology, Vol. 17, pp. 1269-1279, 2018.

4. Vu-Hieu Nguyen, **Tho N.H.T. Tran**, Mauricio D. Sacchi, Salah Naili, Lawrence H. Le. *Computing dispersion curves of elastic/viscoelastic transversely-isotropic bone plates coupled with soft tissue and marrow using semi-analytical finite element (SAFE) method*, Computers in Biology and Medicine, Vol. 87, pp. 371-381, 2017.

5. **Tho N.H.T. Tran**, Kim-Cuong T. Nguyen, Mauricio D. Sacchi, Lawrence H. Le. *Imaging ultrasonic dispersive guided wave energy in long bones using linear Radon transform*, Ultrasound in Medicine and Biology, Vol. 40, No. 11, pp. 2715-2727, 2014.

6. **Tho N.H.T. Tran**, Lawrence H. Le, Mauricio D. Sacchi, Vu-Hieu Nguyen, Edmond H.M. Lou. *Multichannel filtering and reconstruction of ultrasonic guided wave fields*

using time intercept-slowness transform, Journal of the Acoustical Society of America, Vol.136, No.1, pp. 248-259, 2014.

7. **Tho N.H.T. Tran**, Lauren Stieglitz, Yu J. Gu, Lawrence H. Le. *Analysis of ultrasonic waves propagating in a bone plate over a water half-space with and without overlying soft tissue*, Ultrasound in Medicine and Biology, Vol. 39, No. 12, pp. 2422-2430, 2013.

In the aforementioned publications, Tho N.H.T. Tran was responsible for designing and programming the algorithms, preparing data examples, and writing the manuscripts. Dr. Le was involved in the originality of the ideas and formulation of concept, research direction, manuscript drafting and editing. Dr. Sacchi advised on signal processing, inversion techniques, statistical validation, and manuscript editing. Dr. Lou advised on equipment and clinical aspect of the project.

Submission of additional papers is planned related to Chapter 5 Dispersion Curve Inversion.

This thesis is dedicated to my families, mentors, friends, and those who read it, and in memory of my grandparents.

Acknowledgements

The completion of this thesis is thanks in large part to the people who have supported academically, financially, and practically.

The author would like to express thanks to Department of Radiology and Diagnostic Imaging and Department of Physics, University of Alberta for offering me the opportunity to research at Ultrasonic Visualization, Imaging & Characterization Lab. I feel fortunate to be able to do what I do within the group.

I would like to acknowledge Alberta Innovates - Technology Futures (AITF) and the generous supporters of Lois Hole Hospital through Women and Children's Health Research Institute (WCHRI) for the graduate studentships.

I am privileged to have worked with the committee members Dr. Lawrence H. Le, Dr. Mauricio D. Sacchi, and Dr. Edmond Lou. These mentors brought a depth of knowledge that few could match. I am very grateful to them for supporting this project and giving such thoughtful feedback, always aimed at moving me forward.

I would like to express my deepest gratitude towards my supervisor, Dr. Lawrence H. Le, for his patient guidance, leading advices, and encouragements. Throughout this work Dr. Le helped me develop independent thinking and research skills. I have learned a great deal of knowledge, skills, and experiences from Dr. Le and all of them will serve useful to my academic career ahead.

I gratefully appreciate Dr. Mauricio D. Sacchi with whom I enjoyed discussing problems and sharing ideas. I always learn something new, interesting, and immediately applicable to my research from Dr. Sacchi. I believe not all professors spend time writing computer codes side-by-side with students like Dr. Sacchi.

Dr. Edmond Lou is very knowledgeable about ultrasonic data acquisition systems and clinical trials. I owe my sincere thank to Dr. Lou for his support, guidance, and stimulating discussions throughout my study.

The author would like to take this opportunity to thank other scholars who have done work which was pivotal in the dissertation's development: Dr. Dean Ta (Department of

Electronic Engineering, Fudan University), Dr. Vu-Hieu Nguyen (Université Paris Est), Dr. Jeff Gu (Department of Physics, University of Alberta), Dr. Jacob Jaremko (Department of Radiology and Diagnostic Imaging, University of Alberta), and Dr. Luning Wang (Department of Materials Science and Engineering, University of Science and Technology Beijing). Their scientific advice and suggestions made a great contribution in the preparation of this thesis.

Thank you, also, to Dr. Kumaradevan Punithakumar, Dr. Alan Wilman, and Dr. Lei Zhang for serving in the examination committee of my dissertation as well as for their insightful comments and healthy criticism.

My gratitude also goes to Carol Rae, Ken Leung, Mary Lou, Lynda Loiseau, and Holly O'Kurly for their kind assistance in administration matters.

It has been a blessing to work alongside passionate and talented colleagues: Dr. Rui Zheng, Dr. Wei Chen, Lauren Stieglitz, Dr. Nhat-Quang Vo, Kim-Cuong T. Nguyen, Reham Kaifi, Thanh-Tu Pham, Phuong-Thuy T. Nguyen, and Mahdieh Khodaei. I am grateful to their help during my study and all the fun we have had together. A special acknowledgment goes to Dr. Rui Zheng, currently Assistant Professor in the ShanghaiTech University of Technology's School of Information Science and Technology, for teaching me many aspects of the experiment protocols.

Hard days are little more bearable with good friends. Special thanks go to my friends Denis J. Blakeman, Mineko Fujikura, Duc Vu Nguyen, Phuong Nguyen, Duy Ha Ly, Hanh-Thuc Tran, and Minh-Ly Nguyen, among others, for all encouraging conversations and good times we've shared.

Last, but certainly not the least, I would not be where I am without the endless love and support from my families, June, and my beloved 4-legged companion Skye. You fill my world with your joy and love. Thank you for always being there for me!

Contents

List of Figures

List of Tables

List of Abbreviations

2D	Two-dimensional
3D	Three-dimensional
μCT	Micro-computed tomography
AIB	Apparent integrated backscatter
ARP	Adjoint Radon panel
ART	Adjoint Radon transform
ATU	Axial transmission ultrasound/ultrasonography
BMD	Bone mineral density
BUA	Broadband ultrasonic attenuation
BUB	Broadband ultrasonic backscatter
CT	Computed tomography
DXA	Dual energy X-ray absorptiometry
DLS	Damped least-squares
ESPRIT	Estimation of signal parameters via rotational invariance technique
FAS	First arriving signal
FDTD	Finite-difference time-domain
FEM	Finite element method
FT	Fourier transform
FFT	Fast Fourier transform
FP	Fourier panel
FSAB	Frequency slope of apparent backscatter
FWHM	Full-width at half-maximum
GPR	Ground penetrating radar
GVF	Group velocity filtering
GWU	Guided wave ultrasonography

HFHV	High-frequency and high-velocity
HR-pQCT	High-resolution peripheral quantitative computer tomography
HRRT	High-resolution Radon transform
HS	High speed
IRLS	Iteratively re-weighted least-squares
JADE	Joint approximate diagonalization of eigen-matrices algorithm
JSSRE	Joint spectrogram segmentation and ridge-extraction
L-BFGS	Limited-memory Broyden-Fletcher-Goldfarb-Shanno method
LFLV	Low-frequency and low-velocity
LS	Low speed
LSRT	Least-squares Radon transform
MRI	Magnetic resonance imaging
MUSIC	Multiple signal classification
MVM	Minimum variance method
NDT	Non-destructive testing
pQCT	Peripheral quantitative computed tomography
PSD	Power spectral density
PV	Phase velocity
QGWU	Quantitative guided wave ultrasonography
QUS	Quantitative ultrasound
RT	Radon transform
SAFE	Semi-analytical finite element
SFEM	Spectral finite element method
SNR	Signal-to-noise ratio
SOS	Speed of sound
STFT	Short time Fourier transform
SVD	Singular value decomposition
TGC	Time gain compensation
TI	Transversely-isotropic
UGM	Ultrasonic guided modes
UGW	Ultrasonic guided waves
WDR	Wideband dispersion reversal

Chapter 1

Introduction

1.1 Motivation

Osteoporosis is a serious medical condition that changes bone tissue structure and composition, and impairs the mechanical strength of bone leading to the increased risk of fractures. How do you know if you have osteoporosis or if you are at risk? Early detection and monitoring of osteoporosis mainly rely on dual-energy X-ray absorptiometry, though in recent years bone quantitative ultrasound has gained attention for its ability to detect bone fragility. Although X-ray absorptiometry is successful in measuring bone mineral content, it cannot determine bone micro-structures and elasticity, which are important factors of bone strength.

Quantitative ultrasound has become widely applied to study bone properties over the last two decades. Ultrasonic imaging is cost effective, portable, and ionizing radiation-free therefore has an excellent safety record. Additionally, ultrasonography uses mechanical waves that are more sensitive to the physical properties of bone (e.g., elasticity, absorption, cortical thickness, micro-architecture, density) than absorptiometry. Axial transmission ultrasound (ATU) has shown great potential to be a non-invasive tool to characterize cortical bones at multiple peripheral skeletal sites, e.g. radius and tibia (Moilanen, 2008). The ATU technique was first introduced to monitor bone fracture healing (Anast *et al.*, 1958). The ATU acquisition configuration requires the transmitters and receivers to be placed on the same side of the investigated skeletal site and measures the ultrasound signals traveling over a known distance along the bone axis. The cortical bone is a hard tissue layer surrounded by soft tissues, resulting in high impedance contrast interfaces, and therefore is a strong natural waveguide for ultrasound to propagate and build up guided wave energy. Ultrasonic guided waves (UGW) have been successfully used in non-destructive testing and structural health monitoring to characterize complex waveguide structures such as plates, cylinders, and pipes

(Rose, 2014). Quantitative guided wave ultrasonography is particularly attractive because of the sensitivity of UGW propagation characteristics to the geometric, architectural, and material properties of the cortex.

In NDT and geophysics, inversion of surface or guided wave energy for material properties and geological structures is a widely-studied topic. However research on extracting bone parameters such as thickness and elastic constants using inverse theory is still rare. There are only a handful of published studies on this topic in the last couple of years. An understanding of the context of this work leads to the realization that currently there are knowledge gaps of UGW propagation in hard biological tissues like cortical bones. One challenge in the analysis of guided waves traveling in long bones is the presence of overlying soft tissues due to the lack of computational methods that are able to accurately describe the dispersion phenomena of waves in a coupled soft tissues-cortical bone system. Because guided waves are sensitive to cortical boundaries, the soft-tissue layer can affect mode generation and alter the dispersive characteristics of guided modes. The modeling of UGW propagation in the multi-layered waveguide such as cortex coupled with soft tissues has been a long-standing problem for ATU's clinical application. In the published studies from literature, the long bone is usually described as free plate model for modeling purposes to fit the experimental data. Our knowledge about the impact of soft tissue on ultrasound bone data is still limited. In order to anticipate successful application of quantitative ultrasound in bone assessment, we must have a solid understanding of the governing physical principles involved. The motivation of this doctoral work is to develop an acoustic characterization method for long cortical bones with soft-tissue coupling effect taken into account. Through the end, the research is expected to provide substantial knowledge, methodologies, and evidence to advance the application of guided wave ultrasound in bone quality assessment.

1.2 Scope of the Thesis

The objectives of this thesis are to:

- develop sparsity-promoting signal processing algorithms to image ultrasonic energies propagating in long cortical bones with high resolution thus providing a more accurate interpretation of bone data,
- develop a forwarding modeling tool to simulate the ultrasonic dispersion in multi-layered long bone models to study the dispersion, attenuation, and particle motions of the guided modes,

- develop model-based inversion or optimization techniques for a reliable estimation of cortical thickness and elastic velocities from ultrasonic guided wave signals,
- validate the developed techniques using numerically simulated signals.
- apply the developed techniques to *ex-vivo* and *in-vivo* datasets.

1.3 Overview of the Thesis

This thesis contains 6 chapters organized as follows.

- In this Chapter 1, the motivation and the objectives of this research are described.
- Chapter 2 introduces the background of bone tissues, osteoporosis disease, and different medical imaging modalities used for osteoporosis diagnosis. A comprehensive literature review on bone guided wave ultrasonography is also reported.
- Chapter 3 describes signal processing methods to extract dispersion characteristics from guided wave data with numerical simulation, *ex-vivo*, and *in-vivo* examples.
- In Chapter 4, semi-analytical finite element method is implemented to calculate the dispersion curves of ultrasonic waves propagating in long bone models. There is also the sensitivity analysis of of ultrasonic guided waves to cortical properties.
- Chapter 5 presents the inversion studies on the simulation, *ex-vivo*, and *in-vivo* measurements.
- Finally, in Chapter 6, the contributions and limitations of this work, and recommendations for future research directions are discussed.

Chapter 2

Background

2.1 Bone and Osteoporosis

Bones are rigid organs that making up the skeleton in humans. The adult human skeleton consists of over 200 bones to provide the body's structural framework, protect the various organs of the body, and produce red and white blood cells and store minerals (Chiras, 2013). Bone is a living tissue and is constantly remodeled throughout life. Bone is a composite material consisting of an inorganic and an organic phase. By weight, approximately 60% of the tissue is inorganic matter, 8-10% is water, and the remainder is organic matter. By volume, these proportions are approximately 40%, 25%, and 35% respectively. The inorganic phase is an impure form of hydroxyapatite, which is a naturally occurring calcium phosphate. The organic phase is composed predominantly (98% by weight) of type I collagen and a variety of noncollagenous proteins, and cells make up the remaining 2% of this phase (Marcus *et al.*, 2008). Bones are classified on the basis of their shape rather than according to size. Five classes can be identified: long bones (e.g. femur, tibia, radius, humerus), short bones (e.g. carpals, tarsals), flat bones (e.g. skull, ribs, sternum), irregular bones (e.g. vertebrae, pelvis), and sesamoid bones (e.g. patella). Anatomically, two types of bone are found in the body: the cortical and trabecular bone (Figure 2.1). Cortical bone is dense and compact. It forms the outer layer of the bone. Trabecular or cancellous bone makes up the inner layer of the bone and has a spongy, honeycomb-like structure (Chiras, 2013).

Osteoporosis is the most common metabolic bone disease in which the density and quality of bone are reduced. The disease occurs when there is a deterioration of bone tissues and causes mineral density loss of both trabecular and cortical components. The latter is caused by the process of trabecularization, which increases cortical porosity and subsequent decreases cortical thickness. As the bones become thinner and more porous, the risk of fractures is significantly increased (Werner, 2005). Figure 2.2 displays the comparison

of normal bone and bone weakened by osteoporosis. The bone quality loss occurs "silently", painlessly, and progressively. Often there are no symptoms until the first fracture occurs.

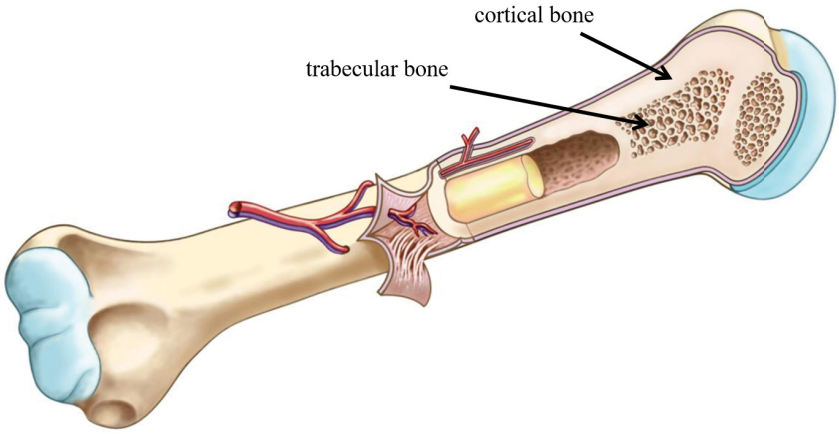

Figure 2.1: Two types of bone tissue: cortical and trabecular/cancellous bone (Docstoc, 2012).

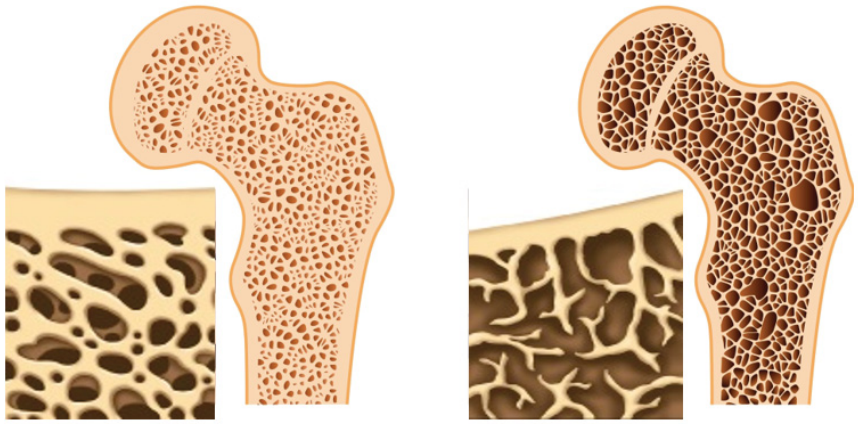

Figure 2.2: (a) Healthy bone versus (b) bone weakened by osteoporosis (modified from PharmacyPedia, 2018).

Osteoporosis is a wide-spread systemic disorder of the skeleton which raises a significant challenge to health care systems worldwide. Osteoporosis affects up to 15.8% of women and 6.6% of men over the age of 50 years (Tenenhouse *et al.*, 2000). The rate of bone loss is greater in women than men with women experiencing accelerated bone loss following menopause. The disease however can strike at any age. The most common fractures associated with osteoporosis occur at the hip, spine, and wrist (World Health Organisation, 1994). Globally, the number of hip fractures has been estimated to be approximately 2.6 million by the year 2025 and 4.5 million by the year 2050. Asia has been predicted to bear most

of this burden. The projected incidence of hip fracture in this region will account for 37% of all hip fractures by 2025 and 45% by 2050. The worldwide incidence of hip fracture is projected to increase by 310% in men and 240% in women (Gullberg *et al.*, 1997).

In Canada, as many as 2 million people suffer from osteoporosis. Osteoporotic fractures are more common than heart attack, stroke, and breast cancer combined. 30,000 Canadians have hip fractures every year (Leslie *et al.*, 2010). Annually, the cost to the Canadian health care systems of treating osteoporosis and the fractures it causes is at presence estimated to be $1.9 billion. Long term, hospital and chronic care account for the majority of these costs. These costs will likely rise due to the increasing proportion of senior citizens in the population. The annual economic impact of hip fractures is projected to rise to $2.4 billion annually by 2041 (Wiktorowicz *et al.*, 2001). Osteoporotic hip fractures even consume more hospital bed days than stroke, heart attack, and diabetes (Osteoporosis Canada, 2018). The increasing prevalence of osteoporosis will lead to increased socioeconomic burdens of the high cost of treatment. Early detection and prevention strategies are urgent needs to minimize the effect of osteoporosis.

2.2 Diagnosis of Osteoporosis

Osteoporosis is typically diagnosed with a bone density test. The bone scan results show how susceptible an individual's bones are to fracture. Two main types of technologies are currently available to assess bone quality: the ionizing radiation techniques including dual energy X-ray absorptiometry (DXA) and peripheral quantitative computed tomography (pQCT); and the non-ionizing techniques including magnetic resonance imaging (MRI) and quantitative ultrasound (QUS).

DXA is presently the gold-standard and most common clinical method to measure mineral content of bone and provides reliable information to identify individuals most likely to have osteoporosis (World Health Organisation, 1994). The technique is based on photon absorptiometry to measure the attenuation of photon energy by different tissues and uses X-ray as the source of photon energy. DXA is most often performed on femoral neck (the top of the femur), lumbar spine (in the lower back), and hip. As one lies on a platform, the mechanical arm containing an X-ray source, which passes over the body, is aligned with the detector below the body (Figure 2.3). Bone mineral density (BMD) measured by DXA, which is related to the amount of mineral in a specific bone site per scanned area or volume (g/cm^2 or g/cm^3), is an indirect indicator of osteoporotic fracture risk. Generally, the higher the mineral content, the denser the bone is and the less likely it is to fracture.

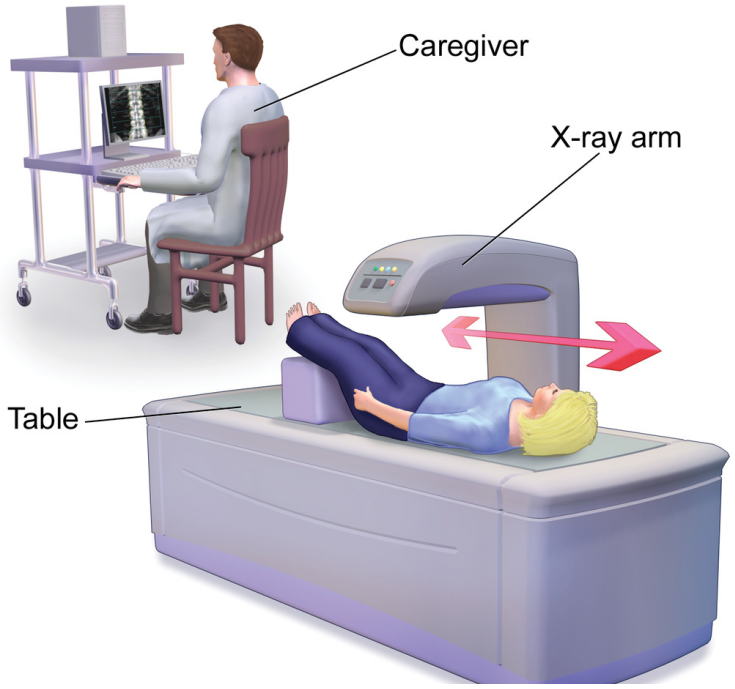

Figure 2.3: DXA bone densitometry scan (Wikipedia, 2018).

pQCT uses X-ray source to perform computed tomography and provides a three-dimensional (3D) measurement of bone density on the periphery of the skeleton such as the wrist (World Health Organisation, 1994). Although this densitometer is more portable than DXA, it is less accurate at predicting fracture risk. Moreover the procedure takes longer scanning time and produces a higher radiation dose.

The shortcomings of the radiation-based techniques are the radiation exposure, the cost of the equipment setup for routine use, and limited portability. Moreover, these techniques only measure bone mass and are incapable of providing the bone mechanical properties, most notably elastic parameters, which are important biomarkers of bone quality especially in the early stage of osteoporosis.

MRI is also used to visualize trabecular bone and assess skeletal strength and integrity. The scanner uses magnetic field to detect the radiofrequency signals from the excited hydrogen protons. However, MRI cannot delineate the bone well because the bone minerals are lack of free protons and thus cannot generate signals while the adjacent tissues (soft tissue and marrow) contain plentiful free protons and produce strong signals. In addition, MRI scanners are costly to purchase, operate, and maintain.

Bone sonometry is a rapidly evolving technology for osteporosis diagnosis in recent years. It uses high-frequency sound waves and, therefore, has the potential to reflect material,

mechanical and structural properties. These properties are very important in bone and osteoporosis assessment. Moreover, ultrasonic testing is non-invasive, cost effective, portable for widespread use in osteoporosis screening programs, and lack of exposure to ionizing radiation.

2.3 Bone Quantitative Ultrasound

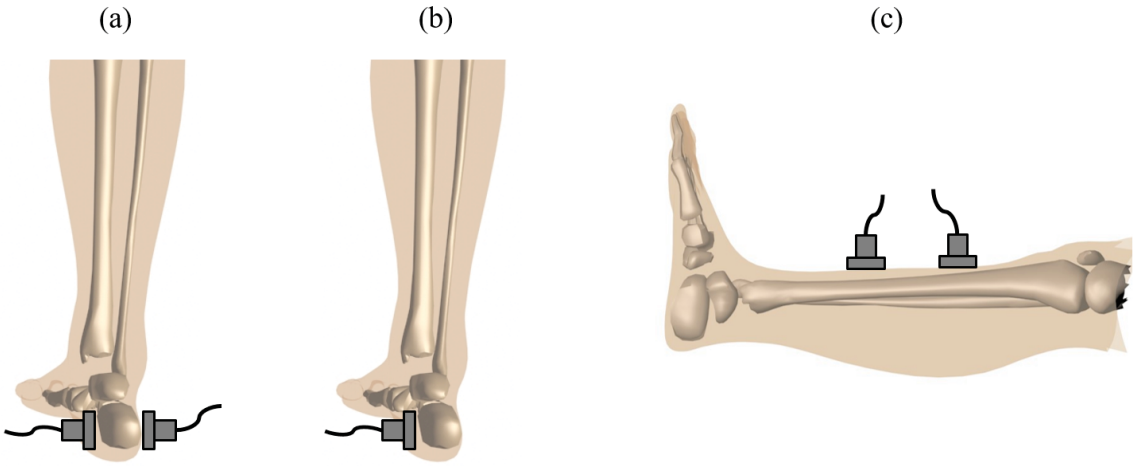

Figure 2.4: Bone quantitative ultrasound: (a) transverse transmission, (b) backscatter, and (c) axial transmission techniques.

The application of ultrasound in clinical diagnosis of osteoporosis was firstly proposed by Langton in 1984 (Langton and Njeh, 2008). The approach uses transverse transmission technique to characterize calcaneus trabecular bone (Figure 2.4a). In this technique, two broadband ultrasonic transducers are used, one transmitter and one receiver, facing each other on each side of the skeletal site to be tested. The broadband ultrasonic attenuation (BUA) of the ultrasound beam through the cancellous bone is measured by a subtraction of the ultrasonic spectra obtained with and without the cancellous bone in position. Langton's work has shown the frequency dependence phenomenon of ultrasonic attenuation in bone and this frequency dependence of osteoporotic bone differs from healthy bone. The transmitted signals through heel bone could discriminate osteoporotic from normal bones. The technique has now been successfully commercialized to quantitatively assess calcaneous by measuring the ultrasound speed and attenuation of the transmitted signal, e.g. Sahara® bone sonometer of Hologic and QRT® 250 Heel Scanner of Cyberlogic Inc. (Langton and Njeh, 2008). However, there are a number of potential sources of error that affect BUA

measurement in transverse transmission technique, including diffraction, interface losses, and phase cancellation.

Instead of using the transmitted signal, ultrasonic backscatter technique (Figure 2.4b) uses pulse-echo to probe the internal structure of cancellous bone with a single transducer to both transmit and receive ultrasonic signals. This allows access to clinically interesting sites such as hip and spine. The backscattering method may offer a useful tool for detecting changes in trabecular bone caused by osteoporosis. The principle of this technique is to measure the power difference between two portions of an ultrasonic backscatter signal. Several studies have demonstrated that the backscatter signal and parameters such as apparent integrated backscatter (AIB) and frequency slope of apparent backscatter (FSAB) have moderate correlations with the density and mechanical characteristics of cancellous bone *in vitro* (Hoffmeister *et al.*, 2012) and *in vivo* (Liu *et al.*, 2016). An ultrasonic backscatter bone diagnostic prototype has recently been developed by Fudan University, Shanghai, China (Liu *et al.*, 2016).

Cortical thickness and elasticity are important determinants of bone strength. Over the last two decades, ultrasonic assessment of long cortical bones using pitch-catch or axial transmission technique has drawn considerable attention. The ATU configuration was first introduced by Anast *et al.*, 1958 to monitor bone fracture healing. The axial acquisition requires the transmitting and receiving transducers to be placed on the same side of the investigated skeletal site and measure the ultrasound signals traveling over a known distance along the long bone axis (Figures 2.4c and 2.5a). The acquisition configuration is equivalent to the single-ended spread in seismic exploration. Ultrasound generated by the emitter will travel through the cortex and be recorded by the receiver. The signals thus acquired carry information about the mechanical characteristics of the cortical bone. At least two companies have marketed ATU-based ultrasound devices to measure sound speed through cortex, e.g. Sunlight Omnisense® 8000S by Sunlight and Oscare Sono® by Oscare Medical. The ATU data is usually presented in a two-dimensional time-offset matrix where offset is the transmitter-receiver distance (Figure 2.5b). The recorded response signals are mainly made up of two types of signals: the strong fast-traveling bulk waves at small offsets (Le *et al.*, 2010) and the slowly-traveling energetic guided waves at far offsets (Moilanen, 2008).

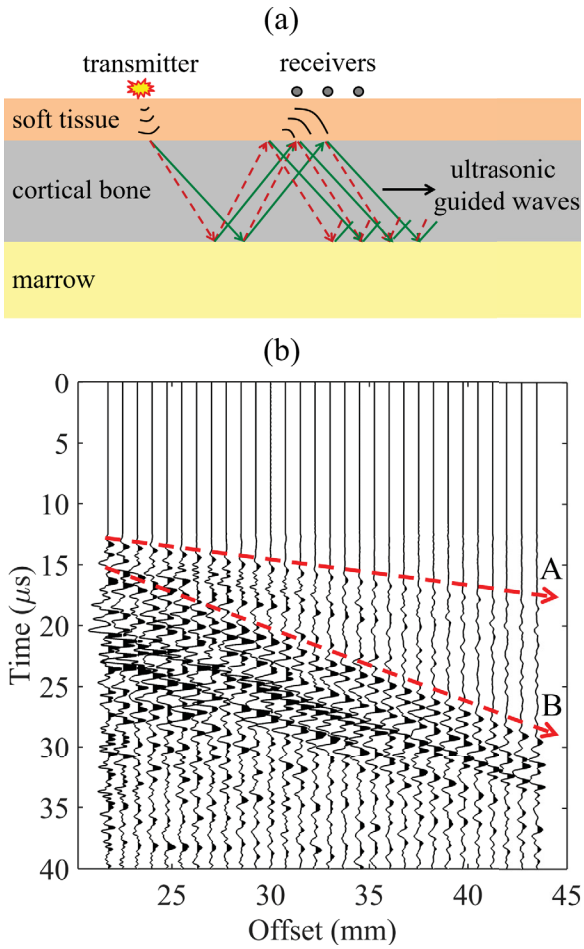

Figure 2.5: (a) Excitation and propagation of ultrasonic guided waves in long cortical bones. (b) The multi-channel time-offset data acquired from an *in-vivo* axial transmission measurement on a human tibia. The recorded signals show two major wave groups with distinct phase speeds, which are typically observed in bone data. The first group is made up of the fast-travelling and high-frequency bulk waves (A). The second group covers the slow-travelling and low-frequency ultrasonic guided waves (B).

2.4 Literature Review on Bone Guided Wave Ultrasonography

2.4.1 Signal Processing

Axial transmission ultrasound excites guided waves traveling in the cortical shells of long bones. Cortex is a hard tissue layer bounded above and below by soft tissues and bone marrow, resulting in high-impedance contrast boundaries, and therefore is a natural dispersive waveguide supporting the propagation of ultrasonic energy (Figure 2.5a). The ultrasonic guided waves are dispersive, i.e. travel with frequency-dependent phase or group velocity, and multi-modal by nature. Regardless of the application, analysis of guided wave signals

fundamentally involves the use of the dispersion curves, which are plots of phase or group velocity versus frequency (Figure 2.6). The velocities of the guided modes are different and are sensitive to the cortical thickness and the elasticity of the propagating medium (Tran *et al.*, 2018*a*). Therefore phase and group velocity dispersion curves possess valuable information about geometrical and elastic properties of the cortical waveguide. The dispersion properties can be used to drive inversion formulation for cortex characteristics. Thus the velocity curve calculation serves as a critical signal processing step and an important area of scientific inquiry. It is also the most active and emerging research topic in the area of cortical bone quantitative ultrasound for the past ten years. This section reviews the recent advances of the methods to analyze UGW signals. The spectral techniques can be categorized into two groups: single-channel and multi-channel analysis that produces group and phase velocity dispersion map respectively.

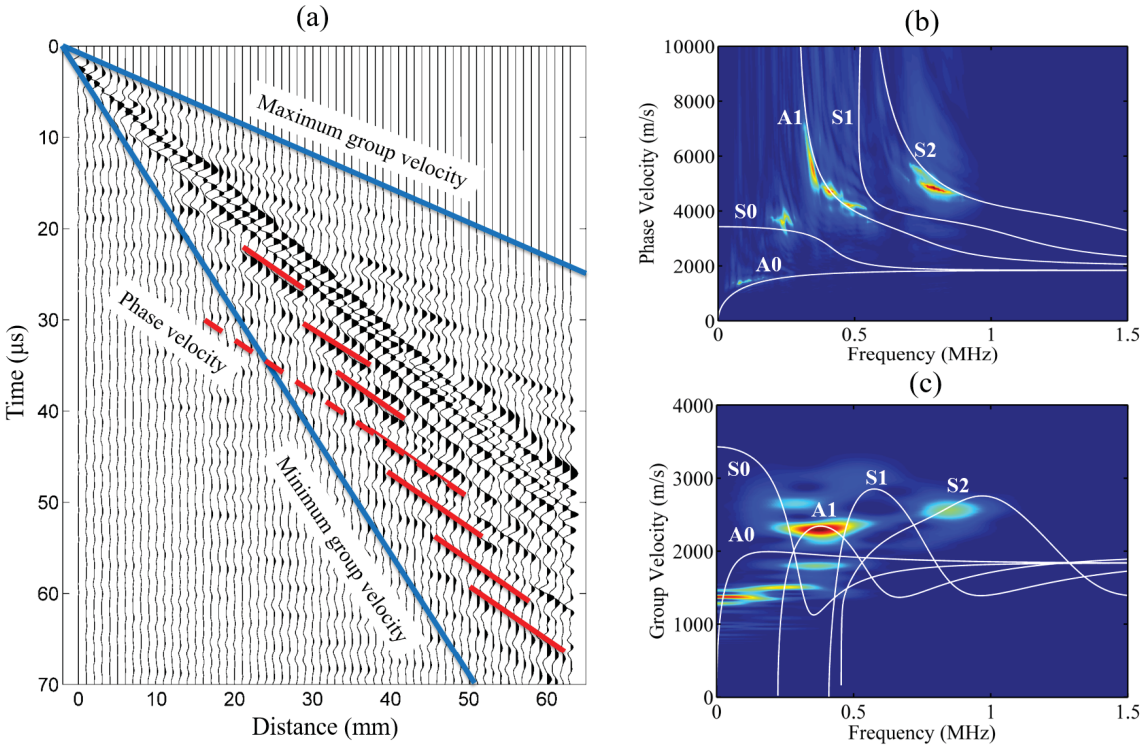

Figure 2.6: (a) Identification of the group and phase velocities on a multichannel time-offset data from a bone plate. (b) Theoretical phase velocity dispersion curves are superimposed on the dispersion energies of a bone-plate data. (c) Theoretical group velocity dispersion curves are superimposed on the dispersion energies of a bone-plate data. Several low-order Lamb modes are labeled.

2.4.1.1 Single-channel Analysis

To image group velocity distribution of UGW energy from long bones, short time Fourier transform (STFT) was introduced back in 2006 to process a single time series (Protopappas *et al.*, 2006). The time-domain signal was Fourier transformed while segmented by a sliding short time Hamming window resulting in a time-frequency (t-f) representation. Xu *et al.* (2010) later applied a STFT-based method called multiridge-based analysis in which a crazy-climber algorithm was used to detect and separate t-f energy ridges from a multi-modal signal. The corresponding waveform representatives of individual guided modes can be reconstructed from the identified t-f ridges. However, on the application end, the drawback of this method was that manual interaction is required for mode identification. Song *et al.* (2011) utilized the joint approximate diagonalization of eigen-matrices algorithm (JADE) to separate the superimposed guided waves in long bones. The group velocities of extracted modes were then computed by the adaptive Gaussian chirplet t-f and difference value methods. Even though JADE has high time-frequency resolution and low computational cost, identifying the guided modes under noisy condition is still a challenging task with this technique and pretreatment filter is prerequisite to denoise the signals. Dispersion compensation technique has been developed to facilitate Lamb mode separation of multi-mode single-channel recording (Xu *et al.*, 2012). The approach, nevertheless, is unable to separate UGW modes traveling at the same speed and requires a great deal of prior knowledge about the UGW data, which is difficult to have access in clinical applications. Its performance was limited to application on the steel-plate experimental signals only. In a research paper by Zhang *et al.*, 2013, joint spectrogram segmentation and ridge-extraction (JSSRE) was used to improve the previous works in guided wave modal filtering. First, the Gabor t-f transform calculated the spectrogram of the multi-modal signals. Then, a multi-class image segmentation algorithm was involved to find the corresponding region of each UGW mode in the spectrogram, including an improved watershed transform and a region growing procedure. Finally, the ridges were extracted and the time-domain signals representing individual modes were reconstructed from their corresponding ridges. Despite only simulation datasets with different SNR were presented in this study, JSSRE showed its efficacy to separate and reconstruct the multi-modal UGW signals and a great potential for bone data evaluation. The most recent work by Xu *et al.*, 2014 employed the wideband dispersion reversal (WDR) to detect single-mode pulses. Compared with the dispersion compensation method presented earlier in Xu *et al.*, 2012, WDR has the advantages of

multi-modal design and selective excitation but it still needs more experimental validation. Same with Song *et al.*, 2011 study, WDR technique makes use of some a priori knowledge of the UGW dispersion characteristics to synthesize the corresponding dispersive reversal excitations, which is its disadvantage. Mode conversion and overlap are tough problems for guided wave analysis. Further research is necessary to evaluate the efficacy and ability in bone UGW data identification and interpretation of the aforementioned proposed approaches especially when dealing with clinical data from human beings.

2.4.1.2 Multi-channel Analysis

Regarding the multi-channel analysis for phase velocity imaging, the set of recorded time-space signals measured on bone specimens can be represented in the frequency-wavenumber (f-k) domain using the traditional two-dimensional spatio-temporal Fourier transform (2D-FFT) (Lefebvre *et al.*, 2002). The number and distribution of inspected space positions, the resolution thus the ability to discriminate two closely spaced guided modes clumping together (Moilanen, 2008) are known limitations of the 2D-FFT. Moilanen *et al.*, 2006 then applied a group velocity filtering (GVF) to improve the 2D-FFT extraction of fundamental flexural guided mode. The GVF technique relies on the use of a Hanning time window to selectively envelope and isolate the late arrival contribution from the recorded signals. The so-called "selective 2D-FFT" approach truly can not increase the 2D-FFT resolution and lacks of the capability to discriminate signals that are overlapping in time domain. The well-known singular value decomposition (SVD) has been adapted to apply *in vitro* on human radius to extract the most energetic late arrival signals (Sasso *et al.*, 2009; Minonzio *et al.*, 2010). The limited ability of SVD-based wave extraction algorithm is that it requires the application of a signal alignment or synchronization procedure, which has been shown to be mainly responsible for the inaccuracy. Motivated by the successful application of the high-resolution Radon transform (HRRT) in exploration and global seismology (Sacchi and Ulrych, 1995), Tran *et al*. applied the technique to image dispersive guide wave energy in long cortical bones (Le *et al.*, 2013; Tran *et al.*, 2014*a*) and to filter and reconstruct the UGW modes (Tran *et al.*, 2014*b*). The linear Radon or time intercept-slowness (τ-p) transform considers the UGW fields as a superposition of plane waves defined by ray parameters or slowness, p, and time intercepts, τ. The transform was computed by summing the data in t-x domain along straight lines with a range of slopes and intercepts and then mapping them onto a τ-p plane. Wavefields traveling with different phase velocities and intercepting the time axis at different zero-offset time intercepts are well separated in the τ-p panel.

The transform algorithm was posed as an inverse problem in the frequency domain with a Cauchy-norm sparseness constraint that serves to enhance the focusing power of the Radon operator. From the f-p Radon solution, the f-c dispersion panel could be obtained by the relationship $p = 1/c$. The publications (Le *et al.*, 2013; Tran *et al.*, 2014*a*; Tran *et al.*, 2014*b*) recommend the adoption of HRRT as a powerful tool to enhance the resolution of phase velocity dispersion curves especially when the data acquisition aperture is limited and uneven station sampling occurs in routine clinical tests. The improvement in Radon resolution rendered more discriminating power to separate UGW modes and provided an opportunity to isolate the wavefields/guided modes more precisely for further analysis. Inspiring by the Canadian group's works on sparsity-constraint Radon transform, Xu *et al.* recently developed sparse-SVD (Xu *et al.*, 2016) and dispersive Radon (Xu *et al.*, 2018) transforms to process ultrasonic wave signals guided by cortical bone. The computational cost of these methods are not low because inversion of large-scale matrices is involved. Okumura *et al.*, 2017 applied adaptive beamforming and estimation of signal parameters via rotational invariance technique (ESPRIT) technique on phase velocity computation for UGW propagating along cortical long bones. Their algorithm also employed eigen-value decomposition to separate the signal of interest from noise. Because the eigen-value decomposition and matrix inversion procedures are computationally expensive, improvement of the algorithmic efficiency would be useful for practical applications. Therefore, in a more recent study (Okumura *et al.*, 2018), the authors proposed rapid high-resolution wavenumber extraction using adaptive array method. The proposed approach was more computationally efficient because it used a diagonal loading technique instead of an iterative process. The frequency-dependent wavenumbers of UGW signals from numerical simulation and bone-mimicking plate experiments were estimated with less than 4% errors. Advancement in multi-channel signal processing has widened the scope of dispersion analysis in quantitative bone ultrasound.

2.4.2 Long Bone Modeling

In order to solve the bone inversion problem, i.e., to extract bone parameters from the acquired ultrasound data, a numerical simulation tool must be developed to predict the dispersion curves given a bone model. Developing accurate forward modeling algorithms plays a keystone to solve the model-based inverse problem to recover bone properties. This is an emerging research direction in the bone ultrasonography community of the current decade. In this section, a review of the state-of-the-art in guided wave propagation analysis in long

bones is presented. Various methods are then discussed with respect to their capability of simulating UGW propagation phenomena and how such simulators have been validated. These numerical approaches can be classified into two families: full waveform simulation and dispersion characteristic calculation.

2.4.2.1 Waveform Simulation

Back in 2002, the modeling of axially-transmitted ultrasonic waves traveling in cortical bone was first introduced by Bossy *et al.*, 2002 using a 2D simulation software called Wave2000 Pro (Cyberlogic Inc., New York, USA). This commercial package computed a numerical solution to the 2D elastic wave propagation based on a finite difference method. The authors focused their interest on the speed of sound (SOS) of the first arriving signal (FAS) and its dependence on the bone plate thickness. The simulational setting was carried out with spherical source and the bone plate immersed in water. Two years later, Bossy *et al.*, 2004 self developed a 3D finite-difference code to investigate the ultrasonic axial transmission velocity measurement on cortical bone cylinders. In this study, their focus was on the effects of 3D bone geometry such as curvature and cortical thickness, anisotropy, and microporosity on SOS measurements. The results showed that SOSs measured on tubular cortical shells were identical to the values measured on cortical plates of equal thickness and anisotropy had major influence on SOS measures as a function of bone thickness. Protopappas *et al.* (Protopappas *et al.*, 2006; Protopappas *et al.*, 2007) applied a 3D finite-element computational approach (ABAQUS/Explicit version 6.4) to model UGW propagation in intact and healing long bones. The bone structures were modeled as uniform hollow circular cylinders with their cross sections being determined by CT transverse scans. This work presented the significant impact of bone irregularity and anisotropy to UGW dispersion. UGW were shown to be sensitive to material and geometrical changes during fracture healing process. To conclude, in the early days of bone quantitative ultrasound, the research heavily relied on commercial softwares that were not idealized to solve wave propagation problems in long cortical bones.

In 2010, Le *et al.* used seismological principles and geophysical techniques including reflectivity-method waveform modeling and travel time calculation to study the ultrasonic wave propagation in long bones at small source-receiver offsets. Their numerical and experimental tests demonstrated that the bone ultrasound response could be reasonably simulated and interpreted by a horizontally layered model. The layers were homogeneous and isotropic. This was the first attempt to employ a multi-layer with cortical plate coupled

with fluids to explain the *ex-vivo* axial-transmission echogram of a bovine tibia.

The complexity of multi-layer bone models was then upgraded with the anisotropy and viscosity effects taken into account by Nguyen and Naili, 2011. This work dealt with a 2D functionally-graded anisotropic solid material coupled with semi-infinite fluid media. The numerical solution to this model was described by Cartesian coordinates using spectral finite element method (SFEM). The problem was formulated in the frequency-wavenumber domain by applying a combined Laplace-Fourier transform. The inverse Laplace transform technique reversed the solution back into time-space domain. The approach was validated against the conventional FEM and dynamic finite element analysis performed by COMSOL Multiphysics (COMSOL Inc., Stockholm, Sweden). The proposed SFEM was significantly efficient due to the dimensional reduction. The same group of authors later added poroelasticity into the materials by using Biot's theory (Nguyen and Naili, 2012). A hybrid spectral/finite element method (S/FEM) formulation was developed to find the time-domain solution of UGW existing in a poroelastic plate immersed in two fluid halfspaces. Similar to the previous work (Nguyen and Naili, 2011), the numerical tests showed perfect match between the S/FEM technique and the conventional FEM and COMSOL software.

The 3D cylindrical velocity model, which was constructed by bilinear interpolation and the piecewise cubic Hermite interpolating polynomial method, was investigated by Hata *et al.*, 2016 and Takano *et al.*, 2017. The elastic finite-difference time-domain (FDTD) technique was used to simulate the axial ultrasonic waves traveling in these heterogeneous models. The effect of cortical heterogeneity was found in the simulation results to be significant for the wave propagation and FAS velocity. The human bone heterogeneity and anisotropy were emphasized to be important factors in long bone computational modeling. These numerical studies did not consider wave attenuation in the simulated materials. Osteoporotic bones are often porotic therefore the attenuation influence will be worth analyzed in the future. Potsika *et al.*, 2017 presented the finite difference, finite element, and boundary element methods to interpret the ultrasonic signals acquired at different stages of osteoporosis and fracture healing process. Ultrasonic velocity was found to be a potential indicator for osteoporosis diagnosis at an early stage. The wave speed was theoretically observed to decrease during the first healing stages and gradually to increase in later stages approximating the values of intact bones. Potsika *et al.*, 2017 also mentioned that the dispersion of guided waves provided supplementary qualitative information for ultrasonic evaluation of bones.

2.4.2.2 Dispersion Curve Simulation

Chen *et al.*, 2012 used an fluid-solid bilayered model to explain the dispersion mechanism of ultrasound waves guided by soft tissues-cortex phantoms. The plate model served as a good approximation of the bone waveguide to theoretically compute the wavenumber dispersion curves of bilayer guided modes. For simplicity, the two layers of the model were considered as two decoupled waveguides. The dispersion equation was solved analytically. By means of this analytical tool, the coupling effect of the overlying soft tissue layer to UGW propagation characteristic was researched. In a study to also inspect the influence of soft tissues to the dispersive UGW traveling in the cortex, Tran *et al.*, 2013 utilized the DISPERSE software (version 2.0.16i, Imperial College London, London, UK) to simulate phase-velocity dispersion curves. Different from Chen *et al.*, 2012, the soft tissue-cortical bone structure in this work was treated as a single waveguide. DISPERSE is a commercial package widely used in ultrasonic nondestructive testing. However, it has challenges when dealing with bone models that involve fluids and complex boundary conditions. More recently, Nguyen *et al.*, 2017 implemented the semi-analytical finite element (SAFE) method to compute the velocity dispersion and attenuation in a tri-layered system consisting of a transversely-isotropic cortical bone plate sandwiched between the soft tissues and bone marrow layers. The computational accuracy of the proposed SAFE technique was validated against the DISPERSE software and published literature. The algorithm was also applied to interpret of an *ex-vivo* experimental dataset from a bone phantom.

The cylindrical model of guided waves propagation in long bones was first investigated by Ta *et al.*, 2006*a*. In the analytical model, the dispersion curves were derived by Bessel function. What made this study distinct from the previous works was the geometry they applied in this work: hollow cylindrical model and cylinder immersed in water. The validity of this simulation was verified by *in-vivo* experiment carried out in cylinder immersed in water. These model were used to simulate bone and bone covered with marrow. The results revealed a significant match between analytical solution and experimental data. In a following study by this group (Ta *et al.*, 2009), attenuation was considered and was simulated using a hollow cylinder model filled with a viscous liquid. The numerical model was executed in DISPERSE. As a comparison to numerical solution, the experiment setting was also supplemented with attenuation. The results also showed good agreement between simulation and experiment. As for cylindrical model with multilayers considering coupling effect, SAFE method has been found to be excellent tool in modeling bones. In a study

published in 2017, Thakare *et al*. applied the SAFE numerical approach to simulate wave propagation in bones and to predict the dispersive curves. Healthy bone and bone with osteoporosis was studied. What should be mentioned here is that their simulational framework allows the assessment of anisotropy, porosity and some other effects on the cortical media. The comparison of experimental data and numerical simulation results revealed a strong correlation. Based on the Thakare *et al.*, 2017 study, this group improved their SAFE modeling for cylindrical, irregular, multi-layer, and heterogeneous bone cross-section with anisotropic and viscoelastic material properties (Pereira *et al.*, 2017). The SAFE method was compared with 3D finite difference method and showed good matching.

2.4.3 Bone Imaging and Inversion

The ultimate goal of quantitative ultrasonography is to extract the bone parameters such as cortical thickness and elastic constants from UGW signals. This review section covers advances in the inverse problem for long bone characterization, i.e. the current numerical techniques to find approximate solutions of cortex imaging and their performance results.

2.4.3.1 Cortical Bone Imaging

Zheng *et al*., 2015 applied the wave scattering theory to image the internal geometry of long bones from axial zero-offset reflection data. The wavefield imaging method was implemented based on the Born inversion technique and the conjugate gradient iterative algorithm. The *in-vitro* cortex interfaces along the axial direction were fairly accurate imaged. Later, Tasinkevych *et al.*, 2016 estimated the cortical bone thickness and acoustic wave velocity using a multivariable optimization approach by fitting the temporal spectrum of the simulated reflected wave to the spectrum of the experimentally-measured reflected wave. They developed an echo-simulation model of soft tissue-cortical bone-cancellous bone. The least square cost function was minimized by simulated annealing algorithm. The proposed method was tested with a custom designed bone mimicking phantom and a calf femur. The relative errors of thickness and velocity assessment were 0.4%-10.8% and 3.1%-4.5% respectively for different samples. Bernard *et al.*, 2017 performed a full-waveform inversion of two-dimensional ultrasonic computed tomography data for long bone cross-sectional imaging using a quasi-Newton technique called the limited-memory Broyden-Fletcher-Goldfarb-Shanno (L-BFGS) method. The technique was benchmarked with synthetic datasets of increasing complexity, with or without noise, including a tibia-fibula bone pair model. However no real experimental data has been involved yet. Recently, Renaud *et al.*, 2018 were able to reconstruct

the transverse and sagittal (longitudinal) ultrasound images of the tibial and radial top cortical shell using ray-tracing technique and delay-and-sum algorithm. Their work considers wave refraction and anisotropy in cortex thus allowing the measurements of the cortical ultrasonic wave-speed and anisotropy. It's the first *in-vivo* approach that provides the direct estimates of the magnitude and type of the elastic anisotropy of cortical bone. The estimated ultrasonic biomarkers agreed with the values measured with high-resolution peripheral X-ray computed tomography. Their study demonstrated the *in-vivo* feasibility of accurate ultrasonic imaging of the cortex. However, in order to reconstruct the complete bone cross-section image, there are still several outstanding physics-involved issues such as ultrasonic attenuation and multiple reflections that need to be addressed.

2.4.3.2 Inversion of Ultrasonic Guided Waves

For the dispersion-based inversion of axially-transmitted ultrasonic records that is the focus of this thesis, there are only a few studies published in the last four years. A paper by Foiret *et al.*, 2014 was the first work on the estimation of several cortical bone properties from UGW measurements in bone-mimicking phantoms and human radius bone samples. The report was a good attempt to apply the Matlab built-in gradient method to recover bone thickness and elastic characteristics with a few percent error. Two years later, they extended the study to *in-vivo* data measurements from the forearm of 14 healthy subjects (Vallet *et al.*, 2016). An exhaustive search in the frequency-wavenumber model space with very narrow range of cortical thickness from 0.5 mm to 4 mm was presented. The cortical thickness estimates were validated by comparison with the site-matched values derived from high-resolution peripheral quantitative computer tomography (HR-pQCT). A significant correlation has been found between the inverted and reference values ($r^2 = 0.7$, $p < 0.05$, RMSE = 0.21 mm). The same group of authors later proposed a genetic algorithm and the application of the genetic algorithm-based inversion on *in-vivo* datasets (Bochud *et al.*, 2016; Bochud *et al.*, 2017). In the aforementioned works, the inversion procedure was formulated in frequency-wavenumber (f-k) domain and transversely-isotopic (TI) free plate model was employed to fit the experimental dispersion curves. Their approaches still have limitations such as inaccuracy in the estimation parameters due to relatively high number of unknowns and lack of soft-tissue-layer consideration in the simulating model. The modeling of UGW propagation in the multilayered waveguide such as cortex coupled with soft tissues has been a long-standing problem for quantitative guided wave ultrasonography (QGWU). Tran *et al.* (Tran *et al.*, 2018*b*; Tran *et al.*, 2018*c*; Tran *et al.*, 2019 submitted) have recently

developed a nonlinear grid-search optimization method applied in bone inversion. Their semi-analytical finite-element (SAFE) model considers a soft tissue-cortex bilayer. The dispersion-curve inversion has been solved in the multi-modal frequency-phase velocity (f-c_p) domain. The technique exhaustively examines a large databank of possible solutions and pick the optimal one which minimizes the misfit function. The method is feasible for the small scale inverse problem, i.e. small number of unknown parameters to reconstruct, and the parameters lie within specific ranges of values like the bone data examples. The method's performance has been verified using numerically simulated and bone phantom datasets with acceptable accuracy.

Chapter 3

Signal Processing

3.1 Introduction

As multi-channel ultrasonic axial-transmission data are multi-modal by nature, wave field filtering becomes important because the analysis is usually limited to a few lower-order modes and requires their extraction. Multi-channel analysis of dispersive ultrasonic energy also requires a reliable mapping of the data from the time-distance (t-x) domain to the frequency-wavenumber (f-k) or frequency-phase velocity (f-c) domain. The mapping is usually performed by the classical two-dimensional Fourier transform with a subsequent substitution and interpolation via $c = 2\pi f/k$. The extracted dispersion trajectories of the guided modes lack the resolution in the transformed plane to discriminate wave modes. The resolving power associated with the Fourier transform is closely linked to the aperture of the recorded data. Motivated by the successful applications of the Radon transform (RT) in geophysics and exploration and global seismology, in this Chapter 3, a high-resolution linear Radon transform is implemented to provide sufficient wave field separation capability and imaging resolution to analyze multi-modal UGW signals for bone tissue characterization.

Section 3.2 provides the methodology of linear Radon or τ-p transform. The method considers guided wave fields as superpositions of plane waves defined by ray parameters or slowness (p) and time intercepts (τ) and stacks the amplitudes along linear trajectories. The transform is computed by summing the data in t-x domain along straight lines with a range of slopes and intercepts, mapping t-x data to a τ-p or Radon panel. Wave fields traveling with different phase velocities and intercepting the time axis at different zero-offset time intercepts are well separated in the τ-p panel. The transform algorithm is posed as an inverse problem in the frequency domain, which allows the implementation of regularization strategy to enhance the focusing power. A Cauchy-norm sparseness constraint serves to enhance the focusing power of the Radon operator. Sparsity-promoting Radon transform

is a powerful tool to enhance the resolution of dispersion curves especially when the data acquisition aperture is limited and uneven station sampling occurs in routine clinical tests. The improvement in Radon resolution will render more discriminating power to separate UGW modes and provide an opportunity to isolate the wave fields/guided modes more precisely for further analysis.

In Section 3.3, an application of the Radon transform to enhance signal-to-noise ratio and separate wave fields in ultrasonic records is presented. The method was verified using simulated data and applied to an uneven-spatially-sampled bovine-bone-plate data set. The results demonstrate the Radon panels show isolated amplitude clusters and the Cauchy-norm constraint provides a more focused Radon image than the damped least-squares regularization. Wave field separation can be achieved by selectively windowing the τ-p signals and inverse transformation, which is illustrated by the successful extraction of the $A0$ mode in bone plate. In addition, the method effectively attenuates noise, enhances the coherency of the guided wave modes, and reconstructs the missing records. The proposed transform presents a powerful signal-enhancement tool to process guided waves for further analysis and inversion.

Section 3.4 discusses the application of the linear Radon transform to image the dispersive energies of the recorded ultrasound wave fields. Three solutions of Radon transform: adjoint (ART), damped least-squares (LSRT), and high-resolution (HRRT) are described and their robustness are compared using simulated and cervine bone data. The Radon solution also depends on the data aperture but not as severely as the Fourier transform. With Radon transform, the resolution of the dispersion panel could be improved up to around 300% over the Fourier transform. Among the Radon solutions, the HRRT delineated the guided wave energy with much better imaging resolution (at least 110%) than the other two forms. The Radon operator can also accommodate unevenly spaced records. The results suggest that the high-resolution Radon transform is a valuable imaging tool to extract dispersive guided wave energies under limited aperture.

3.2 Linear Radon or $\tau - \mathrm{p}$ Transform

Consider a series of ultrasonic time signals $d(t, x_n)$ at different offsets x_0, x_1, ..., x_{N-1} where t denotes time and the x-coordinates are not necessarily evenly sampled. The discrete Radon or τ-p transform is defined by the summation along a line $t = \tau + p_k x$ with ray parameter

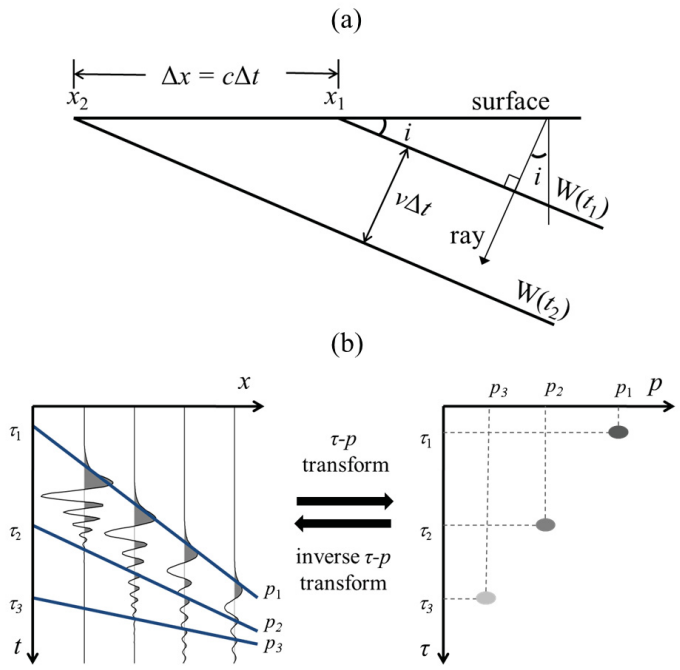

Figure 3.1: Illustration of horizontal phase velocity and the τ-p transform. (a) A plane wavefront W propagates obliquely into the material at an angle i with the horizontal surface. The ray, which is normal to the plane wavefront, travels at the same incident angle i with the normal to the surface. When the wavefront travels $v\Delta t$ into the material where v is the material velocity, the point of intersection, x_1 where the wavefront meets the surface, travels to x_2 through a distance $c\Delta t$ where c is the (horizontal) phase velocity. By trigonometry, $p = 1/c = \Delta t/\Delta x = \sin i/v$. (b) The schematic diagram for forward and inverse linear τ-p transform. The records are summed along straight lines with different slopes p and time intercepts τ. Stacking along p_1 goes through strong peaks of the records and thus yields a strong amplitude focus in the τ-p panel (dark gray ellipse) while stacking along p_2 encounters amplitudes of opposite polarities and thus leads to less Radon energy. Stacking along p_3 leads to trivial Radon energy due to very small amplitudes of the signals (modified from Gu and Sacchi, 2009).

p_k and time intercept τ

$$\tilde{m}(\tau, p_k) = \sum_{n=0}^{N-1} d(t = \tau + p_k x_n, x_n), \quad k = 0, ..., K-1 \tag{3.1}$$

where $\tilde{m}(\tau, p_k)$ is a Radon or τ-p series obtained via the so called adjoint operator (Sacchi and Ulrych, 1995). The adjoint is also called the conjugate transpose operator. The ray parameter p, which is related to the material velocity and incident angle via Snell's law (Figure 3.1a), are sampled at p_0, p_1, ..., p_{K-1}, and the intercept τ is the arrival time at zero-offset. Equation 3.1 defines a low-resolution mapping of a linear arrival to a point in the Radon panel (Figure 3.1b) (Sacchi and Ulrych, 1995).

In order to enhance the resolution of modes in the τ-p domain and to have a viable technique for signal reconstruction, the estimation of the Radon coefficients is posed as an inverse problem. Thus the data in the time-offset space is represented via a synthesis of Radon coefficients $m(\tau, p)$

$$d(t, x_n) = \sum_{k=0}^{K-1} m(\tau = t - p_k x_n, p_k), \quad n = 0, ..., N-1. \tag{3.2}$$

Notice that because the Radon transform is not an orthonormal operator, $\tilde{m}(\tau, p)$ is not equal to $m(\tau, p)$. In other words, Equation 3.1 (the adjoint operator) and Equation 3.2 (the forward modeling operator) are not the inverse of each other. Notice also that once $m(\tau, p)$ is estimated, it can be used to reconstruct the signal $d(t, x)$ using a subset of ray parameters p. In other words, one can implement filtering techniques to retain desired modes of propagation and use them to reconstruct the data represented by those modes. The task of inverting Equation 3.1 is simplified in the frequency domain. Taking the temporal Fourier transform of Equation 3.2 yields

$$D(f, x_n) = \sum_{k=0}^{K-1} M(f, p_k) e^{-i2\pi f p_k x_n} \tag{3.3}$$

where the time-delay property of Fourier transform has been used. Writing the latter in matrix notation and omitting f in the arguments, Equation 3.3 becomes

$$\mathbf{D} = \mathbf{L}\mathbf{M} \tag{3.4}$$

where the Radon operator $\mathbf{L}$ is

$$\mathbf{L} = \begin{bmatrix} e^{-i\omega p_0 x_0} & \dots & e^{-i\omega p_{K-1} x_0} \\ \vdots & \ddots & \vdots \\ e^{-i\omega p_0 x_{N-1}} & \dots & e^{-i\omega p_{K-1} x_{N-1}} \end{bmatrix} \tag{3.5}$$

with $\omega = 2\pi f$.

A least-squares (LS) solution to Equation 3.4 can be obtained by minimizing the following cost function,

$$J = \|\mathbf{L}\mathbf{M} - \mathbf{D}\|^2 + \mu R(\mathbf{M}). \tag{3.6}$$

with respect to the model $\mathbf{M}$ (Sacchi, 1997; Moldoveanu-Constantinescu, 2006). The first term on the right denotes the data misfit, which quantifies the error between the reconstructed and original data and thus measures how well the Radon operator predicts the data; the second term is known as the regularization term $R(\mathbf{M})$ which is included to guarantee the uniqueness and stability of the solution (Tikhonov and Goncharsky, 1987). The

regularization parameter μ controls the degree of fitting the predicted observations to the actual data. For example, if μ is small, emphasis is to seek a solution to minimize the prediction error and the data is accurately reproduced including noise. However if μ is large, the Radon energy will be focused but the data is under-fitted or poorly reconstructed.

Different regularization functions $R(\mathbf{M})$ have been proposed to estimate the Radon coefficients $M(f,p)$. For instance, one can select the quadratic norm or l_2 norm i.e., $\|\mathbf{M}\|^2$. In this case the Radon solution is known as the damped least-squares (DLS) solution (Menke, 2012)

$$\mathbf{M} = (\mathbf{L}^H\mathbf{L} + \mu\mathbf{I})^{-1}\mathbf{L}^H\mathbf{D} \tag{3.7}$$

where $\mathbf{L}^H$ is the adjoint of the Radon operator $\mathbf{L}$ and $\mathbf{I}$ is the identity matrix. This solution is not able to focus adequately the modes in the Radon panel and leads to τ-p signals with significant amplitude smearing (Sacchi and Ulrych, 1995; Trad *et al.*, 2002). This problem is alleviated by using a regularization term that enforces sparsity in the τ-p panel. This is possible by adopting a non-quadratic regularization strategy based on a Cauchy criterion. The Cauchy norm is considered a suitable regularization term to obtain sparse τ-p solutions and enhance their resolution of Radon panels (Sacchi and Ulrych, 1995; Moldoveanu-Constantinescu, 2006). $R(\mathbf{M})$ is taken to be the Cauchy criterion used to regularize the solution, i.e.,

$$R(\mathbf{M}) = \sum_{k=0}^{K-1} ln(1 + M_k^2/\sigma^2) \tag{3.8}$$

where σ^2 is the scale factor of the Cauchy distribution. By minimizing the cost function (6) with respect to the model $\mathbf{M}$, the Radon solution is given by

$$\mathbf{M} = (\mathbf{L}^H\mathbf{L} + \mu\mathbf{Q}(\mathbf{M}))^{-1}\mathbf{L}^H\mathbf{D} \tag{3.9}$$

where $\mathbf{Q}(\mathbf{M})$ is a diagonal weighting matrix with elements given by

$$Q_{kk} = \frac{1}{(1 + M_k^2/\sigma^2)}. \tag{3.10}$$

Equation 3.9 provides a high-resolution Radon solution and is a non-linear system of equations, which can be solved by the following iteratively re-weighted least-squares (IRLS) scheme for each frequency (Sacchi and Ulrych, 1995; Sacchi, 1997).

1) Select the hyper-parameters μ and σ. σ is fixed at 0.8 and examine the fit of the predicted data to the original data to select μ.

2) Start with the DLS solution as an initial solution, i.e.,

$$\mathbf{M}_0 = (\mathbf{L}^H\mathbf{L} + \mu\mathbf{I})^{-1}\mathbf{L}^H\mathbf{D}.$$

3) Compute the initial weighting matrix

$$Q_{0,kk} = \frac{1}{(1 + M_{0,k}^2/\sigma^2)}.$$

4) The initial weighting matrix $\mathbf{Q}_0$ is now used to calculate a new solution

$$\mathbf{M}_1 = (\mathbf{L}^H\mathbf{L} + \mu\mathbf{Q}_0)^{-1}\mathbf{L}^H\mathbf{D}.$$

5) The weighting matrix $\mathbf{Q}_1$ is computed using the solution $\mathbf{M}_1$. A new solution $\mathbf{M}_2$ is then estimated by $\mathbf{Q}_1$.

6) After z iterations, the solution and the cost function are, respectively, given by

$$\mathbf{M}_z = (\mathbf{L}^H\mathbf{L} + \mu\mathbf{Q}_{z-1})^{-1}\mathbf{L}^H\mathbf{D}$$

and

$$J_z = \|\mathbf{L}\mathbf{M}_z - \mathbf{D}\|^2 + \mu R(\mathbf{M}_z).$$

7) The procedure is terminated when the tolerance is met:

$$\frac{|J_z - J_{z-1}|}{(|J_z| + |J_{z-1}|)/2} < \text{tolerance}$$

or the number of iteration is reached.

8) Compute the data misfit. Re-select a new trade-off parameter, μ if the result is not satisfactory.

Appendix A summarizes the IRLS method and an implementation of the HRRT algorithm.

Once $\mathbf{M}$ is determined for all frequencies, inverse Fourier transform is performed to map $\mathbf{M}$ back to time domain $\mathbf{m}$, creating a τ-p Radon panel. Equation 3.9 and 3.4 can be considered as the Radon and inverse Radon transforms in the frequency domain. A brief schematic algorithm is summarized in Figure 3.2. The iterative algorithm is used to estimate the Radon solutions (panels) presented later in this chapter. In the τ-p domain, windowing can be used to extract wave fields of desired slownesses while muting the others. It should be noted that the dispersion (f-c) curves can be extracted by mapping the f-p to f-c panels via $c = 1/p$ and preferably, linear interpolation. As shown in Figure 3.2, the filtered t-x signals are reconstructed by performing the operations in reverse order: Fourier-transform the Radon panel to the f-p panel, map the f-p panel to the f-x panel via Equation 3.4 using the Radon operator $\mathbf{L}$, and inverse Fourier-transform the f-x panel to the t-x domain.

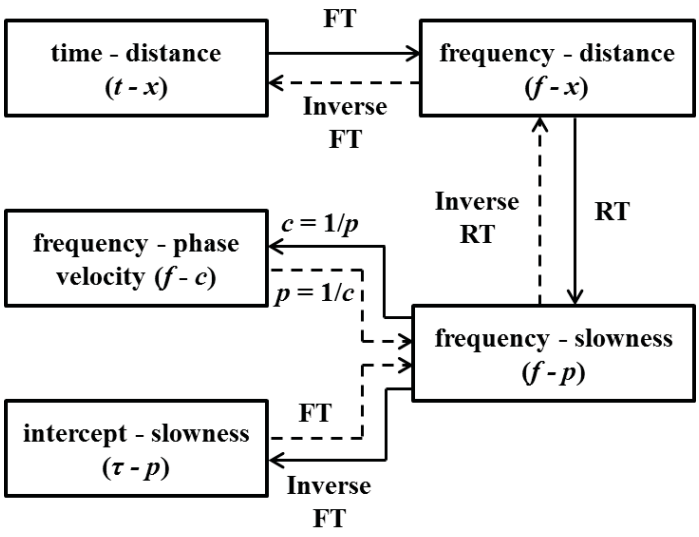

Figure 3.2: A flowchart of the τ-p method. FT denotes Fourier transform. The Radon transform (RT) and its inverse are given by Equations 3.9 and 3.4 respectively. Once the f-p panel is obtained, either the τ-p (Radon) panel or the f-c panel can be computed. The former is obtained by inverse FT transform while the latter by replacing slowness by the inverse of phase velocity $1/c$.

3.3 Wavefield Separation

3.3.1 Introduction

Ultrasonic guided wave technologies are powerful nondestructive testing techniques to characterize near-surface materials and evaluate integrity of materials or structures such as plates, cylinders, and pipes (Rose, 2002). UGW testing has been successfully used in a wide range of industrial applications such as structural health monitoring and material characterization. These applications are, for example, damage assessment of layered composites (Kim *et al.*, 2007), identification of rail defects (Lee *et al.*, 2009; Coccia *et al.*, 2011), characterization of Zircaloy tubes (Yeh and Yang, 2011), and highly absorptive materials such as bitumen (Simonetti and Cawley, 2003), and detection of ice on aircraft wing (Gao and Rose, 2009). Guided waves have also received considerable attention in geotechnical and seismological studies. The GW techniques have been used to monitor the stability of grouted rock bolt (Zou and Cui, 2011), image the subsurface permittivity structure using ground penetrating radar (GPR) guided waves (Decker and Haney, 2010), and visualize fault zone structure (Korneev *et al.*, 2003). In recent years, GW application has been used to study long bones (Ta *et al.*, 2006*a*) and monitor bone fractures (Protopappas *et al.*, 2006).

Ultrasonic Lamb waves are elastic waves propagating in a plate and require boundaries

for their existence (Rose, 1999). The boundaries of the structure act as waveguide to retain the energy, thus keeping the GW energy from spreading out. Therefore, guided waves can travel over considerable distances and interact with a larger portion of the structure. The GW modes travel with different velocities, which vary with frequency. The dispersive properties, which are characteristic for each mode, are described by the dispersion curves. The dispersion curves are not only dependent on the material properties but also the thickness of the structure under investigation.

Guided waves are often studied using multi-channel recordings. One of the most common acquisition arrangements is to have the transmitter and receiver arrays located on the same side of the testing structure. The source and receivers are ultrasonic transducers. Usually the transmitter is stationary with many receivers laid out collinearly at multiple locations on both sides or one side of the transmitter. This is equivalent to the split-spread or end-on spread shooting profile in seismic reflection prospecting (Telford *et al.*, 1990). In bone study, the arrangement is also known as the axial transmission configuration (Le *et al.*, 2010). The data are usually acquired at a uniform spatial spacing interval with limited aperture. The acquisition can be done using a single receiver measured at multiple locations (Le *et al.*, 2010) or a transducer array (Bossy *et al.*, 2004; Nguyen *et al.*, 2013). The regular spatial sampling is usually required for the subsequent Fourier analysis of the dispersive characteristics of the signals. The recorded signals form a time-offset matrix of signal amplitudes where offset is the source-receiver distance. The data, which records the motion of the structure underlying the receivers subject to the source excitation, exhibits time history of many wave types or modes propagating at various phase velocities. These modes have their own propagation characteristics, governed by the elastic and geometrical properties of the structure. Some modes, especially the lower-order and fundamental modes, are more important than the others in an application and require to be separated from others to enhance their presence and signal-to-noise ratios for more accurate analysis and inversion. However, the amplitudes of the wave modes in the time record overlap, making their separation and identification a difficult and challenging task.

There are several multi-channel approaches to separate wave modes. The most common method is the phase velocity or f-k filtering (Kanasewich, 1981). The t-x records are mapped to the frequency-wavenumber f-k domain by means of the two-dimensional Fourier transform where k is the wavenumber in the direction of guided wave propagation (Alleyne and Cawley, 1991). The multi-mode wave fields propagating with different wave speeds become more visible and separated in the transformed f-k plot, reveal their presence as

strong coherent energy clusters, and the phase velocity, c, of the mode can be determined via $2\pi f/k$. The reject-pass bands, which show as fan windows, are designed to isolate the desired events or modes while muting the rest of the f-k spectrum. The spectrum after windowing is transformed back to t-x domain via inverse Fourier transform. Michaels *et al.*, 2011 applied the technique to remove incident wave and separate lower-order guided waves to enhance damage visualization. However, Fourier-based transform techniques usually have poor performance when the recording aperture is limited (Ta *et al.*, 2006*a*; Ta *et al.*, 2006*b*). In addition, wave modes that have spectral overlap are difficult to separate. Moilanen *et al.*, 2006 applied a group velocity filtering (GVF) to extract the fundamental flexural guided mode propagating in long cortical bones. The GVF method relies on a Hanning time window to selectively isolate the late wave arrivals from the recorded signals. The approach truly lacks the capability to discriminate signals overlapped in the time domain.

Another method is to decompose the t-x data matrix into eigen-images via the SVD (Freire and Ulrych, 1988). This approach has similarities to the principal component analysis and the Karhunen-Loéve transform (Andrews and Patterson, 1976; Jones and Levy, 1987). The SVD presents the data matrix as a sum of weighted eigen-images where the coefficients or weights are the singular values of the data matrix. The magnitude of a singular value dictates the proportional contribution of the corresponding eigen-image to the data reconstruction. When the neighboring time series have some degree of linear dependence or correlation, the data can be reconstructed using the first few largest singular values (or eigen-images). In practice, the desired signals are first aligned by time-shifting to enhance the coherency. The time-shifted matrix is SVD-processed and filtered by choosing a proper subset of the singular values. The selected eigen-images are used to reconstruct the filtered time-shifted data. The time shift is then reversed to yield the filtered data matrix. Freire and Ulrych used SVD to separate upgoing and downgoing waves in vertical seismic profiling (Freire and Ulrych, 1988). The SVD technique was also applied to extract low-frequency ultrasonic wave fields in cortical bone characterization (Sasso *et al.*, 2009). A drawback of this method is that it requires pre-processing step such as wave alignment, which makes the algorithm more complex. Arrivals of interest usually come with a range of phase velocities and it is uncertain how misalignment affects the accuracy of wave field extraction.

Rather than decomposing the ultrasound data into harmonic components or eigen-images, RT studies the plane wave composition of the signals in the plane of zero-offset time intercept τ and ray parameter p (Chapman, 1978; Phinney and Chowdhury, 1981).

The ray parameter is also known as the apparent slowness or horizontal slowness, which is the reciprocal of the horizontal phase velocity c (Figure 3.1a). Here, for simplicity of illustration, a Cartesian coordinate system with vertical and horizontal axes is used. The method considers the ultrasound records as a superposition of various locally linear events. The transform sums all the time records that fall along a line $t = px + \tau$ with slope p and intercept τ, and maps the sum to a point in the τ-p or Radon panel (Figure 3.1b), thus allowing wave field separation and identification. In seismic processing, the method is also known as the τ-p transform or the slant stack (Tatham, 1984). The intensity of the point depends upon the coherency of the linear event and hence, the sum. Wave fields can be separated by their phase velocities and time intercepts. A τ-p window can be used to reject the events outside the window. Late arrivals with the same phase velocities, such as multiples, can be discriminated by the larger time intercepts. The τ-p transform has been used to interpolate missing data and suppress noise for teleseismic data (Wilson and Guitton, 2007), reject events of unwanted strikes and enhance linear events in magnetic data (Pawlowski, 1997), separate seismic wave fields (Greenhalgh *et al.*, 1990), and suppress multiples in seismic data (Foster and Mosher, 1992). Rouze *et al.*, 2010 applied RT to measure shear wave speeds of elastic phantoms and *in-vivo* human livers.

While the RT is widely used in seismology and geophysics to process seismological and geophysical data, its application in ultrasonics is still uncommon. Motivated by the successful experience of the method in processing seismic wave fields, the RT is now applied to separate and enhance guided wave fields. An outline of the RT theory has already been presented in the previous Section 3.2. In this section, the proposed τ-p algorithm's performance is validated using the simulated set of waveforms and will then be applied to separate slowly- and fast-traveling simulated wave fields in a Plexiglass plate and extract low-order guided modes propagating in a bone plate.

3.3.2 Method Validation using Numerical Simulation of Linear Events

In order to test the accuracy of wave field separation, two linear events were simulated (Figure 3.3a). The events traveled a distance of 100 mm at 5 μs/mm (Event 1) and 2 μs/mm (Event 2) respectively. Their arrival times were calculated by $t = px + \tau$ where τ denotes their respective delay times. The time intercepts for the two events were 100 μs and 200 μs. Their arrivals were indicated by two spikes of unit amplitude on the time axis. The time series were then convolved with a source wavelet. The wavelet could be, for example, a Berlage wavelet (Le, 1998) but a Ricker wavelet was chosen (Ricker, 1953) with center

frequency of 20 kHz and unit amplitude. Fifty one records of 700 μs long were generated with 2 mm spacing interval and 2 μs time interval. The simulated signals were bandpassed with a high-cut at 40 kHz.

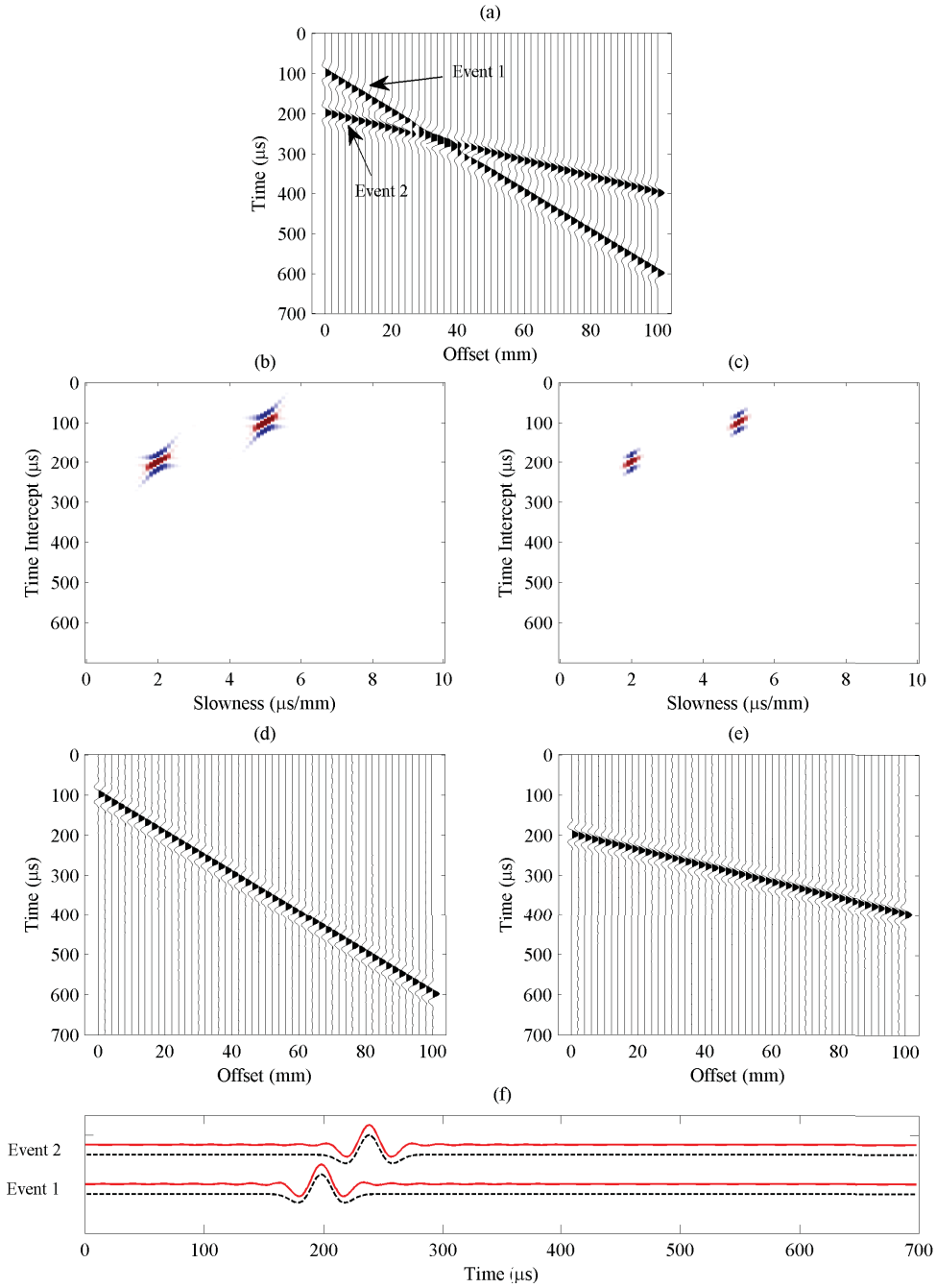

Figure 3.3: Wave field separation of the simulated waveforms. (a) The simulated t-x data shows two linear events traveling at 5 μs/mm (Event 1) and 2 μs/mm (Event 2). (b) The DLS τ-p panel. (c) The HR τ-p panel. (d) The separated Event 1. (e) The separated Event 2. (f) Comparison between the simulated (dashed) and reconstructed signals (solid) at 30 mm offset.

The simulated waveforms with two linear events is shown in Figure 3.3a. The events propagate at 5 μs/mm and 2 μs/mm representing slow- and fast-traveling waves respectively. The events cross, interfere, and result in complex wave fields around 30 mm and 300 μs. The corresponding DLS and HR Radon panels (Figures 3.3b and 3.3c) show two strong amplitude clusters around 5 μs/mm$-$100 μs (Event 1) and 2 μs/mm$-$200 μs (Event 2). The panels have a 0.1 μs/mm resolution. The clusters are much better localized in the HR τ-p panel (Figure 3.3c) than the LS counterpart (Figure 3.3b). The DLS strategy smears the energy along the p-direction by at least 200% relative to the Cauchy constraint. The Cauchy regularization offers better p-filtering or p-windowing because the imaged Radon energy is tightly confined. Therefore, the HR regularization is adopted as the preferred strategy over the DLS in this study. To separate the two events, two mono-p windows: 70 - 130 μs at 5 μs/mm and 170 - 230 μs at 2 μs/mm were chosen to reconstruct Event 1 and Event 2 respectively. All Radon signals outside these ranges were muted. The time windows correspond to the positions and lengths of the wavelets at zero-offset. The two events are well separated as shown in Figures 3.3d and 3.3e. The reconstructed wavelets at 30 mm offset, for example, compare well with the simulated wavelets (Figure 3.3f). The mean-square-errors (MSE) of reconstruction with respect to the signal power are small, 8% for Event 1 and 6% for Event 2, validating the accuracy of the wave field separation.

3.3.3 Application to Simulated Waveforms in a Plexiglass Plate

A Lamb problem with a plate in vacuum was considered. The plate was modeled as a two-dimensional isotropic elastic medium. The dynamic equilibrium equation is

$$\rho \ddot{u}_i - \sigma_{ij,j} = 0 \tag{3.11}$$

where ρ is the mass density; u_i and σ_{ij} are components of the displacement vector and the stress tensor respectively. The lower surface of the plate was assumed to be under traction-free condition and the upper one was excited by a point force. The system was at rest for $t < 0$.

By using the Voigt's notation in which the stress and strain are represented in vector form, i.e., $\boldsymbol{\sigma} = \{\sigma_{11}, \sigma_{22}, \sigma_{12}\}^T$ and $\boldsymbol{\epsilon} = \{\epsilon_{11}, \epsilon_{22}, 2\epsilon_{12}\}^T$, the constitutive equation reads

$$\boldsymbol{\sigma} = \mathbf{C}\boldsymbol{\epsilon} + \boldsymbol{\eta}\dot{\boldsymbol{\epsilon}} \tag{3.12}$$

where $\mathbf{C}$ and $\boldsymbol{\eta}$ are, respectively, the elasticity and viscosity tensors defined by

$$\mathbf{C} = \begin{bmatrix} c_{11} & c_{11} - 2c_{44} & 0 \\ c_{11} - 2c_{44} & c_{11} & 0 \\ 0 & 0 & c_{44} \end{bmatrix} \tag{3.13}$$

and

$$\boldsymbol{\eta} = \begin{bmatrix} \eta_{11} & \eta_{11} - 2\eta_{44} & 0 \\ \eta_{11} - 2\eta_{44} & \eta_{11} & 0 \\ 0 & 0 & \eta_{44} \end{bmatrix}. \tag{3.14}$$

The velocities of compressional and shear waves in this isotropic solid medium are given by $c_p = \sqrt{c_{11}/\rho}$ and $c_s = \sqrt{c_{44}/\rho}$ respectively. The numerical solution of this problem was computed by a semi-analytical finite element method (Nguyen and Naili, 2011; Nguyen and Naili, 2012).

Wave fields for a 4-mm plate were simulated with the compressional wave speed, shear wave speed, and density of the plate being 2730 m/s, 1430 m/s, and 1180 kg/m^3 respectively. The properties are similar to those of Plexiglass. No absorption was assumed. The source wavelet had a time history given by

$$F(t) = F_0 e^{-4(f_c t - 1)^2} \sin(2\pi f_c t) \tag{3.15}$$

where $F_0 = 1$ N.m^{-2} and the center frequency f_c was 0.5 MHz. In order to resemble the experimental setup with angle beam transducers (Figure 3.4), the source is modeled by a force applied at 30° with respect to the normal i.e $\mathbf{F} = (-F\sin\theta, F\cos\theta)^T$ where $\theta = 30°$. Similarly, the simulated signals recorded at the receivers may be estimated as the projection of the simulated horizontal and vertical wave field components on a 30° inclined direction. A set of 64 ultrasound records was simulated with 0.0488 μs time increment, 1 mm spacing interval, and a minimum offset of 30 mm. The signals beyond 0.95 MHz were insignificant and removed by bandpass filter to avoid aliasing.

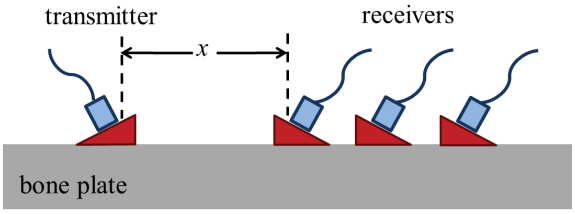

Figure 3.4: A schematic diagram shows the experimental setup for the bone-plate ultrasonic measurement. The transmitter is held stationary while the receiver is translated axially to acquire data. The offset is the source-receiver distance and denoted by x.

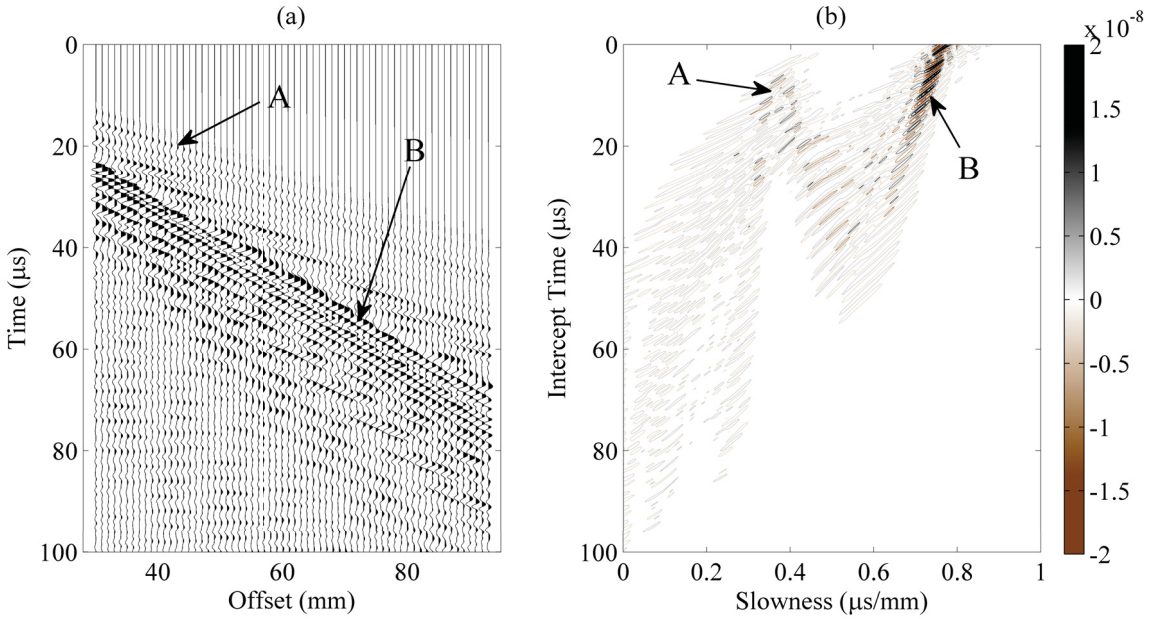

Figure 3.5: The τ-p transform of the simulated Plexiglass plate signals. (a) The non-gained wave fields in the t-x panel with true relative amplitudes. A points to the early-arriving high-speed (HS) bulk waves and B to the late-arriving low-speed (LS) guided waves. (b) The Radon signals.

The simulated signals for a 4-mm thick Plexiglass plate model is shown in Figure 3.5a. The data displays two major groups of wave arrivals propagating at two distinct phase velocities. The first group travels at higher speeds (HS) between 2.6 - 3.7 mm/μs and the amplitudes decay with distance. The HS arrivals include mainly bulk waves including direct arrivals and reflections.Le *et al.*, 2010 The second group of arrivals, which comes later in time, shows a dispersive wave train propagating at lower speeds (LS). The LS events exhibit the presence of surface and guided waves, which propagate between 1.4 - 1.6 mm/μs. These arrivals overlap and interfere with one another in the t-x domain but are clearly separated in the corresponding Radon panel (Figure 3.5b). The panel was computed from 0 μs/mm to 1 μs/mm with a step of 0.002 μs/mm. Each p-record represents a single ray parameter for all τ-values. The panel shows focused signal clusters with some strong Radon peaks between 0.3 - 0.8 μs/mm and at early time, perhaps up to 15 μs. The time intercept, measured at zero-offset, likely indicates reverberation events after 15 μs. The reflection events are hyperbolas in nature and thus mapped to ellipses between 0 and 0.5 μs/mm in the τ-p panel.Tatham, 1984 The LS guided wave events are more linear and mapped to τ-p region between 0.6 and 0.8 μs/mm. Figure 3.6 shows another perspective of the Radon peaks in an elevation plot. The Radon ridges are very locally concentrated and render the possible

phase velocities of traveling waves, demonstrating the use of the τ-p panel to extract wave fields based on traveling velocities.

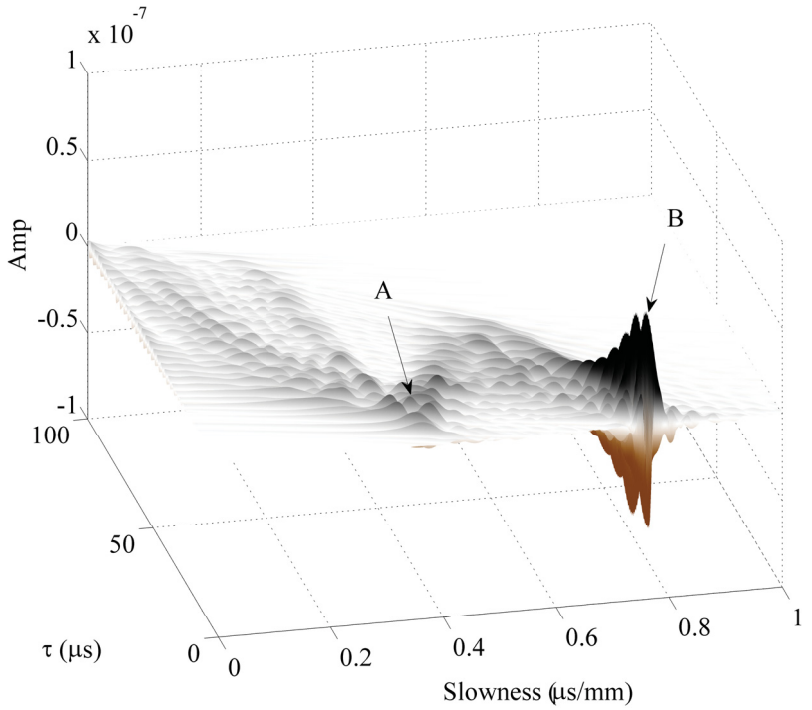

Figure 3.6: An elevation plot shows the Radon ridges. A and B point to signals described in the previous Figure 3.5.

The τ-p panel was split at $p = 0.5$ μs/mm ($c = 2000$ m/s) and the two separated Radon panels (one for $p \leq 0.5$ μs/mm and the other for $p > 0.5$ μs/mm) were reconstructed (Figure 3.7). The two t-x panels show two wave groups with distinct moveouts as shown in the original signals (Figure 3.5a). Moveout is the difference in travel times with respect to offset distance. The panels show the HS arrivals faster than 2000 m/s (Figure 3.7a) and the LS events slower than 2000 m/s (Figure 3.7b). I would like to point out the overlap of the HS and LS arrivals in the original data after 20 μs at small offsets, where the LS wave fields dominate. Attempt to isolate the LS signals by simply muting the rest of the t-x amplitudes fails to eliminate the hidden HS components. The results indicate the τ-p method has successfully separated the wave fields and also uncovered the HS wave fields embedded in the LS regime.

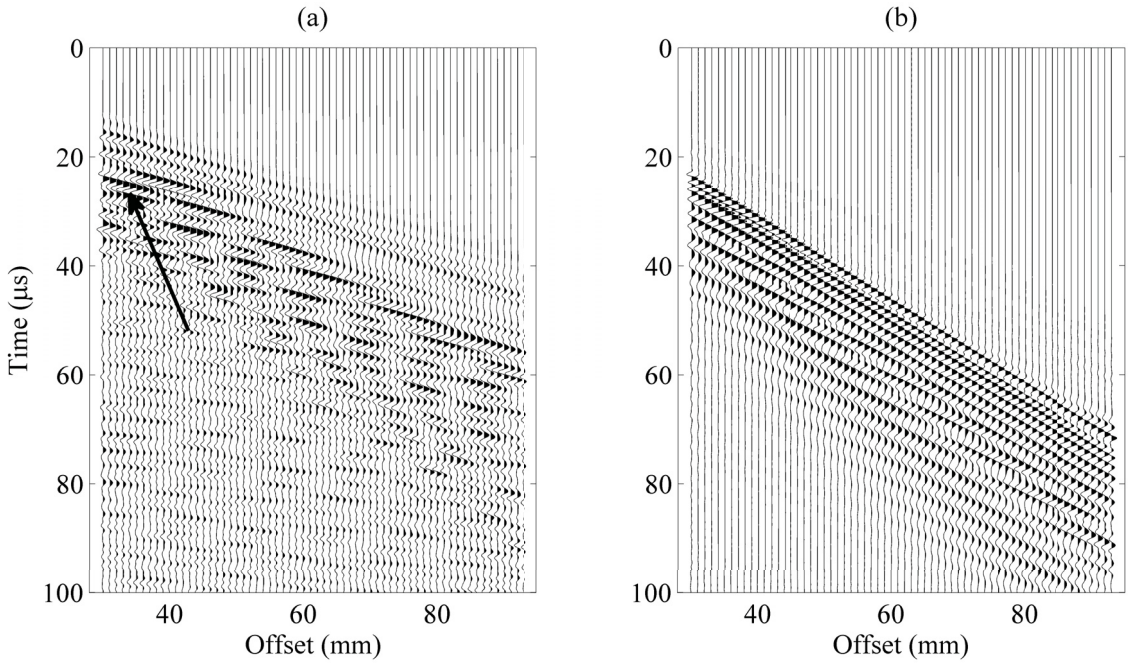

Figure 3.7: The Radon signals are separated at $p = 0.5$ μs/mm ($c = 2000$ m/s) and transformed back to the t-x domain using the filtered τ-p panels. (a) The reconstructed wave fields for $p \leq 0.5$ μs/mm and (b) for $p > 0.5$ μs/mm. The arrow points to the HS events which are recovered by the reconstruction. These signals are covered by the LS arrivals and thus are not visible in the original data.

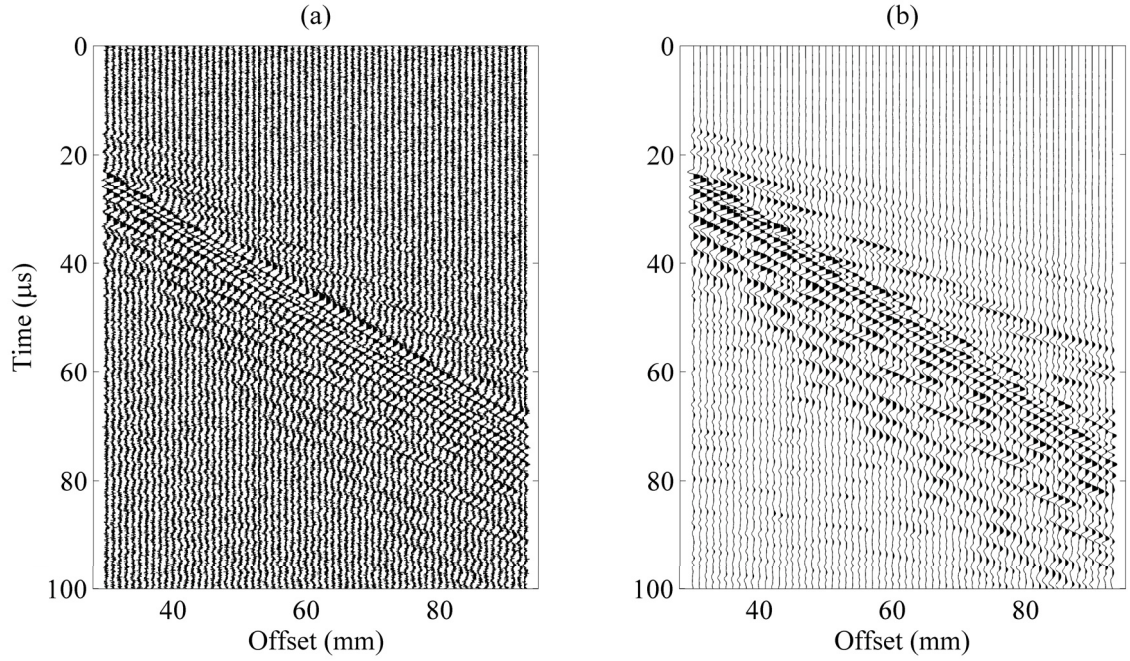

Figure 3.8: Noise suppression by the τ-p method. (a) The simulated signals are contaminated by white Gaussian noise. The SNR is 1. (b) The reconstructed signals show much better signal quality with strong coherent energy and the random noise is greatly attenuated.

To test the ability of the τ-p method to suppress noise, Gaussian noise was added to the simulated signals with unitary signal-to-noise ratio being 1 (Figure 3.8a). The data was τ-p transformed and inverted back to the t-x domain. The reconstructed wave fields (Figure 3.8b) show the noise is significantly attenuated while the signals are enhanced, thus increasing the SNR and improving the image quality. Slant-stacking the wave fields sums all amplitudes along a ray parameter. Coherent energies, which are in phase, are reinforced while incoherent arrivals such as noise, which are random and out of phases, are attenuated. The major arrivals, reconstructed after slant-stacking, are more coherent than the original data.

3.3.4 Application to Ex-vivo Experimental Data in Bone Plate

The experimental setup was an axial transmission configuration following Le *et al.*, 2010 (Figure 3.4). A bovine femur sample, which had a relatively flat surface area, was cut along the long axis to make a bone plate. The plate was cleaned, and the soft tissue and marrow were completely removed. The bone plate had dimensions 220 mm by 45 mm with mean thickness of 9 mm. Experiment was performed in air and at room temperature of 22°C. Two angle beam compressional wave transducers with 1 MHz center frequency (Panametrics C548, Waltham, MA) were attached to two angle wedges (Panametrics ABWM-7T-30 deg, Waltham, MA). One system acted as a stationary source and the other as a moving receiver. The source was pulsed by a Panametrics 5800 P/R (Panametrics, Waltham, MA). The recorded signal was digitized by and displayed on a 200 MHz digital storage oscilloscope (LeCroy 422 WaveSurfer, Chestnut Ridge, NY). A custom-built holder was used to clamp the bone plate in place, hold the transducers, and translate the receiving transducer along the bone sample at an uniform sampling interval. Ultrasound gel was applied on all contacts to ensure good coupling. Two steel bars, with two transducer-wedge systems attached to one end, applied constant pressure to the systems by their weights to maintain uniform coupling during the experiment. A set of 50 ultrasound records was measured with 1 mm spacing interval and 35 mm closest offset. The recorded data set was further decimated for a final sampling interval of 0.1 μs to form a t-x matrix $\mathbf{d}$.

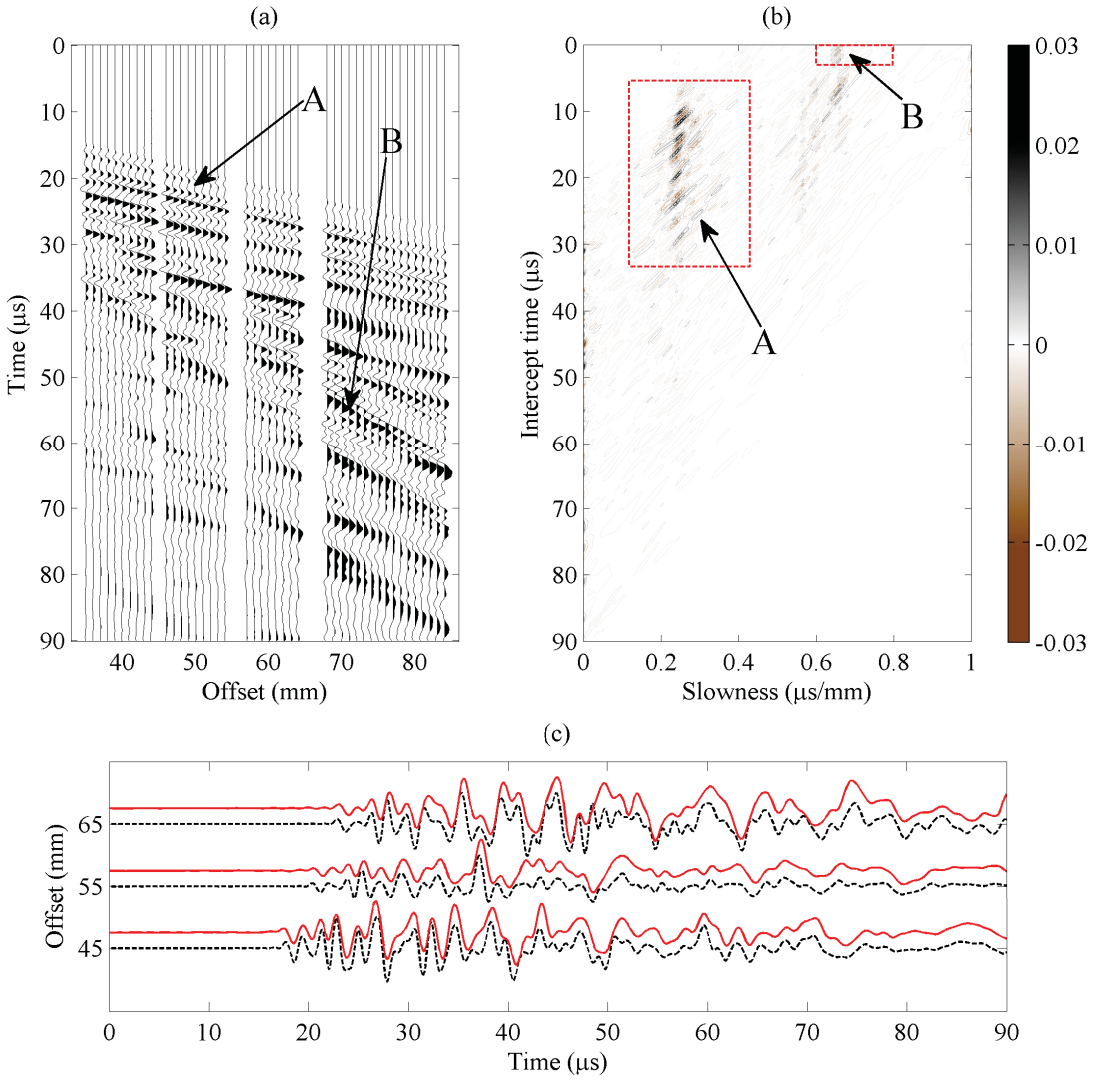

Figure 3.9: The τ-p transform of the bone-plate data. (a) The data has gaps, indicating 1, 2, and 3 missing records at three different spatial locations, 45 mm, 55-56 mm, and 65-67 mm respectively. A points to the high-speed (HS) bulk waves and B to the late-arriving low-speed (LS) guided waves. (b) The τ-p signals. The two rectangles enclose the Radon signals used to reconstruct Figure 3.11b and 3.11c. (c) Comparison between the measurement (dashed) and the reconstruction (solid) of the missing records.

The amplitudes of the ultrasound signals are modified by many factors as they propagate through the medium. These factors are, namely, amplitude decay with distance, material absorption, scattering, and energy partition at the interface. The net effect of these factors upon the signal amplitudes can be approximated by a decay function. Time-gain compensation (TGC) is a process attempting to reverse the attenuation effects and recover the "true" signal amplitudes by multiplying the amplitudes of the data by the inverse of the decay function. In this work, I chose to multiply the amplitudes of the data points by

their corresponding travel times, i.e., I gained the signals linearly. However, TGC amplifies the late-arriving signals for each time series but is not adequate to boost the overall signal strength of the series when the offset is large, i.e., when the receiver is far away from the transmitter. In this situation, I normalize each time series by its own maximum absolute amplitude, which is known as self-normalization. The bone-plate data was linearly gained and self-normalized (Figure 3.9a). After self-normalization, the relative amplitudes between time series is lost but this is not particularly important because the normalization does not destroy the coherency of the existing wave fields, which is important for the τ-p transform.

A trapezoidal bandpass filter with corner frequencies: 0.005, 0.05, 0.8, 0.95 MHz was used. Even though the records were acquired at regular spacing along the long axis (or x-axis), some data gaps consisting of 6 missing records were purposely created to illustrate the ability of the τ-p method to handle irregular spatial sampling. This is very practical in some acquisition situations where either bad records are obtained or data can not be acquired at some locations due to surface conditions. There are three gap sizes: 1, 2, and 3 mm. Similar to the simulated Plexiglass plate signals, two main groups of arrivals, the HS and LS waves, are also observed with different moveouts. The HS multiple reflections, which come at the same time as the LS events, interfere with the LS wave fields and are not visible. The Radon panel (Figure 3.9b) shows two strong signal clusters around 0.25 and 0.65 μs/mm, which correspond to the HS and LS waves in the data. The p-axis was sampled every 0.002 μs/mm. Also shown are the reconstruction of the missing records at three indicated offsets (Figure 3.9c). The reconstructed signals compare well with the real data and follow their phases. The good match between the originally acquired signals and the reconstructed missing records by the τ-p transform demonstrates the interpolation ability of the method to reconstruct missing data.

To further analyze the bone-plate data, dispersive energy is extracted by using the f-p Radon panel and replacing slowness by phase velocity, i.e., $c = 1/p$ (Figure 3.10). The c-values were interpolated to ensure that the c-axis of the f-c panel was regularly sampled. The dispersion diagram shows three small amplitude clusters. Their associated dispersion trajectories are segmented and not easily traceable. The low frequency cluster (labeled as 1) is the fundamental $A0$ Lamb mode of a plate (Rose, 1999) while the other two strong higher-order modes (labeled as 2 and 3) are associated with the HS arrivals. The f-c panel is very noisy including much incoherent energy and the $A0$ dispersion curve lacks the continuity.

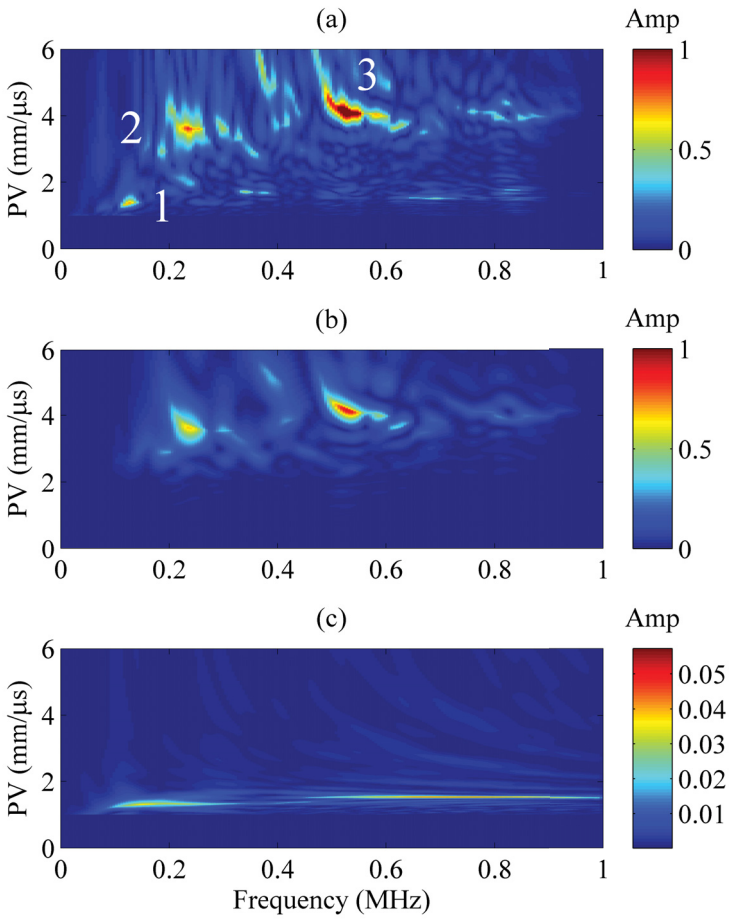

Figure 3.10: The f-c panels or dispersion curves. (a) The dispersion curves of the bone data as shown in Figure 3.9a; The three strongest amplitude clusters are labeled as 1, 2, and 3. (b) The dispersion curves of the filtered HS wave fields. The energy of this panel is made up of the Radon signals within the large rectangle in Figure 3.9b. (c) The dispersion curves of the filtered LS $A0$ mode. The dispersion curve of this mode is more continuous than its presence in the original dispersion curves. The energy of this mode comes from a small bundle of Radon signals within the small rectangular window in Figure 3.9b.

A filtering operation on the τ-p panel was attempted to separate and enhance the dispersive energies of the three dispersive modes. To enhance the higher-order modes, a window 5 - 35 μs and 0.1 - 0.45 μs/mm (the large rectangular area in Figure 3.9b) was applied to isolate the Radon signals while muting the rest of the panel. The windowed Radon signals were then Fourier transformed in time from τ-p to f-p space. The filtering process has greatly focused the dispersive energies of the two modes (Figure 3.10b). Their dispersion curves are more traceable. I further used a small amount of Radon signals bounded by 0 - 2 μs and 0.6 - 0.8 μs/mm (the small rectangular window in Figure 3.9b) to reconstruct the dispersion of the $A0$ mode (Figure 3.10c). The f-c curve thus obtained

shows superior continuity over the one shown in the original data, which is weak and very segmented.

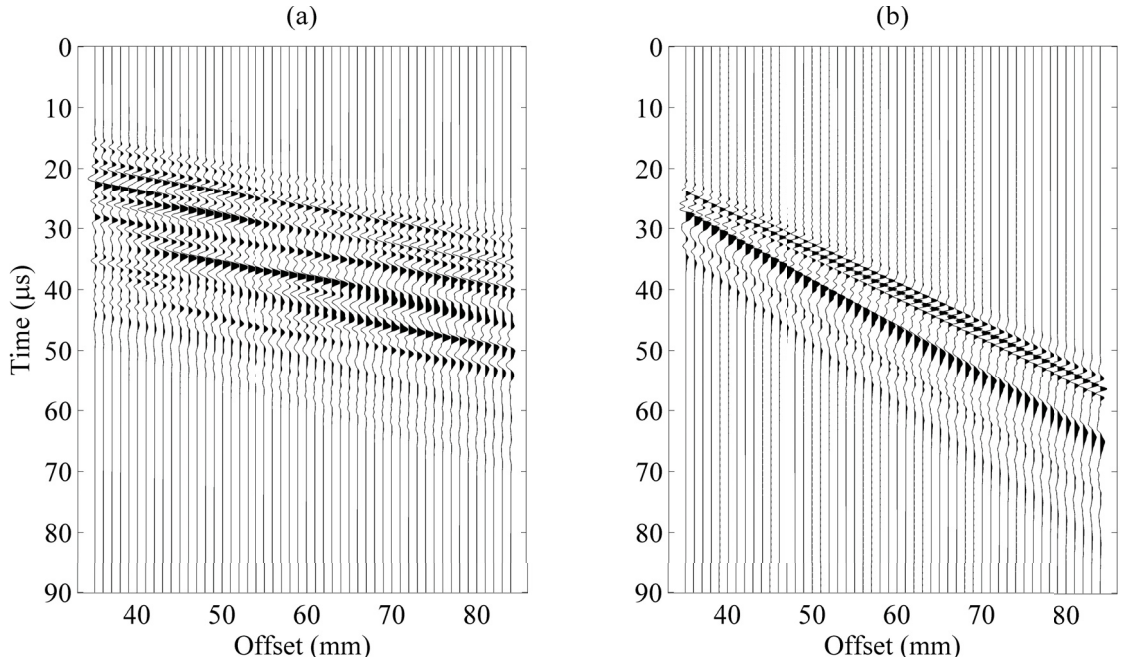

Figure 3.11: The reconstructed wave fields: (a) The HS wave fields corresponding to the Radon signals within the large rectangular window of Figure 3.9b; (b) The LS $A0$ wave fields reconstructed with the Radon signal within the small rectangular area in Figure 3.9b. The missing records are also filled at locations: 45 mm, 55-56 mm, and 65-67 mm respectively.

The reconstructed wave fields corresponding to the three modes are shown in Figure 3.11. During the inversion process, the Radon operator $\mathbf{L}$ was re-sampled with the spatial locations of the missing records and thus, the missing records were interpolated. The wave fields are separated with proper velocity ranges. The HS wave fields, which are not identified before due to overlapping with the LS waves, are recovered (Figure 3.11a). The wave fields are more coherent after τ-p filtering and show a mixture of low and high frequency components. As shown in the f-c panel, the two higher-order modes are in two different frequency regimes: one low at 230 kHz and one high at 550 kHz, but travel with similar phase velocity around 4000 m/s, which is also evidenced by the parallel arrivals of different frequencies with similar moveouts (Figure 3.11a). The speed of the $A0$ mode increases at low frequencies and reaches a plateau after 150 kHz (Figure 3.10c). The fact that the high-frequency components travel faster than the low-frequency components is also supported by the highly dispersive wave trains consisting of the early-arriving, fast-traveling, and high-frequency waves, and the late-arriving, slowly-traveling, and low-frequency wavelets (Figure 3.11b).

3.3.5 Discussions

I have described an iterative algorithm to compute the high-resolution τ-p or Radon transform to process multi-channel ultrasound data. Conceptually, the t-x data are stacked along a range of ray parameters, p, for each zero-offset time intercept to produce a τ-p map. During the stacking process, random noise is significantly attenuated due to their incoherency and randomness but the coherent energy is reinforced, thus greatly enhancing the SNR. The wave modes are separated based on their time intercepts and slownesses in the τ-p panel. Since the linear Radon transform is used, the stacking is best to focus energy along a linear trajectory. Guided waves are, at least locally, linear events while reflections are hyperbolic. However, if the layer thickness is much less than the acquisition range, the reflections are also approximately linear. Further, hyperbolic Radon transform can be used if necessary (Gu and Sacchi, 2009).

The transform does not require the t-x data to be regularly sampled along the offset axis. However, data gap can be interpolated. During the reconstruction process, the offset axis can be re-sampled, the x-values of the missing records can be inserted, and Radon operator $\mathbf{L}$ can be re-sampled to reconstruct missing records, thus filling the data gap.

Random t-x signals appear as scatter Radon signals in the Radon panel while coherent signals show up as strong signal clusters. Ignoring the scatter signals in the Radon panel while keeping the strong clusters will suppress incoherent energies, such as noise, in the reconstructed t-x data. However, reconstruction of the coherent signals is dependent on the size of the filter-window in the Radon panel. The window size is adjusted according to the time intercept at zero-offset and slowness of the guided mode of interest for extraction. If the τ-range is too large, many unwanted early- and late-arriving events are included. If p-range is too big, the reconstructed events are highly dispersive as the results consist of many events of different speeds. In practice, the main clusters of energies responsible for the modes of interest can be identified. However, the choice of window size around the clusters still remains to be subjective and requires some trial-and-error to achieve good results.

The value of the hyper-parameter, μ affects the accuracy of the reconstructed wave fields. As mentioned in Section II, a very small μ-value leads to accurate waveform reconstruction since the prediction error (Equation 3.6) is minimized, but the Radon-focusing is less ideal. A 0.1 μ-value was used to separate the wave fields in Figures 3.3d-3.3e and a unit μ-value was used to reconstruct the missing records in Figure 3.9c. Conversely, a large μ-value images the Radon energies with much higher resolution as the regularization term is now

emphasized, but as expected, the data misfit is large as well. The μ-value takes the value of the number of p-values, which is 701 for the simulated data and 501 for the bone plate data. A preferred method of choosing the μ-value is the usage of the L-curve (Engl and Grever, 1994). I also found that 4 iterations were sufficient to produce good results.

Table 3.1: Sampling parameters for the three data sets used in Section 3.3 Wavefield Separation

Data Set	$\Delta\tau$ (μs)	Δp (μs/mm)	Δx (mm)	f_{max} (MHz)	r_{max} (mm)	P (μs/mm)
Two events	2	0.1	2	.04	100	10
Plexiglass plate	0.05	0.002	1	0.95	63	1
Bone plate	0.1	0.002	1	0.95	50	1

Since the method involves two transforms: Fourier and Radon, the temporal and spatial sampling should follow the Nyquist criteria to avoid alias.Turner, 1990 Aliasing is associated with insufficient sampling and results in data artifacts. The sampling intervals and other parameters relevant to the three data sets are tabularized in Table 3.1 where $\Delta\tau$, Δp, Δx, f_{max}, r_{max}, and P are, respectively, the time step, the slowness resolution, the receiver spacing, maximum frequency, offset range, and slowness range. Using the values provided, these parameters can be verified to satisfy the following sampling requirements:

$$\Delta\tau \leq \frac{1}{2f_{max}}, \tag{3.16}$$

$$\Delta p < \frac{1}{r_{max} f_{max}}, \tag{3.17}$$

and

$$\Delta x < \frac{1}{P f_{max}}. \tag{3.18}$$

In case the spatial sampling is not regular, Δx takes the largest spatial interval in the data.

In summary, a new application of the τ-p transform to study multi-channel ultrasound data in the Radon domain has been investigated. The array processing methodology, which is based on a high-resolution linear Radon transform algorithm, is not widely used in non-destructive testing to the best of my knowledge and this study is considered novel in the material characterization using ultrasound. The Radon domain renders a new τ-p panel to

discriminate ultrasound energies of various traveling wave modes based on the time intercept and slowness. The results have demonstrated, using simulated and *ex-vivo* data sets, that the Cauchy-norm regularization offers enhanced resolution over the damped least-squares and the high-resolution method is very successful to attenuate noise, enhance coherent linear arrivals, and separate wave fields with different moveouts. The accuracy of the reconstructed wave fields has also been verified. Using a windowed Radon panel, the method is able to unfold the t-x wave fields which are previously overlapped and concealed by different arrivals. In addition, the technique is considered a powerful alternative to the Fourier-based techniques such as the conventional f-k filtering because it can handle irregularly sampled data and is capable to reconstruct a regularly sampled grid. This will open up an arena to apply the proposed method to a wide range of ultrasonic guided wave applications.

3.4 Dispersion Curve Imaging

3.4.1 Introduction

Ultrasonic guided waves have seen many successful industrial applications in nondestructive evaluation and inspection. Guided wave testing technologies have been applied to material inspection, flaw detection, material characterization, and structural health monitoring (Rose, 2004). Surface wave methods (Temsamani *et al.*, 2002; Cawley *et al.*, 2003; Masserey *et al.*, 2006; Tsuji *et al.*, 2012) have also received much popularity to characterize near surface materials in shallow geological prospects, structural engineering, and environmental studies. Surface or guided waves require a boundary or structure for their existence. Their propagation is constrained to the near surface or within the structure. These waves are generated by the interaction of elastic waves (compressional, P- and shear, S-waves) with the boundaries. For guided waves within a plate, waves are multiply reflected at the boundaries with mode-conversions, i.e., $P \rightarrow S$ or $S \rightarrow P$. The boundaries facilitate multiple reflections and also guide the wave propagation; the waveguide also retains the guided wave energy and keeps it from being spread out, thus allowing the guided waves to travel over long distances within the plate (Lowe, 2002). The plate vibrates in different vibration modes, which are known as guided modes.

Guided modes are dispersive and travel with velocities which vary with frequency. The velocity of a guided mode depends on the material properties, thickness, and frequency. Dispersion curve, which describes their relationship, is fundamental to the guided wave analysis. The dispersion curve can be obtained by finding a solution to the homogeneous

elastodynamic wave equation (Rose, 1999). The displacement vectors, $\mathbf{N}$, are first assumed general forms with unknown constants. This leads to a set of equations for the unknowns in matrix form, $\mathbf{M} \cdot \mathbf{N} = 0$, where $\mathbf{M}$ is the coefficient matrix of elastic constants, densities, thickness of the structure, wavenumber, and frequency. The dispersion or characteristic equation of guided modes is obtained by setting the determinant of $\mathbf{M}$ equal to zero, i.e., $|\mathbf{M}(\omega, k)| = 0$ where ω is the angular frequency and k is the wavenumber. The characteristic equation is nonlinear and numerical solutions are usually sought.

In recent years, quantitative ultrasound has been applied to characterize material properties of long bones *in vitro* (Camus *et al.*, 2000; Lefebvre *et al.*, 2002; Lee and Yoon, 2004; Zheng *et al.*, 2007; Ta *et al.*, 2009; Le *et al.*, 2010; Li *et al.*, 2013; Tran *et al.*, 2013). Axial transmission technique is the most common method to study long bones. The measurement places the transmitter and receiver on the same side of the bone sample. Usually two transducers is employed where one transducer is a stationary transmitter and the other transducer is moved away from the transmitter at a regular spacing interval to receive the signal. An ultrasound acquisition system with one array probe (Minonzio *et al.*, 2010; Nguyen *et al.*, 2013) and also two array probes (Nguyen *et al.*, 2014) have also been used. The acquisition configuration has been applied successfully by (Le *et al.*, 2010) to analyze bulk waves arriving at close source-receiver distances. Quantitative guided wave ultrasonography (QGWU) is particularly attractive because of the sensibility of guided waves to geometrical, architectural, and material properties of the cortex. The cortex of long bone is a hard tissue layer bounded above and below by soft tissue and marrow, resulting in high impedance-contrast interfaces and therefore is a natural waveguide for ultrasonic energy to propagate. Albeit the studies using guided waves are limited, the results so far suggest the potential use of QGWU to diagnose osteoporosis and cortical thinning. The use of ultrasound to characterize bone tissues and evaluate bone strength has gained some success. A recent publication provides some updates in experimental, numerical, and theoretical results on the topics (Laugier and Haiat, 2011).

Multi-channel dispersive energy analysis requires a reliable mapping of the ultrasound data from the two dimensional time-distance (t-x) space to the frequency-wavenumber (f-k) space. The mapping is usually performed by the two-dimensional Fourier transform (Alleyne and Cawley, 1991). The frequency-phase velocity (f-c) space can later be obtained by substitution and interpolation via $c = \omega/k$. The 2D-FFT based spectral analysis has been used to study dispersive energies of guided waves propagating along the long bones; however, the extracted dispersion curves lack the resolution in the transformed space (f-k

or f-c) to discriminate wave-modes. The resolving power associated with the 2D-FFT is linked to the limited aperture of the recorded data. Due to limited aperture, the energy information is spread or smeared and the smearing makes the identification of the dispersive modes difficult. In clinical studies, the spatial aperture is limited by the accessibility of the adequate skeleton length, regularity of the measuring surface, length of the ultrasound probe, and the number of channels. Several techniques have been attempted with some success to improve the resolution of the dispersion curves, such as using 2D-FFT combining with autoregressive model (Ta *et al.*, 2006*b*), group velocity filtering (Moilanen *et al.*, 2006), and singular value decomposition (Minonzio *et al.*, 2010).

Radon transform owes its name to the Austrian mathematician Johann Radon (1917) and is an integral transform along straight lines, which is known as slant stack in geophysics. The inverse Radon transform is widely used in tomographic reconstruction problems where images are reconstructed from straight line projections such as X-Ray computerized assisted tomography (Herman, 1980; Louis, 1992). The use of RT to process ultrasound data is very few. Most recently, RT was used to perform ultrasonic Doppler vector tomography to reconstruct the blood flow distribution (Jansson *et al.*, 1997) and to detect line-like bone surface orientations in ultrasound images (Hacihaliloglu *et al.*, 2011).

Mcmechan and Yedlin, 1981 generated the first phase velocity dispersion curves based on RT of the seismic wave fields. The data was first slant-stacked (Radon transformed) to the slowness-intercept (p-τ) domain, which is then followed by a Fourier transform into the slowness-frequency (p-f) plane. However, the extracted energies were significantly smeared and the dispersion trajectories had poor resolution. The low-resolution dispersion map showed the neighboring modes cluster together, making the modal identification a difficult task. Over a decade, various computational strategies (see for example Trad *et al.*, 2002; Sacchi, 1997) have been developed in the geophysics community to improve the Radon solutions with enhanced resolution. Recently, Luo *et al.*, 2008*a*; Luo *et al.*, 2008*b* successfully used the high-resolution Radon solution developed by Trad *et al.*, 2002 to image dispersive Rayleigh-wave energies in geophysical surface-wave data. Nguyen *et al.*, 2014 applied an adjoint Radon transform to study guided wave dispersion in brass and bone plates.

In this section, the linear Radon transform is applied to extract dispersive information from ultrasound long bone data. Three solutions of linear Radon transform: standard or adjoint Radon transform (ART), damped least-squares Radon transform (LSRT), and high-resolution Radon transform (HRRT) are presented. The resolution of the RT solutions and FT solution is compared using a dispersive wave-train data set. Finally I apply the Radon

transform to image the dispersion curves from the recorded ultrasound wave fields from a cervine long bone. To my knowledge, this is the first time RT is used to analyze the ultrasound wave fields propagating in long bones (Le *et al.*, 2013; Nguyen *et al.*, 2014). I demonstrate the advantages and robustness of RT in the following aspects: the RT does not require regular channel spacing; it can handle missing records; it requires a smaller aperture of the recorded data; the HRRT has much better resolving power over the conventional FT and other RT solutions.

3.4.2 Simulation Experiment

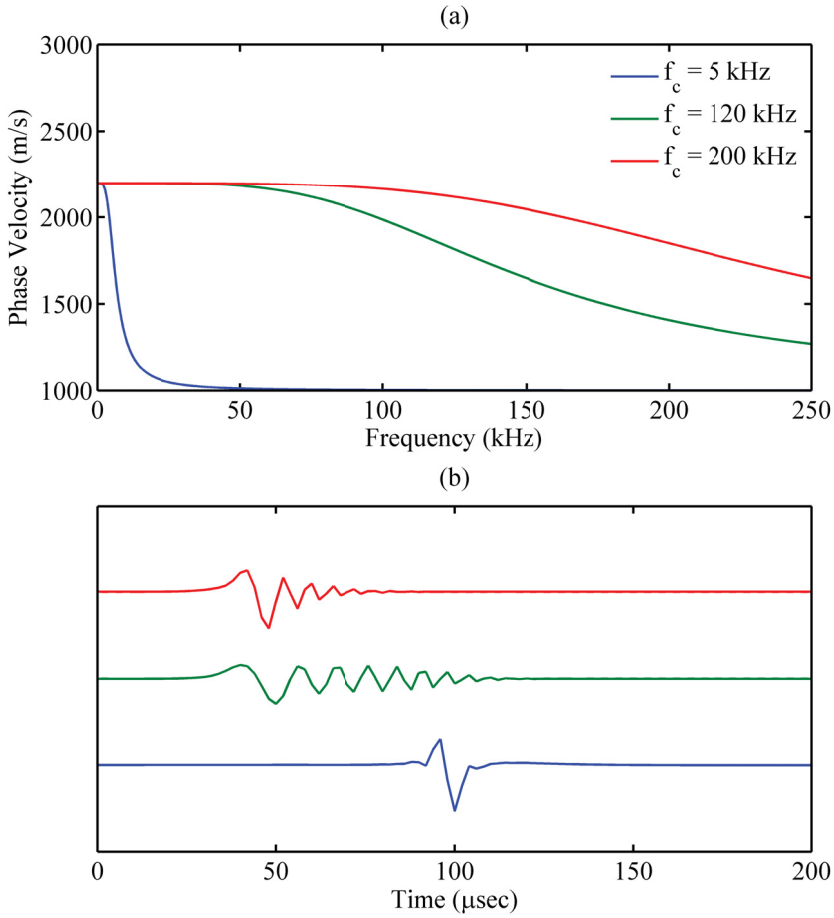

Figure 3.12: Simulated dispersion. (a) The dispersion curves for three f_c-values: 5 kHz, 120 kHz, and 200 kHz. (b) The corresponding trapezoidal wavelets.

A linear dispersive wave train is simulated with the following spectrum

$$S(f) = W(f)e^{[-i2\pi f(\frac{x}{c(f)} - t_0)]} \tag{3.19}$$

where $W(f)$ is the spectrum of the source wavelet and t_0 is a time constant. The phase velocity, $c(f)$, is described by

$$c(f) = c_{min} + (c_{max} - c_{min})/\sqrt{1 + (f/f_c)^4} \tag{3.20}$$

where c_{min} is the minimum phase velocity, c_{max}, the maximum phase velocity, and f_c, the critical frequency. The spread, $\Delta c = c_{max} - c_{min}$, and the critical frequency, f_c, determine the amount of dispersion in the data. There is no dispersion when $(f/f_c)^4 << 1$. The time signal, $s(t)$, is recovered from $S(f)$ by the inverse FFT.

The wavelet, $W(f)$, has a trapezoidal amplitude spectrum and a 90° phase shift. The corner frequencies of the spectrum are 5 kHz, 10 kHz, 120 kHz, and 195 kHz respectively where the signals within the 10-120 kHz band are not attenuated. The minimum and maximum phase velocities are 1000 m/s and 2200 m/s respectively. The effect of f_c upon the dispersion and simulated time signals is illustrated in Figure 3.12. The 5-kHz-f_c gives rise to a sharp drop in phase velocity within 0-50 kHz and the corresponding time signal is simple with one cycle. The 120-kHz-f_c, which yields larger variation in phase velocity within the same frequency band than the 200-kHz-f_c, generates a more complicated dispersive wave train. Since I want to investigate how well the RT images dispersive energies, I choose 120 kHz as the critical frequency.

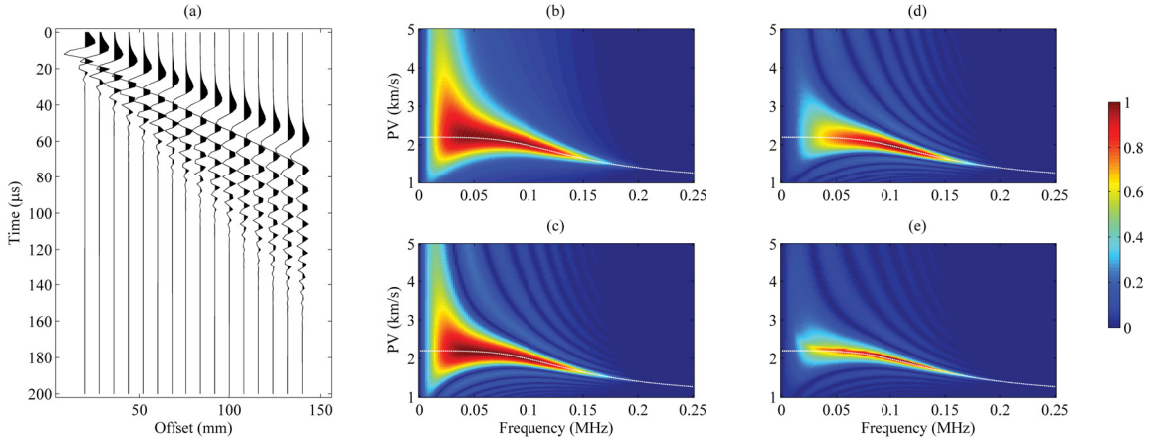

Figure 3.13: Simulated dispersive signals and the corresponding (f-c) dispersion panels: (a) noise-free signals; (b) 2D fast Fourier transform panel; (c) adjoint Radon panel; (d) damped least-squares Radon panel; (e) high-resolution Radon panel. The true dispersion is described by the white dashed curve.

64 time series (or records) of dispersive wave trains were simulated to validate the performance of Radon transform to image the dispersion curve. The series are spaced 1 mm apart and has 101 points, each with a 2-μs sampling interval. Every four records is plotted

for a total of 16 records in Figure 3.13a. The records show dispersive signals of mixed frequencies and the low-frequency components traveled faster than the high frequency components, which is consistent with the simulated dispersive curve (the 120-kHz-f_c curve in Figure 3.12a. Different frequencies have different traveling speeds and thus different traveling times. When the offset was small, the frequencies traveled close together. As the offset increased, the difference in traveling times became larger, and the frequencies separated, showing a fanning wave train with offset. The corresponding dispersion panels (Figures 3.13b-3.13e) show the dependence of phase velocity (PV) resolution on the transform techniques used. Among the four, the Fourier panel (FP) (Figure 3.13b) has the worst PV resolution as the dispersive energy spreads far away from the true dispersion curve (indicated by the white dashed curve in Figure 3.13) for frequencies within 10-120 kHz. The smearing is most severe for frequencies lower than 50 kHz. The main PV spectra have long tails and do not seem to have local extrema. The adjoint Radon panel (ARP) (Figure 3.13c) has slightly better resolution than the FP. The LSRT (Figure 3.13d) improves the focusing better than the ART. The HRRT (Figure 3.13e) focuses the dispersive energy even better, offering sharper image of the dispersion and superior resolution than the other three methods. The HRRT confines the energy to a narrower band, not far from the predicted dispersion curve. The Radon panels have alternating dark and light blue areas, indicating side-lobes with local extrema in the PV spectra.

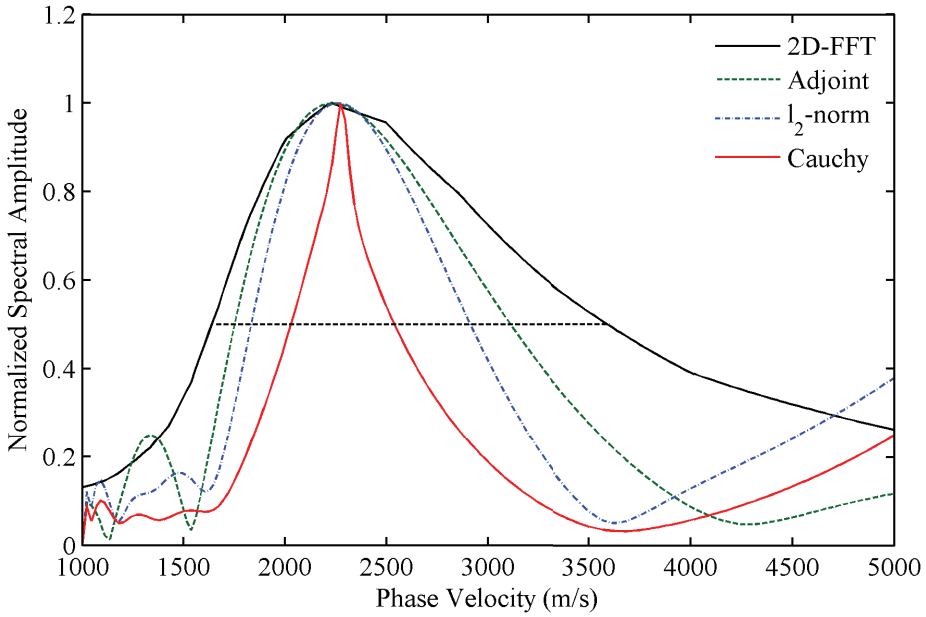

Figure 3.14: Phase velocity spectra at 0.04 MHz and the corresponding full-width at half-maximum measurements.

The transform methods imaged the PV spectrum as broad spectra rather than narrow lines. The amount of energy spreading across a range of phase velocity values is different for each transform method. The spreading characteristic is denoted by the PV resolution of the transform method and can be quantified by the full-width at half-maximum (FWHM) of the PV spectrum. The FWHM is the full width of the PV spectrum measured at one-half of the maximum height of the peak. Poor energy resolution or large FWHM value means that the transform is not capable of localizing or focusing the energy. As an example, Figure 3.14 shows the self-normalized PV energy spectra at 40 kHz. The FWHM-values for the FT, ART, LSRT, and HRRT are 1940 m/s, 1360 m/s, 1080 m/s, and 515 m/s respectively. Among all, the FT has the poorest resolution. The FWHM_{FT} is 40% larger than FWHM_{ART}, 80% larger than $\text{FWHM}_{\text{LSRT}}$, and 280% larger than $\text{FWHM}_{\text{HRRT}}$. This indicates that the ART, LSRT, and HRRT offers 40%, 80%, and 280% better resolution respectively than the FT. Among the Radon solutions, the HRRT yields 164% and 110% better resolution than the ART and LSRT respectively.

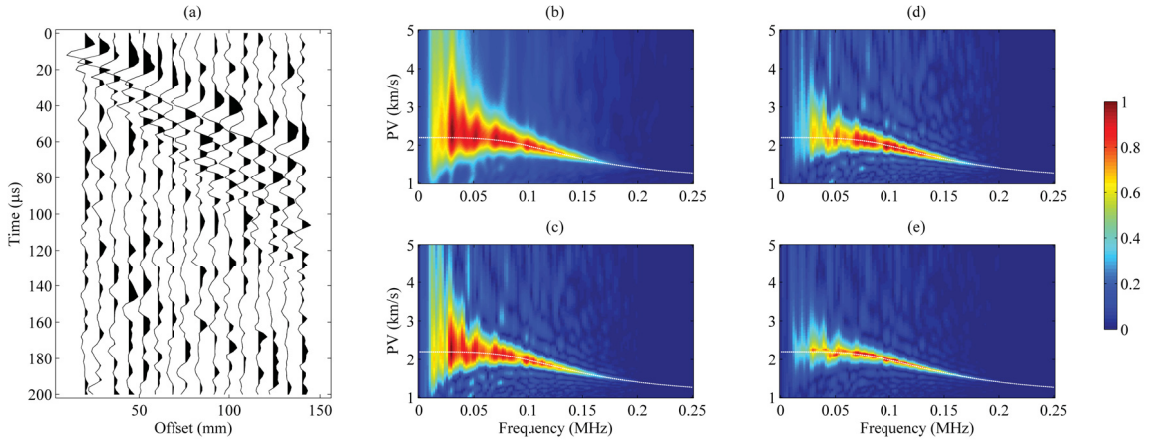

Figure 3.15: Simulated dispersive signals with random noise and the corresponding (f-c) dispersion panels: (a)noisy signals with 10 dB SNR; (b) 2D fast Fourier transform panel; (c) adjoint Radon panel; (d) damped least-squares Radon panel; (e) high-resolution Radon panel. The true dispersion is described by the white dashed curve.

I also applied the methods to image dispersive energies in the presence of random noise (Figure 3.15). The noisy data was generated by adding white Gaussian noise to the noise-free signals with signal-to-noise ratio of 10 dB. The dispersive signals were disrupted by the presence of noise (Figure 3.15a). The tracks of the imaged dispersion are less continuous (Figures 3.15b-3.15e) but visible. As in the noise-free case, the FT (Figure 3.15b) dispersed the energy and had difficulty to confine it, thus rendering poor imaging resolution while

the HRRT (Figure 3.15d) imaged the dispersion with enhanced resolution than the other methods.

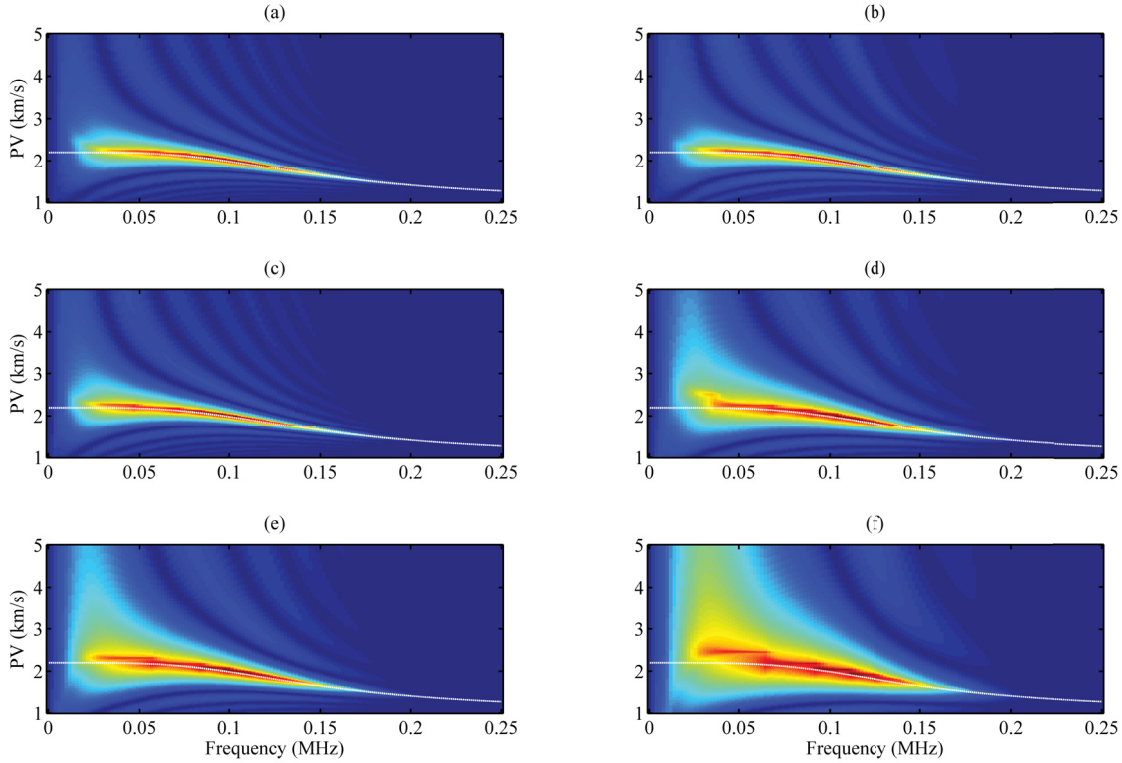

Figure 3.16: Imaging simulated dispersive energy with different data apertures by the HRRT. (a) same data set as in Figure 3.13a, 126 mm aperture with 64 2-mm-spaced records; (b) 126 mm aperture, the same data as in (a) with 6 missing records at 40, 70, 72, 100, 102, and 104 mm respectively; (c) 124 mm aperture with the first 32 4-mm-spaced records; (d) 62 mm aperture with the first 32 2-mm-spaced records; (e) 60 mm aperture with the first 16 4-mm-spaced records; (f) 30 mm aperture with the first 16 2-mm-spaced records.

Similar to FT, the RT also depends on aperture. I explore here the performance of the RT to image the data with limited aperture (Figure 3.16). Since the HRRT has the best imaging resolution among the three other Radon methods, I used the HRRT hereafter. I examined the PV dispersion within the frequency range 10-120 kHz where the frequency components were not attenuated. The aperture is defined by the difference between maximum and minimum offsets. The original reference data has 64 2-mm-spaced records with a 126-mm aperture and Figure 3.16a shows the reference RP. Next I purposely removed six records from the original data to make the spatial sampling non-uniform but keeping the aperture fixed at 126 mm. The RP (Figure 3.16b) closely resembles the original panel (Figure 3.16a) without visual difference. I skipped every two records in the original data to incur larger spacing ($\Delta x = 4$ mm) while keeping the aperture at 124 mm, close to the

original aperture. The dispersion profile (Figure 3.16c) looks similar to the original profile (Figure 3.16a) with a slight increase in PV spread. Next, I considered halving the aperture to 62 mm by taking the first 32 records of the original data. At small aperture, the resultant dispersion profile (Figure 3.16d) suffers energy spreading and the smearing increases with the decrease of frequency. The same smearing effect was observed for Figure 3.16e where I skipped every four records of the original data to keep 16 records with a 4-mm spacing and a similar aperture of 60 mm to the previous case (Figure 3.16d). These two data sets (Figures 3.16d-3.16e) have similar apertures (60 mm versus 62 mm) and their dispersion profiles look similar even though they have different number of records (16 versus 32) and spacing (2 mm versus 4 mm). Last, I lowered the aperture further down to 30 mm (half of the previous two cases) by keeping the first 16 records of the original data. The dispersion panel (Figure 3.16f) shows a lack of energy confinement and severe spreading far away from the true solution. Also, the imaged dispersion track is segmented, discontinuous, and stepwise, yielding an aliased image, which might erroneously implicate the existence of several modes. Clearly, changes in aperture size cause more severe smearing effect than reducing the number of records for a fixed aperture size.

3.4.3 Ex-vivo Experiment

The bone sample was a 23-cm long diaphysis of a cervine tibia acquired from a local butcher shop. The overlying soft tissue and the marrow of the sample were removed and the sample was then CT-scanned for cortex-thickness measurement. Based on the X-ray computed tomographic (CT) image (Figure 3.17a), the top cortex had an average thickness of 4.0 mm (minimum 3.6 mm and maximum 4.5 mm) for the section where the transducers were deployed. The surface of the sample was reasonably flat. The experiment setup shows the bone sample was firmly held at both ends by the grabbers of a custom-built device (Figure 3.17b). Two 1-MHz angle beam compressional wave transducers (Panametrics C548, Waltham, MA) were attached to two angle wedges (Panametrics ABWM-7T-30 deg, Waltham, MA). The transducer-wedge systems were positioned linearly on the same side of the bone sample. One system acted as a transmitter and the other as a receiver. The experiment was carried out at 21°C room temperature. Ultrasound gel was applied on all contacts as coupling agent. Constant pressure was applied to the wedges by the use of two steel bars to ensure good contact between interfaces. The transmitter was pulsed by a Panametrics 5800 P/R (Panametrics, Waltham, MA) and the recorded signals were digitized and displayed by a 200-MHz digital storage oscilloscope (LeCroy 422 WaveSurfer, Chestnut

Ridge, NY). The digitized waveforms were averaged 64 times to increase the signal-to-noise ratio. The receiver was moved away from the transmitter by 1 mm with a minimum offset of 39 mm and 90 records were acquired. The sampling interval, after decimation, was 0.1 μs. The total duration of each record was 150 μs. The recorded signals formed a 1500×90 time-distance (t-x) matrix of amplitudes.

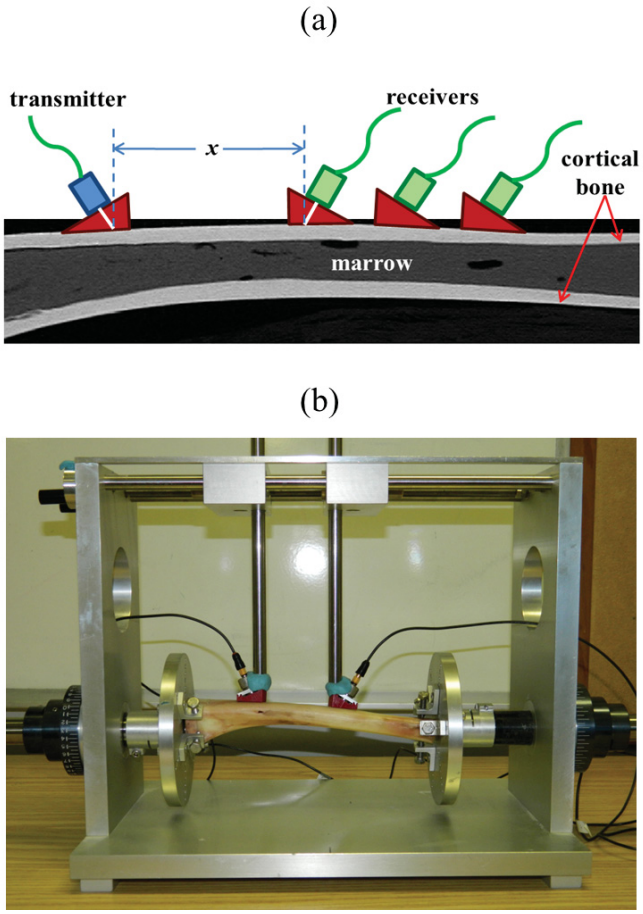

Figure 3.17: The *ex-vivo* experimental setup. (a) A sagittal computed tomography image of the cervine bone sample. Also shown is the schematic of the transducer layout on the bone surface. The receiving transducer is moved away axially and collinearly from the transmitter 1-mm increment. (b) The physical setup of the experiment. The setup shows a device with grabbers at both ends to hold the bone sample firmly in place by screws. The two steel bars are used to provide constant pressure to the transducer/wedge systems against the bone surface.

The cervine tibia data shown in Figure 3.18a consists of 90 records with a 89-mm aperture and 39-mm minimum offset. The processing steps involved bandpass filtering, linear gain, and self-normalization. The corner frequencies of the bandpass window were 0.005 MHz, 0.03 MHz, 0.8 MHz, and 1.0 MHz while the last two processing steps made

the small late-arriving and/or far-offset signals visible. The t-x panel shows mainly two types of arrivals with distinct moveouts. The first type is usually the high-frequency and high-velocity (HFHV) bulk waves (Le *et al.*, 2010) and the second type is the low-frequency and low-velocity (LFLV) arrivals, which are usually surface or Lamb-type guided waves (Ta *et al.*, 2009). At close offset, the HFHV bulk waves dominated. Between 40-55 mm, there was a lack of LV guided wave energy buildup due to short offset. The LV signals started to become more visible after 60 mm offset. At offset $>$ 100 mm, the low-velocity arrivals took over and became quite dominated. The HV bulk waves decayed very quickly with offset and lost their strength after 80 mm. These observations are also evidenced in the corresponding power spectral map (Figure 3.18b). Between 40-70 mm, the data was rich of high-frequency (average 0.8 MHz) bulk waves. The data lost the high frequencies quickly due to amplitude decay with distance and preferential filtering due to absorption. Between 70-100 mm, the frequency content of the signals dropped to a midrange of approximate 0.35 MHz and the signals were a mixture of HV and LV waves. After 100 mm, the 0.1-MHz signals took over and the guided wave energies built up strongly, showing clear evidence of the presence of late-arriving LFLV wave modes.

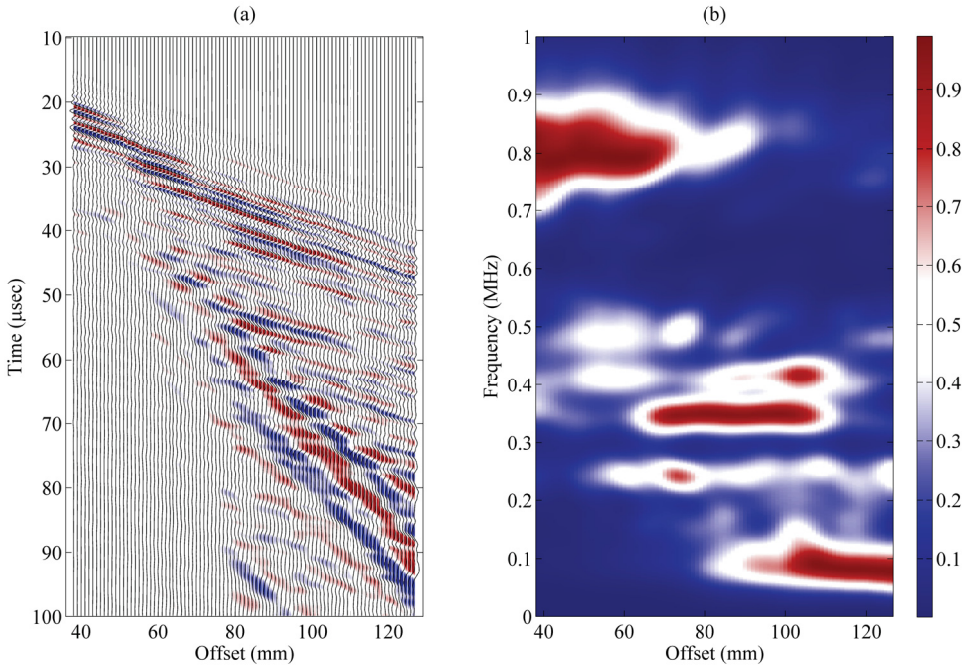

Figure 3.18: Cervine tibia bone sample: (a) self-normalized and linearly-gained t-x signals; (b) the corresponding power spectral density map.

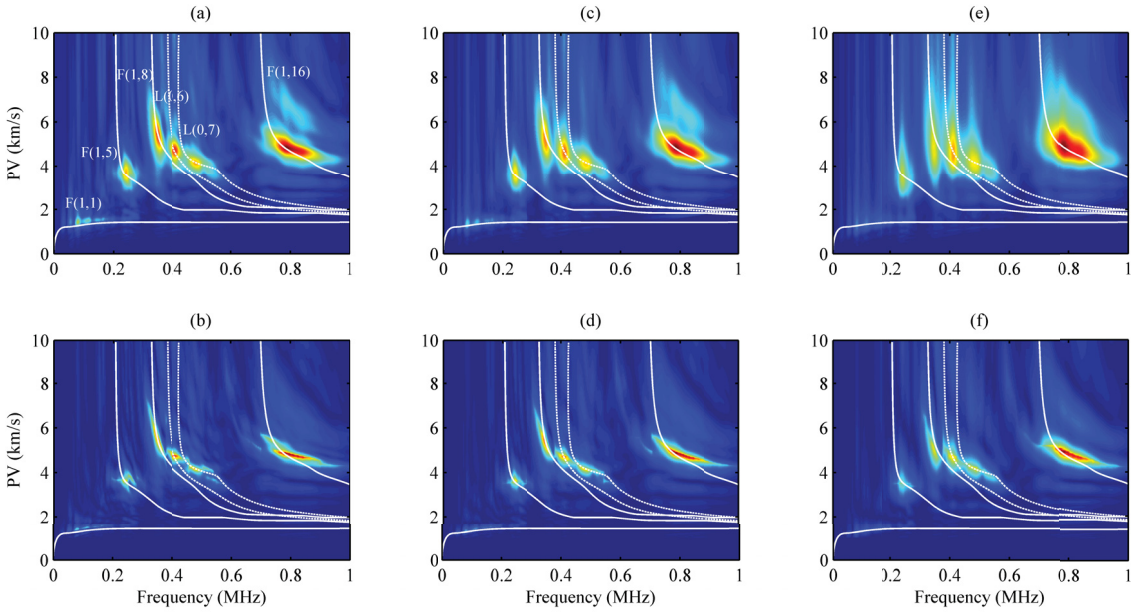

Figure 3.19: Dispersion f-c panels: (a, c, e) conventional Fourier panels; (b, d, f) Radon panels. From left to right, the number of ultrasonic records are 90, 64, and 32, corresponding to 89 mm, 63 mm, and 31 mm apertures, respectively. The theoretical dispersion curves are shown in white.

Using the real data, I examined the performance of the FT and HRRT to extract dispersive energy when the aperture decreased from 89 mm to 31 mm. There are at least six strong energy loci in both panels (Figures 3.19a-3.19f). To interpret the guided modes, I simulated dispersion curves with the commercial software package DISPERSE version 2.0.16i (Imperial College, London) developed by Pavlakovic and Lowe (2001). The model was a water-filled cylinder with a 4.4-mm thick cortex and a 6.35-mm inner radius. The density, longitudinal wave velocity, and shear wave velocity of the cortex were 1930 kg/m^3, 4000 m/s, and 2000 m/s respectively (Le *et al.*, 2010) while the density and longitudinal wave velocity of water were 1000 kg/m^3 and 1500 m/s. Six guided modes were identified with confidence: $F(1,1)$, $F(1,5)$, $F(1,8)$, $F(1,16)$, $L(0,6)$, and $L(0,7)$. With the exception of the $F(1,1)$ mode, all modes are clearly seen in all panels. The $F(1,1)$ was quite weak and its presence faded when only 32 records were used (Figures 3.19e-3.19f). When the data aperture decreased from 89 mm to 31 mm, the resolution of the FPs (Figures 3.19a, 3.19c, and 3.19e) deteriorated with significant energy smearing. For example, at 0.8 MHz, the FWHM of the $F(1,16)$ increases from 927 m/s at 89 mm aperture (Figure 3.19a) to 1935 m/s at 31 mm aperture (Figure 3.19e), which is a greater-than two-fold increase in smearing or loss in resolution. At 31 mm aperture (32 records), the FT lost resolution as the $F(1,8)$, $L(0,6)$, and $L(0,7)$ tended to cluster together (Figure 3.19e). In contrast, the

RPs fared much better than the FPs. All the RPs show good confinement of the modal energies. When the aperture decreased, energy smearing occurred but was not as severe as was the FT case. Similarly the FWHM also shows a two-fold increase from 286 mm to 573 mm when the aperture decreased from 89 mm (Figure 3.19b) to 31 mm (Figure 3.19f). Even though only 32 records were used (Figure 3.19f), the three concerned modes, $F(1,8)$, $L(0,6)$, and $L(0,7)$ were well separated in the RPs.

3.4.4 Discussions

The above experiments were conducted to demonstrate the ability of the linear Radon (or τ-p) transform to image the dispersive guided wave energies in long bones, which makes the work novel. The transform was implemented using a least-squares strategy with Cauchy-norm regularization that serves to improve the focusing power, *i.e.*, to enhance resolution in the transformed domain. The proposed HRRT has also been compared with the conventional temporal-spatial Fourier transform to validate the superiority of the method. Multi-channel dispersive energy analysis requires a reliable mapping of the ultrasound data from the t-x domain to the f-k domain. The mapping is usually performed by the conventional 2D-FFT. However, the extracted dispersion curves lack the resolution in the transformed plane to discriminate wave modes (Moilanen, 2008; Sasso *et al.*, 2009).

The resolving power associated with the FT is linked to the spatial aperture of the recorded data (Ta *et al.*, 2006*a*; Moilanen, 2008). The acquisition aperture is finite, leading to a windowing or truncation on the x-axis. Truncating the x-axis is equivalent to convolving the x-space with a sinc function. Consider a boxcar function, $f(x)$ of width a where $f(x) = 1$ for $-\frac{a}{2} \leq x \leq \frac{a}{2}$ and 0 elsewhere. The width of the box, a, is the "aperture". The Fourier transform of a boxcar is a sinc function, $F(k) = a\frac{\sin(ka/2)}{(ka/2)}$ with the main spectrum bounded by the zeros: $-\frac{2\pi}{a}$ and $\frac{2\pi}{a}$. The distance between the zeros, or zero-distance is $\frac{4\pi}{a}$. As the aperture (a) increases, the zero-distance decreases, and the width of the spectrum becomes smaller or narrower, thus improving the resolution in the k-space. This simple illustration shows the resolution-dependence of the 2D-FFT method on the spatial aperture of the acquired data.

In clinical studies of human long bones where spatial acquisition range is restricted due to the limited dimension of the ultrasound probe, the number of channels, irregularity of the acquisition surface, and the accessibility to the skeletal site, the 2D-FFT method may not provide sufficient resolution. The RT, which also depends on the spatial aperture of the data, has a smaller aperture threshold. Given the same spatial aperture, I have shown

the HRRT dispersion maps are far much better resolved than those of the conventional 2D-FFT. While the RT has a smaller aperture tolerance than the FT method, a small 31-mm aperture in the simulation case shows dispersion artifacts (Figure 3.16f), which is absent in the real data case for the similar aperture. Nevertheless, the HRRT provides an alternative new approach to image limited-aperture data and estimate spectral information. The resolving power of the HRRT will be beneficial for the guided mode identification and separation in *in-vivo* studies where the overlying soft tissue layer increases the number of guided modes and mode density (Tran *et al.*, 2013).

High-resolution spectral analysis via Burg maximum entropy method (Marple, 1987), multiple signal classification (MUSIC) (Schmidt, 1986) or minimum variance method (MVM) (Capon, 1969) can also be used to estimate high-resolution spectra by applying those methods to spatial data for each temporal frequency. The f-k energy computed by these methods could be mapped to the f-p plane to obtain the desired energy distribution for the dispersive signals. However, the aforementioned methods will only give a high-resolution image of the modal energies in the f-p plane that cannot be used to come back to data (t-x) space . The Radon transform approach, on the other hand, permits to design an operator that can be used to return to the t-x domain. This is important because one can obtain high-resolution images in the f-c space by plotting the absolute values of the complex $\mathbf{M}(f,c)$ but can also use $\mathbf{M}(f,c)$ to recover $\mathbf{D}(t,x)$ via the Radon forward operator, $\mathbf{L}$.

The acquired data contains linear (direct waves, head waves, and surface waves) and hyperbolic (reflections) events. By using a linear Radon transform, I assumed all events were linear. In the consideration of the short offset configuration and a thin cortex, the close-offset portions of the reflection events (or the t-x curves) are approximately linear and thus the assumption is valid. Further, hyperbolic Radon transform can be used if necessary (Gu and Sacchi, 2009).

The HRRT maps the t-x signals to a high-resolution dispersion diagram without requiring the spatial space to be evenly sampled. Solving the problem using inverse-problem technique allows the HRRT to be used for accurate missing data reconstruction or interpolation in practice. To reconstruct the missing records, the offset axis is re-sampled, the spatial coordinates of the missing records are inserted, and the Radon operator $\mathbf{L}$ is re-sampled to interpolate missing records or fill the data gap. It is important to note that it is quite simple to use the HRRT in cases where the data are irregularly sampled. This is also true for the Fourier methods where one could replace the FFT by a non-uniform discrete FT (Sacchi and Ulrych, 1996). However, a non-uniform discrete FT is a non-orthogonal

transform and therefore, an inversion process similar to the one outlined for the HRRT is required to have a transform that allows us to go from t-x to f-k and return back to t-x domain. This problem was addressed by Sacchi and Ulrych, 1996.

The HRRT is also robust in enhancing signal coherency and canceling noise. Because the amplitudes are summed along a linear moveout, random noise is significantly attenuated due to its incoherency and randomness but the coherent energy is reinforced, thus greatly enhancing the SNR. Generally, solving inverse problems takes a considerable computation time due to iteration. For the data sets used in this study, four iterations were found to be sufficient to yield reasonable results. For instance, it took less than one minute to provide a dispersion diagram in this study using a quad-core Windows 7 64-bit computer with Intel Core Q6600 2.40 GHz CPU and 4 Gb RAM. Increasing the number of iterations consumes more computation time.

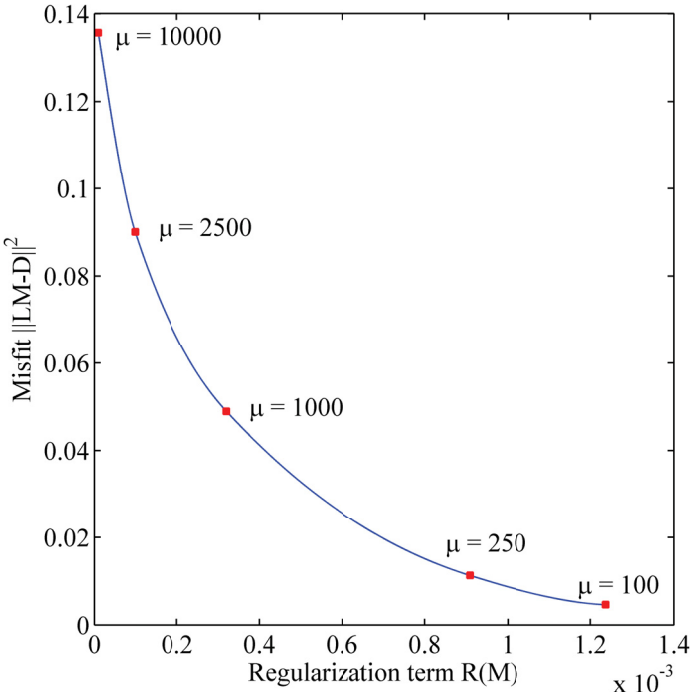

Figure 3.20: Example of an L-curve for the noise-free simulated data set (Figure 3.13a). The regularization and misfit terms of the L-curve were given by Equation 3.6.

The hyper-parameter μ of the cost function, given by Equation 3.6, controls the degree of fitting the predicted observations to the acquired data. A small μ-value leads to a solution with minimized prediction error, but the focusing power of the transform is less ideal. Conversely, if μ-value is large, the Radon energies will be imaged with higher resolution as the regularization term is now emphasized, but the data misfit will be large as well. A

preferred method of choosing the μ-value is the usage of the L-curve (Engl and Grever, 1994), which is illustrated in Figure 3.20. The L-curve is a plot of the regularization term versus the data misfit. The optimal value of μ corresponds to the "elbow" point of the L-curve, where the curvature is maximal. For both the LSRT and HRRT, I used a μ-value of 1000 for the simulated data and 15000 for the bone data.

Aliasing is associated with insufficient sampling resulting in data artifacts. To avoid aliasing, RT should obey the following sampling guidelines. The temporal and spatial sampling are related by the Nyquist criteria (Turner, 1990) and provided by Equations 3.16 and 3.18. The slowness resolution, Δp, is given by Equation 3.17. The sampling intervals and other parameters that are relevant to the simulation and bone data sets, are tabularized in Table 3.2.

Table 3.2: Values of the relevant parameters pertaining to the data used in Section 3.4 Dispersion Curve Imaging

Data Set	$\Delta\tau$ (μs)	Δp (μs/mm)	Δx (mm)	f_{max} (MHz)	r_{max} (mm)	P (μs/mm)
Simulation	2	0.004	2	0.195	126	0.8
Bone sample	0.1	0.002	1	1	89	1

The HRRT technique provides a powerful high-resolution tool to image the multi-channel ultrasonic dispersive energy in long bones. Applications to numerical and *ex-vivo* experimental data sets have demonstrated the feasibility and robustness of the method. Although the guided modes are distinguishable in both FPs and RPs using the *ex-vivo* data in this study, the HRRT shows a more powerful resolving power, constraining the dispersive energies of the guided modes within their well-delineated tracks. Therefore, the application of HRRT will be beneficial for more complex cases where the modes come close together. The HRRT handles smaller aperture and requires less records, which do not have to be evenly spaced. In addition, the HRRT has the added-on advantage to enhance SNR by reducing random noise. This method should be considered as a preferred method to carry out the multi-channel dispersion analysis of ultrasonic guided wave data in long bones, where the recording aperture is limited due to practical constraints. The success of this study opens a bright roadmap to a wide range of RT applications in the field of processing ultrasonic guided wave data in long bones.

Chapter 4

Dispersion Simulation & Sensitivity Analysis

4.1 Simulation of Dispersion Curve

A semi-analytical finite element (SAFE) scheme has been developed for accurately computing the velocity dispersion and attenuation in a trilayered system consisting of a transversely-isotropic cortical bone plate sandwiched between the soft tissue and marrow layers. The soft tissue and marrow are mimicked by two fluid layers of finite thickness. A Kelvin-Voigt model accounts for the absorption of all three biological domains. The simulated dispersion curves are validated by the results from the commercial software DISPERSE and published literature. Finally, the algorithm is applied to a viscoelastic trilayered TI bone model to interpret the guided modes of an *ex-vivo* experimental data set from a bone phantom.

4.1.1 Problem Formulation by Semi-Analytical Finite Element (SAFE) Method

4.1.1.1 Geometry of the Model

A solid layer, extending infinitely along the $\boldsymbol{x}_1$ direction (Figure 4.1), represents the cortical bone plate with a constant thickness h (domain $\Omega^b = \{(x_1, x_2); -h \leq x_2 \leq 0\}$). The anisotropic bone plate is sandwiched between the overlying soft tissue and the underlying marrow layer. Their respective domains are denoted by Ω_1^f ($\Omega_1^f = \{(x_1, x_2); 0 \leq x_2 \leq h_1\}$) and Ω_2^f ($\Omega_2^f = \{(x_1, x_2); -(h + h_2) \leq x_2 \leq -h\}$), where h_1 and h_2 are the thicknesses of the soft tissue and marrow layers respectively. The plane interfaces between the bone (Ω^b) and the fluids (Ω_1^f and Ω_2^f) are denoted by Γ_1^{bf} and Γ_2^{bf} respectively.

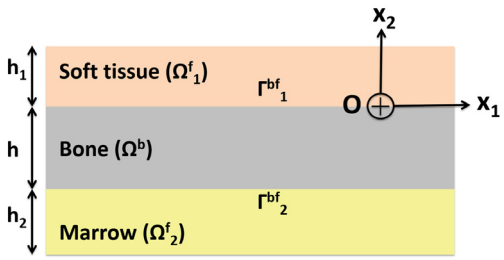

Figure 4.1: Geometry of the trilayered bone model.

4.1.1.2 Governing Equations and Boundary Conditions

Both soft tissue and marrow layers are modeled as acoustic fluid media with dissipation. The dissipation mechanism is assumed to be small and due only to viscosity without memory effects (Sasso *et al.*, 2007; Naili *et al.*, 2010). The linearized wave equations of wave propagation in both domains Ω_1^f and Ω_2^f are

$$\rho_\alpha \ddot{p}_\alpha - K_\alpha \nabla^2 \left(p_\alpha + \gamma_\alpha \dot{p}_\alpha\right) = 0, \quad \forall\, \boldsymbol{x} \in \Omega_\alpha^f,\ (\alpha = 1, 2) \tag{4.1}$$

where p_α $(\alpha = 1, 2)$ denotes the acoustic pressure in Ω_α^f; K_α and ρ_α are the bulk modulus at rest and the mass density of the fluid, respectively; γ_α denotes the viscosity coefficient; single dotted and double dotted symbols indicate the first and second order time derivatives respectively. Thus the wave velocity in Ω_α^f is $c_\alpha = \sqrt{K_\alpha/\rho_\alpha}$.

In Ω^b, the displacement vector is denoted by $\boldsymbol{u}(\boldsymbol{x}, t) = \{u_1, u_2\}^T$ while the stress and strain vectors are $\boldsymbol{\sigma} = \{\sigma_{11}, \sigma_{22}, \sigma_{12}\}^T$ and $\boldsymbol{\epsilon} = \{\epsilon_{11}, \epsilon_{22}, 2\epsilon_{12}\}^T$ respectively. Then the dynamic equilibrium equation is

$$\rho\ \ddot{\boldsymbol{u}} - \mathbb{L}^T \boldsymbol{\sigma} = \mathbf{0} \tag{4.2}$$

where ρ is the mass density and the operator $\mathbb{L}$ is defined by

$$\mathbb{L} = \mathbf{L}_1 \partial_1 + \mathbf{L}_2 \partial_2, \quad \mathbf{L}_1 = \begin{bmatrix} 1 & 0 \\ 0 & 0 \\ 0 & 1 \end{bmatrix}, \quad \mathbf{L}_2 = \begin{bmatrix} 0 & 0 \\ 0 & 1 \\ 1 & 0 \end{bmatrix} \tag{4.3}$$

with ∂_1 and ∂_2 being the spatial derivatives along the $\boldsymbol{x}_1$ and $\boldsymbol{x}_2$ directions respectively.

The constitutive law describing the Kelvin-Voigt viscoelastic behavior of the bone is

$$\boldsymbol{\sigma} = \mathbf{C}\ \boldsymbol{\epsilon} + \boldsymbol{\eta}\ \dot{\boldsymbol{\epsilon}}, \quad \boldsymbol{\epsilon} = \mathbb{L}\ \boldsymbol{u}, \tag{4.4}$$

where $\mathbf{C}$ and $\boldsymbol{\eta}$ are the elasticity and viscosity tensors respectively (Nguyen and Naili, 2012). I recall that the material properties of the trilayered system depend only on x_2, i.e. $\rho = \rho\ (x_2)$, $\mathbf{C} = \mathbf{C}\ (x_2)$ and $\boldsymbol{\eta} = \boldsymbol{\eta}\ (x_2)$.

Regarding the boundary conditions, the normal velocity and stresses are continuous at the fluid-solid interfaces, i.e.

$$\left.\begin{aligned} &\partial_2(p_\alpha + \gamma_\alpha \dot{p_\alpha}) = -\rho_\alpha \ddot{u}_2, \\ &\{\sigma_{12}, \sigma_{22}\}^T = \{0, -(p_\alpha + \gamma_\alpha \dot{p}_\alpha)\}^T, \end{aligned}\right\} \quad \forall\, \boldsymbol{x} \in \Gamma_\alpha^{bf} \quad (\alpha = 1, 2) \tag{4.5}$$

where $\{\sigma_{12}, \sigma_{22}\}^T$ is the traction. The free boundary conditions for fluid layers are

$$p_\alpha = 0, \quad \forall\, \boldsymbol{x} \in \Gamma_\alpha^f \quad (\alpha = 1, 2). \tag{4.6}$$

4.1.1.3 Corresponding Equations in Frequency-Wavenumber Domain

I look for solutions of harmonic waves propagating along the axial direction $\boldsymbol{x}_1$ in the following form

$$p_\alpha(x_1, x_2, t) = \tilde{p}_\alpha(x_2) e^{\mathrm{i}(k_1 x_1 - \omega t)}, \tag{4.7}$$

$$\boldsymbol{u}(x_1, x_2, t) = \tilde{\boldsymbol{u}}(x_2) e^{\mathrm{i}(k_1 x_1 - \omega t)}, \tag{4.8}$$

where $i^2 = -1$, ω is the angular frequency, and k_1 denotes wavenumber in $\boldsymbol{x}_1$ direction. $\tilde{p}_\alpha(x_2)$ and $\tilde{\boldsymbol{u}} = (\tilde{u}_1, \tilde{u}_2)^T$ represent the amplitudes of pressure and displacement vector in the fluid and solid respectively. By substituting Equation 4.7 into Equation 4.1, the equations in the fluid layers become

$$\left(-\rho_\alpha \omega^2 + k_1^2 \bar{K}_\alpha\right) \tilde{p}_\alpha - \bar{K}_\alpha \partial_2^2 \tilde{p}_\alpha = 0, \quad \forall\, \boldsymbol{x} \in \Omega_\alpha^f, \ (\alpha = 1, 2) \tag{4.9}$$

where $\bar{K}_\alpha = K_\alpha(1 - \mathrm{i}\omega\gamma_\alpha)$. Similarly, substituting Equation 4.8 into Equation 4.2 leads to

$$-\rho\omega^2 \tilde{\boldsymbol{u}} - \tilde{\mathbb{L}}^T \tilde{\boldsymbol{\sigma}} = \mathbf{0} \tag{4.10}$$

where $\tilde{\mathbb{L}} = \mathrm{i}k_1 \mathbf{L}_1 + \mathbf{L}_2\, \partial_2$.

The corresponding constitutive law is

$$\tilde{\boldsymbol{\sigma}} = \mathrm{i}k_1 \bar{\mathbf{C}} \mathbf{L}_1 \tilde{\boldsymbol{u}} + \bar{\mathbf{C}} \mathbf{L}_2\, \partial_2\, \tilde{\boldsymbol{u}}. \tag{4.11}$$

where $\bar{\mathbf{C}} = \mathbf{C} - \mathrm{i}\omega\boldsymbol{\eta}$. The interface conditions are

$$\partial_2 \tilde{p} = \bar{\rho}_\alpha\, \omega^2 \tilde{u}_2, \quad \{\tilde{\sigma}_{12}, \tilde{\sigma}_{22}\}^T = \{0, -(1 - \mathrm{i}\omega\gamma_\alpha)\tilde{p}_\alpha\}^T \tag{4.12}$$

where $\bar{\rho}_\alpha = \rho_\alpha/(1 - \mathrm{i}\omega\gamma_\alpha)$. For each values of (ω, k_1), Equation 4.10 can be rewritten as

$$\left(-\omega^2 \mathbf{A}_1 + k_1^2 \mathbf{A}_2\right) \tilde{\mathbf{u}} - \mathrm{i}k_1 \left(\mathbf{A}_3 + \mathbf{A}_3^T\right) \partial_2 \tilde{\mathbf{u}} - \mathbf{A}_4 \partial_2^2 \tilde{\mathbf{u}} = \mathbf{0} \tag{4.13}$$

where the matrices $\mathbf{A}_1$, $\mathbf{A}_2$, $\mathbf{A}_3$, and $\mathbf{A}_4$ are defined by

$$\mathbf{A}_1 = \rho\mathbf{I}, \quad \mathbf{A}_2 = \mathbf{L}_1^T \bar{\mathbf{C}}\, \mathbf{L}_1, \quad \mathbf{A}_3 = \mathbf{L}_2^T \bar{\mathbf{C}}\, \mathbf{L}_1, \quad \mathbf{A}_4 = \mathbf{L}_2^T \bar{\mathbf{C}}\, \mathbf{L}_2. \tag{4.14}$$

4.1.1.4 The SAFE Formulation of the Characteristic Equation

A detailed SAFE derivation for the dispersion characteristic equation is presented in Appendix B. The characteristic equation of an infinite viscoelastic plate coupled with fluids (B.18) can be written as

$$\left[\mathbf{K}_1 + k_1^2\mathbf{K}_2 + \mathrm{i}k_1\mathbf{K}_3\right]\ \mathbf{V} = \mathbf{0}, \tag{4.15}$$

where $\mathbf{V} = (\mathbf{P}_2, \mathbf{U}, \mathbf{P}_1)^T$, $\mathbf{P}_\alpha$ $(\alpha = 1, 2)$, and $\mathbf{U}$ are the global pressure and displacement fields or global wave structures. I rearrange (Equation 5.1) in order to have a linear eigen-value problem in the following form

$$\left(\begin{bmatrix} \mathbf{0} & \mathbf{K}_1 \\ \mathbf{K}_1 & \mathrm{i}\mathbf{K}_3 \end{bmatrix} - k_1 \begin{bmatrix} \mathbf{K}_1 & \mathbf{0} \\ \mathbf{0} & -\mathbf{K}_2 \end{bmatrix}\right)\ \begin{pmatrix} \mathbf{V} \\ k_1\mathbf{V} \end{pmatrix} = \mathbf{0}. \tag{4.16}$$

By solving (Equation 4.16) for each value of ω, I can determine the eigen-values k_1 and their associated eigen-vectors, $\mathbf{V}(\omega,k_1)$ of guided modes. The frequency-dependent phase velocity (c_p) and attenuation (att), in Np/m, of a guided mode are obtained from k_1 using the following relationships

$$c_\mathrm{p} = \frac{\omega}{\mathsf{Re}(k_1)}, \quad \mathrm{att} = \mathsf{Im}(k_1) \tag{4.17}$$

where $\mathsf{Re}()$ and $\mathsf{Im}()$ are the real and imaginary parts of a complex quantity.

Conventionally, the group velocity c_g is determined by taking the derivatives of the ω-k relationship, i.e $c_\mathrm{g} = \partial\omega(k_1)/\partial k_1$. However, as mentioned in Bernard *et al.*, 2001, this definition of group velocity is only valid in undamped waveguides. For damped waveguides, it is more appropriate to evaluate the energy velocity V_e along the propagation direction. The energy velocity is defined by the ratio between the time-average of Poynting vector and the time-average of the energy density, i.e.

$$V_e = \frac{\int_\Omega \langle \boldsymbol{P} \cdot \mathbf{x}_1 \rangle \, \mathrm{d}x_2}{\int_\Omega \left(\langle E_p \rangle + \langle E_k \rangle\right) \mathrm{d}x_2} \tag{4.18}$$

where $< . >= \frac{1}{T}\int_0^T (.)dt$ is the time-averaging operator and $T = 2\pi/\omega$ is the period of the considered harmonic wave. The time-averaged Poynting vector, strain and kinetic energy densities, i.e., $\langle \boldsymbol{P} \rangle$, $\langle E_p \rangle$, and $\langle E_k \rangle$, are given by (see e.g Carcione, 2001)

$$\langle \boldsymbol{P} \rangle = -\frac{1}{2}\ \langle \mathsf{Re}(\boldsymbol{\sigma}) \cdot \mathsf{Re}(\dot{\boldsymbol{u}}) \rangle\,, \langle E_p \rangle = \frac{1}{2}\ \langle \mathsf{Re}(\boldsymbol{\sigma}) \cdot \mathsf{Re}(\boldsymbol{\epsilon}) \rangle\,, \text{and}\, \langle E_k \rangle = \frac{1}{2}\,\rho\ \langle \mathsf{Re}(\dot{\boldsymbol{u}}) \cdot \mathsf{Re}(\dot{\boldsymbol{u}}) \rangle\,. \tag{4.19}$$

4.1.2 Computation of Dispersion Curve

4.1.2.1 Bone Models

Three homogeneous TI layered bone models (Figure 4.2) were considered to validate the simulated results and study the through-thickness wave structures. They are a free bone plate (Model 1), a bone plate with overlying soft tissue (Model 2), and a bone plate surrounded by soft tissue and marrow (Model 3).

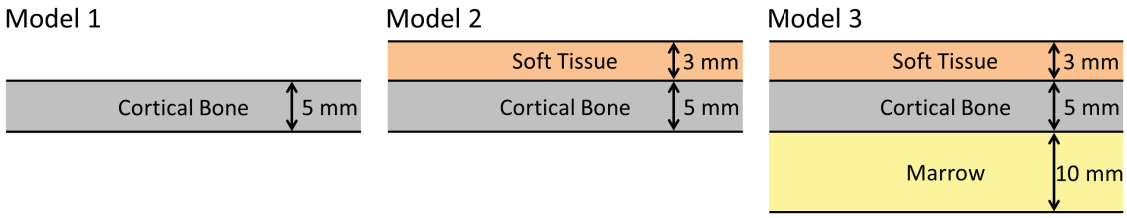

Figure 4.2: 2D layered bone models used in dispersion calculation.

Table 4.1: Material parameters of bone models used in the dispersion curve calculation

Experiment	Material	h (mm)	ρ (kg/m^3)	V_{PL}/V_{PT} (m/s)	V_S (m/s)	Compressional viscosity (dB/MHz/cm)	Shear viscosity (dB/MHz/cm)
	Soft tissue	3	1043	1561	0	0.54	0
Bone Models	Cortical bone	5	1930	4000/2000	1652	3.2/4.2	4
(1, 2, or 3)	Marrow	10	930	1480	0	0.8	0
Fluid-Solid	Water	0.5	1000	1480	0	0	0
Bilayer	Aluminium	20	2700	5950	3120	0	0
	Soft tissue mimic	2	1000	1600	0	0.54	0
Ex-vivo	Cortical bone	6	1930	4250/3170	2041	3.2/4.2	4
	Marrow mimic	2	1000	1500	0	0.8	0

The material properties relevant to the three bone models are summarized in Table 4.1, where h, ρ, V_{PL}, V_{PT}, and V_S are the thickness, the mass density, the longitudinal compressional wave speed, the transverse compressional wave speed, and the shear wave speed respectively. The values of these properties and the viscosities are chosen from the published results in the literature (Naili *et al.*, 2010; Le *et al.*, 2010; Culjat *et al.*, 2010). Also shown in Table 4.1 are a fluid-solid bilayer model (Yapura and Kinra, 1995) and a bone model for an *ex-vivo* experiment.

4.1.2.2 Verification of Computational Accuracy

In order to validate the accuracy of the proposed SAFE method and its implementation to characterize the dispersion of guided waves, I compare the dispersion curves calculated by the developed SAFE algorithm for two cases: (1) a bone plate in vacuum with the commercial software DISPERSE (Pavlakovic and Lowe, 2001) and (2) a fluid-solid bilayer with published data by Yapura and Kinra, 1995.

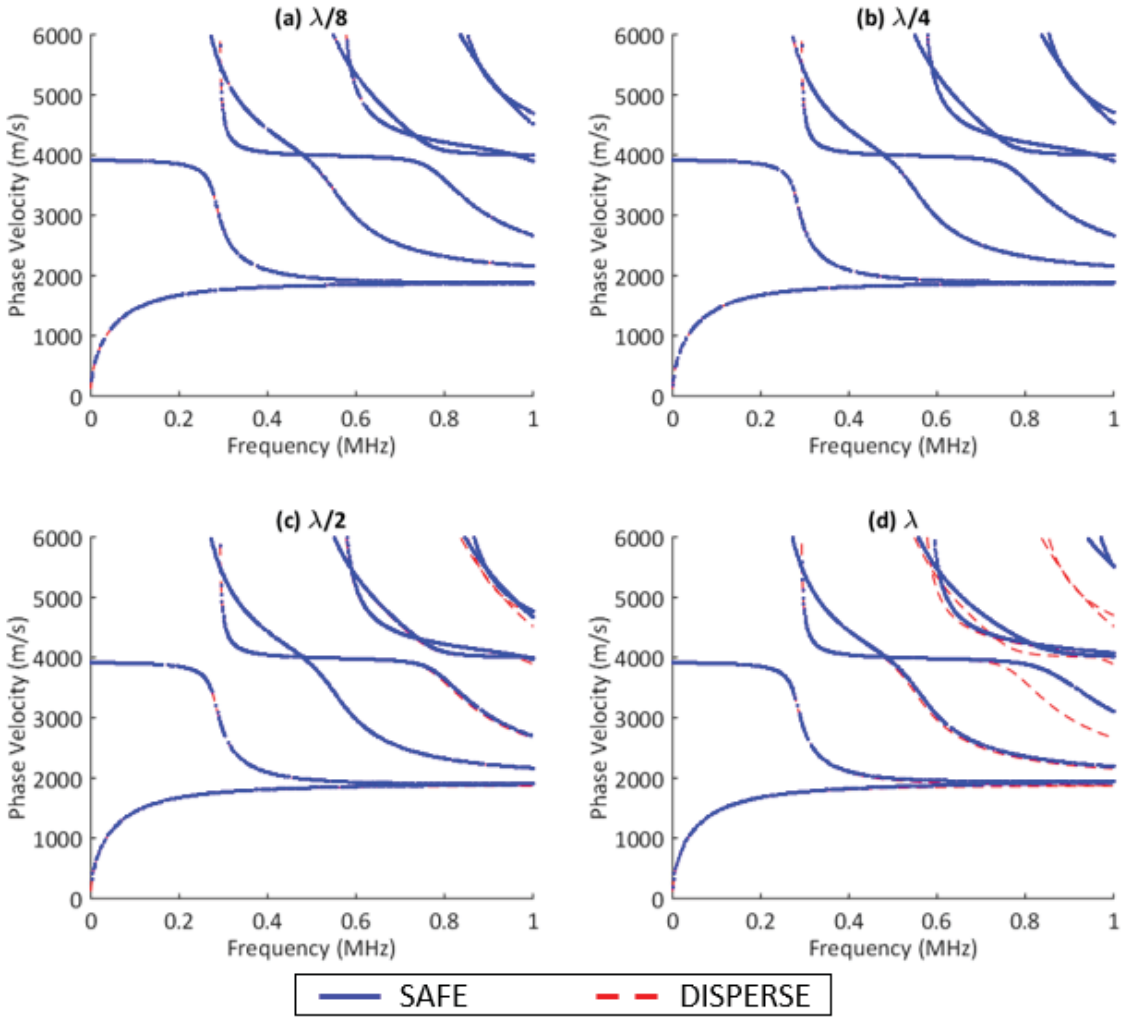

Figure 4.3: Comparison between the phase velocity dispersion of Lamb waves computed by the SAFE method (blue) and DISPERSE (red) for four element sizes using the 5-mm thick bone plate (Model 1 in Figure 2). The element sizes are (a) $\lambda/8$, (b) $\lambda/4$, (c) $\lambda/2$, and (d) λ respectively, where λ is the shear wavelength of the bone plate.

The first structure examined is a 5-mm thick viscoelastic TI bone plate in vacuum (Model 1 in Figure 4.2). The physical parameters of the plate can be found in Table 4.1.

In this case, Lamb waves are generated up to 1 MHz (Figure 4.3) using four element sizes varying from $\lambda/8$ to a full shear wavelength, λ, propagating in the bone plate to study the effect of the element size upon the computational accuracy of the dispersion curves. Superimposed are the solutions computed by DISPERSE. The results are in good agreement for element size up to $\lambda/4$ (Figure 4.3b). Discrepancy between results is noticeable at element size of $\lambda/2$ for higher order guided modes, especially at high frequency region (Figure 4.3c). When the element size increases to one wavelength (Figure 4.3d), agreement between results deteriorates further and the mismatch propagates down to lower order guided modes, noticeably for frequencies over 0.5 MHz.

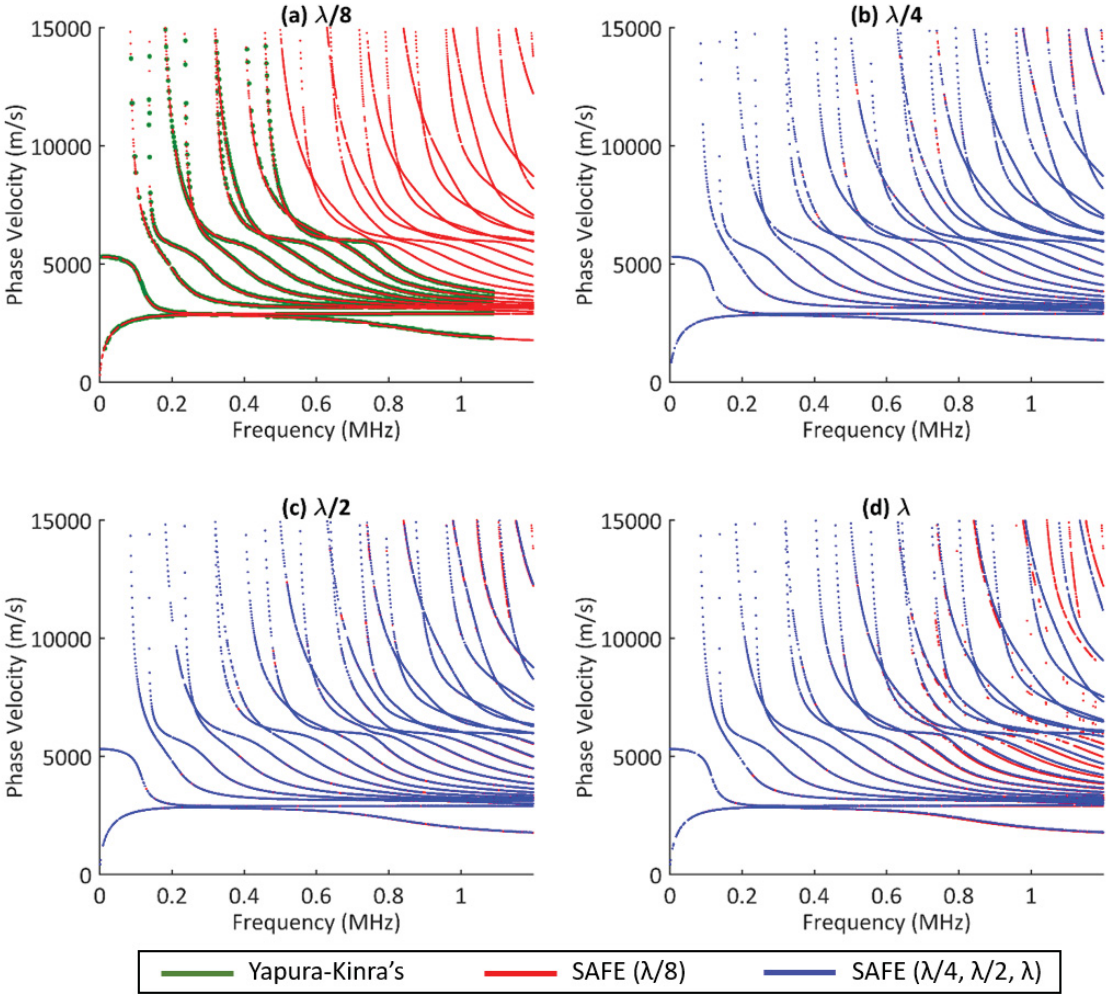

Figure 4.4: (a) Comparison between the SAFE's phase velocity dispersion curves (red) and Yapura-Kinra's results (green) for a water-aluminum bilayer using element size of $\lambda/8$ where λ is a wavelength of acoustic wave in water. Subsequently, the SAFE's phase velocity dispersion curves (red) are used as reference to compare other SAFE's estimation (blue) using bigger element sizes: (b) $\lambda/4$, (c) $\lambda/2$, and (d) λ.

The second structure to be investigated is an elastic water-aluminum bilayer (Table 4.1). This example is chosen because it was analytically studied by Yapura and Kinra, 1995. Four SAFE solutions are presented up to 1.2 MHz for four different element sizes, which, similar to Figure 4.3, vary from $\lambda/8$ to a full shortest wavelength of the system. In this case, the wavelength associated with ultrasonic propagation in water is used. Yapura and Kinra, 1995 only calculated the first 10 modes, which were used for comparison. With the element size equal to $\lambda/8$, the SAFE method has faithfully reproduced the dispersion curves of Yapura and Kinra (Figure 4.4a), confirming the accuracy and reliability of the simulation method. Hereafter the SAFE dispersion curves calculated with $\lambda/8$ element size were used as the reference to compare results with larger element size. When the element size increases to $\lambda/4$ (Figure 4.4b), the SAFE algorithm misses some roots in the region: 0.7 MHz - 1.25 MHz / 10000 m/s - 15000 m/s. This becomes worse when the element size expands to $\lambda/2$ (Figure 4.4c) and λ (Figure 4.4d), resulting in discontinuous or interrupted dispersion branches. As well, the discrepancy between the reference and the calculated results is much pronounced beyond 1 MHz and over 10000 m/s.

4.1.2.3 Elastic and Viscoelastic Bilayer and Trilayer Bone Models

I first consider a soft tissue-bone bilayer (Model 2 of Figure 4.2). The material attenuation coefficients are assumed to be zero for the elastic case. Figures 4.5 shows the simulated phase and energy velocity spectra for the elastic and viscoelastic bone plates with overlying soft tissue. The attenuation values up to 0.7 dB/cm are superimposed. Four points at 0.95 MHz from the four guided modes in the frequency-phase velocity (f-c) plane are chosen to study their wave structures. The corresponding particle displacements or wave structures are shown in Figure 4.6. The displacement fields of the same kind are normalized by the global maximum of the displacement magnitudes.

A soft tissue-bone-marrow trilayer (Model 3 of Figure 4.2), which is consisted of a bone plate with overlying soft tissue and underlying marrow layers, is considered next. The dispersion results are shown in Figure 4.7. Similarly, four displacement profiles across the thickness are plotted for the four points at 0.95 MHz from the four guided modes in the f-c plane (Figure 4.8).

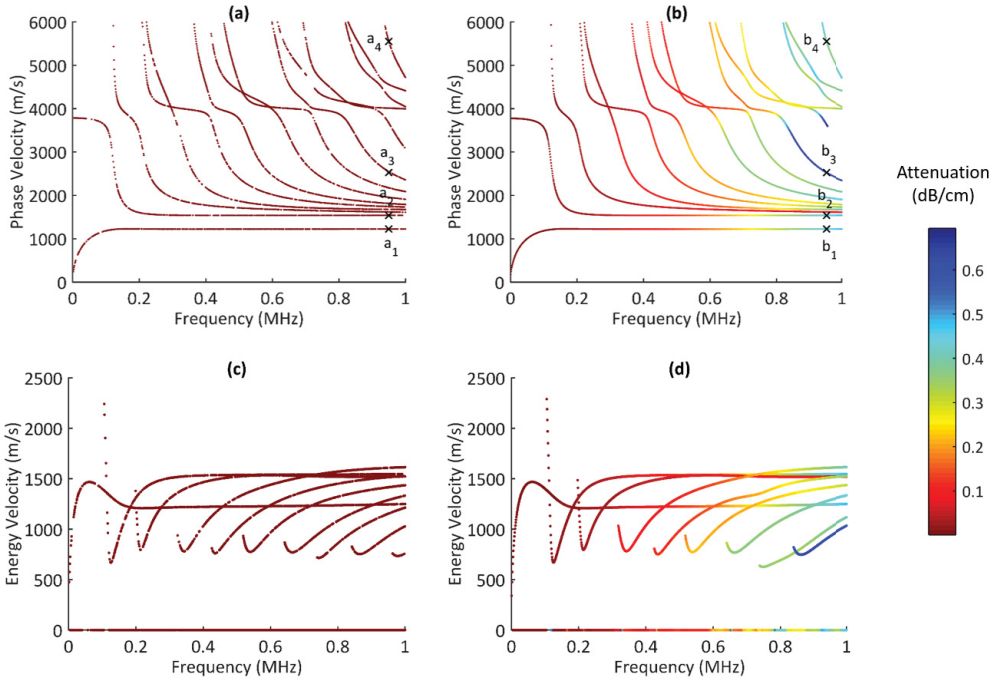

Figure 4.5: Velocity spectra for the soft tissue-bone bilayer (Model 2 of Figure 4.2): Phase velocity dispersion curves for (a) elastic case and (b) viscoelastic case; Energy velocity dispersion curves for (c) elastic case and (d) viscoelastic case; Superimposed are the corresponding attenuation values. Four points marked in (a) and (b) at 0.95 MHz are used to illustrate the wave structures in Figure 4.6. (a_1, b_1), (a_2, b_2), (a_3, b_3), and (a_4, b_4) are from Mode 1, Mode 2, Mode 9, and Mode 14 respectively.

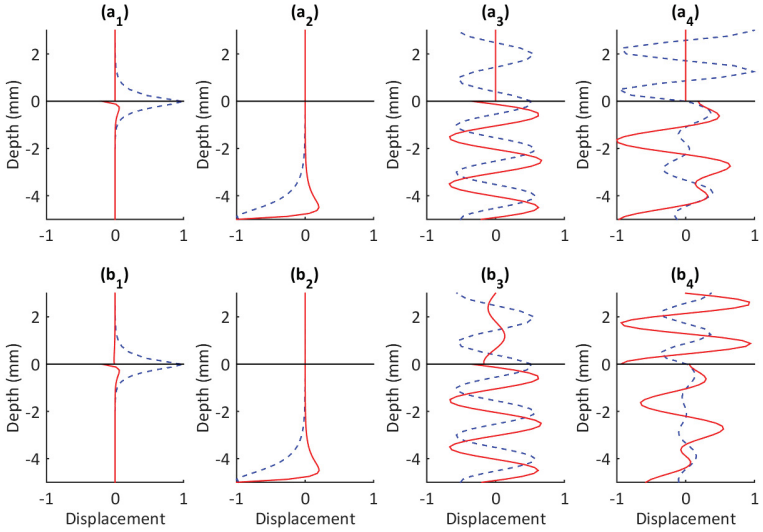

Figure 4.6: Displacement fields (vertical: dashed blue, horizontal: solid red) for the soft tissue-cortical bone bilayer (Model 2 of Figure 4.2): (a_1)-(a_4) are for the elastic case and (b_1)-(b_4) for the viscoelastic case for the four points at 0.95 MHz as marked in Figures 4.5a and 4.5b. The vertical and horizontal displacement fields are normalized by their respective global maximum of the displacement magnitudes.

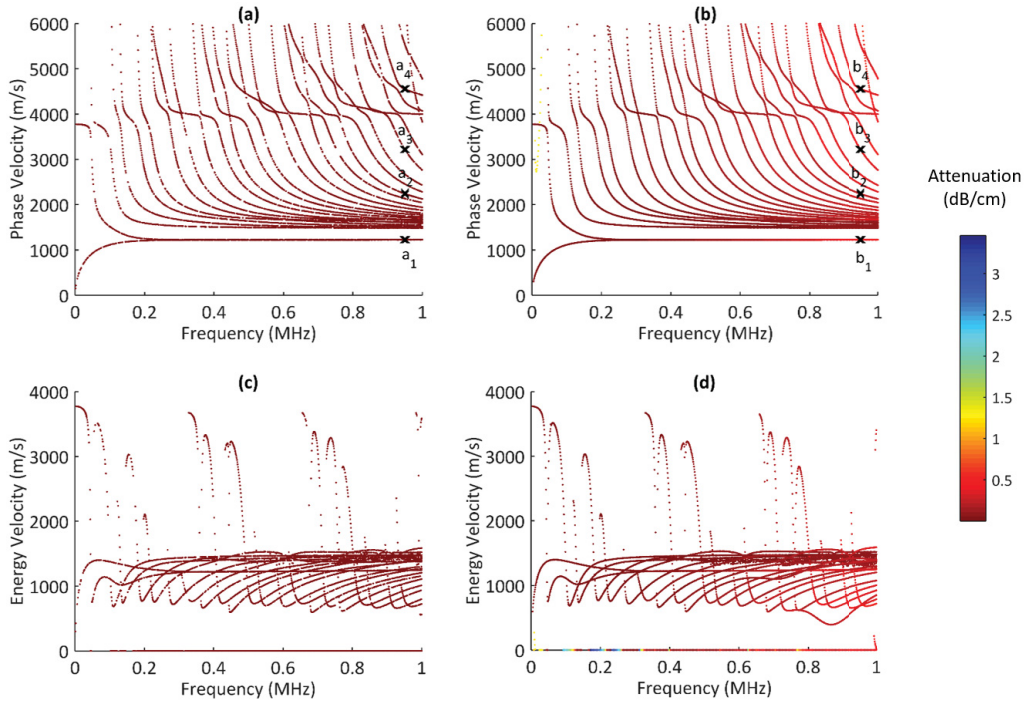

Figure 4.7: Velocity spectra for the soft tissue-bone-marrow trilayer (Model 3 of Figure 4.2): Phase velocity dispersion curves for (a) elastic and (b) viscoelastic case; Energy velocity dispersion curves for (c) elastic case and (d) viscoelastic case. Superimposed are the corresponding attenuation values. Four points marked in (a) and (b) at 0.95 MHz are used to illustrate the wave structures in Figure 4.8. (a_1, b_1), (a_2, b_2), (a_3, b_3), and (a_4, b_4) are from Mode 1, Mode 18, Mode 21, and Mode 25 respectively.

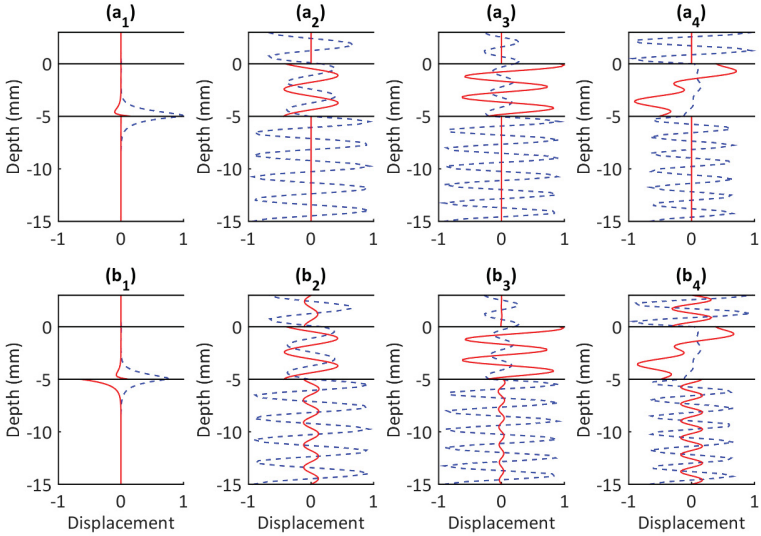

Figure 4.8: Displacement fields (vertical: dashed blue, horizontal: solid red) for the soft tissue-bone-marrow trilayer (Model 3 of Figure 4.2): (a_1)-(a_4) are for the elastic case and (b_1)-(b_4) for the viscoelastic case for the four points at 0.95 MHz as marked in Figures 4.7a and 4.7b. The vertical and horizontal displacement fields are normalized by their respective global maximum of the displacement magnitudes.

4.1.2.4 Interpretation of Ex-vivo Data

The SAFE algorithm is applied to interpret the dispersion of a guided wave dataset acquired on a bovine femur plate with a 2-mm thick Blue Phantom^{TM} layer (CAE Healthcare, Sarasota FL) on the top and water at the bottom (Figure 4.9a). The dimensions of the bovine bone plate are 180 mm $\times$ 55 mm with a mean thickness of 6 mm. The tissue-mimicking material and water are used to mimic human soft tissue and marrow. The ultrasonic axial-transmission measurement is performed using two 1-MHz angle beam compressional wave transducers (Panametrics C548, Olympus NDT, Waltham, MA, USA) attached to two angle wedges (Panametrics ABWM-7T-30). Two clips, designed by CAD modeling and produced by 3D printer, hold the the transducer-wedge systems in place while the other ends are attached to the two steel bars, which provide constant pressure to the contact surface during the experiment. One probe acts as a stationary transmitter and the other as a receiver. The transmitter is pulsed by a Panametrics 5800 P/R (Panametrics, Waltham, MA, USA). The signals detected by the receiver are digitized by and displayed on a 200-MHz digital storage oscilloscope (LeCroy 422 WaveSurfer, Chestnut Ridge, NY). Ultrasound gel is applied on all contact surfaces to ensure good coupling. The experiment is performed at room temperature (21-22^{o}C). Further details of the experimental setup are provided by Tran *et al.*, 2013. A total of 64 ultrasonic records are collected with the closest offset (transmitter-receiver distance) of 30 mm and the receiver spacing of 1 mm. The ultrasound properties of the trilayered model are provided in Table 4.1. The longitudinal compressional velocity is obtained from the time-distance (t-x) data while the longitudinal shear velocity is measured axially using a pair of 1 MHz shear wave contact transducers (Panametrics V153, Olympus NDT, Waltham, MA, USA). The transverse compressional velocity was measured by a pair of 1 MHz compressional wave contact transducers (Panametrics V103, Olympus NDT, Waltham, MA, USA) using transmission-through technique. The measured values are within the range reported in the literature (Pithioux *et al.*, 2002; Le *et al.*, 2010). Small attenuation values were used to account for the damping of soft tissue and marrow (Naili *et al.*, 2010).

The acquired time-distance (t-x) data set is transformed to the frequency-phase velocity (f-c) domain using the high-resolution linear Radon transform (Tran *et al.*, 2014*a*; Tran *et al.*, 2014*b*) and linear interpolation. Intensity peaks of the guided modes in the f-c plane are searched for each frequency and the maximum intensity of the peaks is determined. Those peaks with the intensity larger than 50% of the maximum are included. Figure 4.9b

shows the SAFE-based dispersion curves with the superposition of the experimental loci. The first eleven guided modes are identified to have close agreement with the experimental data.

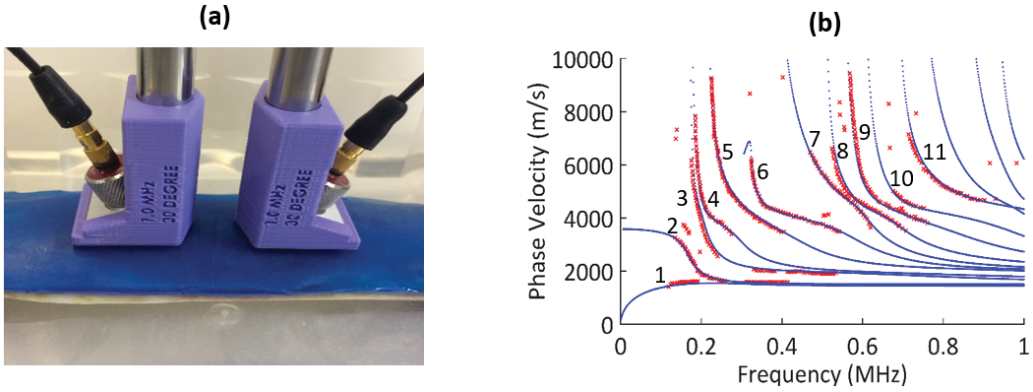

Figure 4.9: (a) The setup of the *ex-vivo* axial-transmission experiment. (b) The theoretical f-c dispersion curves are calculated for the trilayered model consisting of soft tissue mimic, bovine bone plate, and marrow (blue curves). Superimposed are the maximum intensity loci from the experimental data (red dots).

4.1.3 Discussions

Velocity and attenuation are two important parameters characterizing dispersion of guided waves propagating within multilayered structures. A solid knowledge of the aforementioned frequency-dependent characteristics is essential in our understanding of the ultrasonic guided wave propagation in long bones. In order to solve the inversion problem, i.e., to extract bone parameters from the ultrasonic guided wave data, a numerical simulation tool must be developed to predict the dispersion curves given a bone model. This will subsequently provide guidance to optimize data acquisition and model-based inversion of guided wave energy for cortical bone parameters. The objective of this work is to develop a forward modeling algorithm using SAFE scheme to estimate dispersion energy of ultrasound traveling within an elastic/viscoelastic trilayered bone model. The bone model is novel with soft tissue and marrow layers on both sides. To the best of my knowledge, this is the first attempt to simulate the dispersion and attenuation curves of ultrasonic guided modes traveling along a TI bone plate of a trilayered system.

The SAFE solutions have been validated by DISPERSE for a bone plate model and by Yapura-Kinra's result for a bilayered model. The accuracy of SAFE approximation depends on the element discretization along the cross-section of the waveguides. The mesh should be sufficiently fine to accurately capture the waveguide structures at the maximum frequency of interest. Rose suggests to use at least eight elements per wavelength and four-to-five

nodes per element to obtain accurate solutions (Rose, 2014). In the simulation, I use 1/8 of the wavelength as the element size with three nodes for each element. The simulated results are in very good agreement with the reference data from DISPERSE and Yapura and Kinra, 1995. Elements with four and five nodes are also used but the same dispersion curves and wave structures are obtained. The comparison also agrees when the element size is doubled to $\lambda/4$. Discrepancy between the simulated data and the reference always appears first for the high frequency region and higher order guided modes and propagate downward (lower frequencies and smaller phase velocities) as the element size gets bigger. It took approximately 20 seconds to calculate a dispersion profile for a trilayered model (Figure 4.9b) with a Intel Core i7 4.00-GHz CPU and 64-Gb RAM Windows 10 64-bit computer.

The presence of the soft tissue layer on top of the cortex increases the number of the observed guided modes (Figure 4.3a versus Figure 4.5a). The phenomenon was observed in the previous *ex-vivo* study by Tran *et al.*, 2013. The addition of underlying marrow also increases the number of guided modes (Figure 4.5a versus Figure 4.7a). While the possible dispersion curves, which account for the kinematic properties of the guided modes, are predicted, not all guided modes are excited in the bone. Only some of them in particular frequency neighborhoods will propagate (Rose, 2014; Tran *et al.*, 2015). The non-propagating waves correspond to the so called evanescent waves, whose energies are not propagating for long distances. From the mathematical point of view, the wavenumbers of these waves are complex or purely imaginary.

The inclusion of absorption in the model does not seem to modify significantly the phase/energy velocity and displacement profiles of the guided modes within the f-c region of interest (Figures 4.5b, 4.5d, 4.7b, and 4.7d). The damping has the least effect upon the low frequency components, say under 0.5 MHz. Then attenuation increases with frequency up to 0.7 dB/cm beyond 0.8 MHz especially for high order modes, which vanish in the viscoelastic case.

The viscosity of the bone plate has little impact on the wave structures or displacement profiles of the guided modes at low frequencies, where the wave structures between the elastic and viscoelastic cases are similar. For the bilayer, I compare wave structures for the four guided modes at 0.95 MHz (Figure 4.6). Basically there is no particle motion along the horizontal (x_1) direction in the soft tissue except for mode 9 and mode 14, which oscillate in the soft tissue layer for the viscoelastic cases with mode 14 having a much larger displacement magnitude. The horizontal displacement is discontinuous across the

soft tissue-bone boundary as expected. Within the bone layer, I observe the following for the horizontal particle motion. Mode 1 has a very mild displacement close to the interface. Mode 2 starts at around -2 mm with a gentle increase in positive displacement amplitude and then drops sharply to a large negative displacement around 5 mm below the interface. Mode 9 oscillates periodically with large magnitude. Mode 14 oscillates irregularly with large troughs. The vertical displacements for the elastic and viscoelastic cases are continuous across the interface and look similar. Mode 1 has a gentle positive displacement with a maximum close to the interface within the soft tissue and bone layers. Mode 2 has no motion in the soft tissue and a negative displacement component in the bone layer. Mode 9 oscillates periodically in both layers with a uniform amplitude. Mode 14 also oscillates regularly in soft tissue but irregularly in the bone layer. For the trilayer (Figure 4.8), a similar observation can be drawn. The horizontal displacements are discontinuous across the interfaces. All modes lack the horizontal motion in both the soft tissue and marrow layers for the elastic case while the horizontal motion, except for modes 1 and 21 in soft tissue, are non-vanishing for the viscoelastic case and oscillate for higher order modes. The horizontal motion within the elastic and viscoelastic bone plate has a small displacement for mode 1 and oscillates with increasing strength for higher order modes. The vertical wave structure, which is continuous across the interfaces, shows more complexity. Mode 1 has a gentle positive vertical displacement with a maximum close to the bone-marrow interface within the bone and marrow layers. The vertical displacement field oscillates in all layers for higher order modes.

It has been found that DISPERSE has challenges to compute the dispersion curves for a bilayered bone model with overlying soft tissue. The problem becomes intractable when the third layer of underlying marrow is involved. Both the overlying and underlying tissues have much lower velocities than the bone layer ($\sim$ 1500 m/s versus $\sim$ 4000 m/s). The outcome is unpredictable. The program either runs, does not run, or terminates itself. It is difficult to place confidence on the computed results.

The developed simulation tool may be directly used for a functionally-graded bone plate, where bone properties change along the $\boldsymbol{x}_2$ direction. A limitation of the SAFE method is that it only considers bone plates with constant thickness and elastic parameters along $\boldsymbol{x}_1$. This usually does not pose a big challenge as the bone section between the emitter and receiver is only a few centimeter long and the thickness and velocities varies mildly.

Though mimicking long bones using a layered model has been justified (Le *et al.*, 2010), development of a simulation algorithm for cylindrical bone waveguides will be a good re-

search direction in the future. The cylindrical model has much closer similarity to the long bone geometry. Moreover, the merit of simulating dispersion curves for a cylindrical model allows us to compute selectively any individual longitudinal guided modes.

My doctoral research focuses on a SAFE-based approach for calculating the dispersion characteristics of ultrasonic guided waves propagating in viscoelastic TI bone waveguide coupled with soft tissue and marrow modeled as viscous fluids. The validation with published data and application on a plate-like bone models with surrounding soft tissue and marrow illustrate the accuracy and potential of the developed simulation tool to predict the dispersion of ultrasonic guided modes propagating in long bones *in vivo* with the presence of soft tissue and marrow layers. The validated forward computational algorithm plays a keystone to solve the model-based inverse problem to recover cortical bone properties, which is very meaningful for the non-invasive ultrasonic diagnosis of bone health.

4.2 Sensitivity Analysis

The fundamental ultrasonic guided modes are consistently observed in long bones *ex vivo* and *in vivo*. However, the responses of ultrasonic guided waves to the changes of cortical thickness, cortical elastic parameters, and thickness of the overlying soft tissues are not comprehensively understood. This section systematically presents a sensitivity analysis of leaky Lamb modes to the geometry and material characteristics of layered bone model by means of semi-analytical finite-element modeling. The stratified bone model is consisted of a transversely isotropic cortex with an overlying soft tissue and underlying marrow. This sensitivity study is important as it offers guidance to the parameter inversion process about the optimal selection of guided modes and regions of sensitivity for better inversion results.

4.2.1 Introduction

Currently, there is a lack of comprehensive study of the dependence of UGW upon the geometrical and mechanical properties of bone waveguide. Moilanen *et al.*, 2004 measured the phase speed variation of ultrasonic waves in two thick and thin PVC bone-mimicking phantoms. Their work was limited to the cortical thickness sensitivity only. Most recently, numerical simulation (Thakare *et al.*, 2017) has been used to provide more insight into the effect of dimensional degradation of cortical bone on cylindrical guided wave velocity. The studies considered a very small range of cortex thickness (1-3 mm) and the quantitative analysis was limited to two guided modes L(0,3) and F(1,6). It is expected that a more vigorous sensitivity investigation of the bone's geometrical and mechanical properties upon

the modal characteristics of UGW will enhance our fundamental understanding of ultrasound interaction of bone tissue under the impact of the surrounding soft media. This will subsequently improve the efficacy of guided wave technology for cortical bone quality assessment.

This section presents a sensitivity analysis of the UGW to dimensional and mechanical property changes of layered bone models by means of numerical simulation. While cylindrical models more closely resemble the human long bone geometry and provide a more accurate simulated ultrasonic response, our lab's work (Le *et al.*, 2010) and others (Chen *et al.*, 2012; Minonzio *et al.*, 2014) have also demonstrated that the stratified bone model quite adequately interpret the long bone data at hand, especially in case when the radius of the bone sample is large. In this sensitivity study, dispersion curves are simulated for plate-like cortical bone structures using semi-analytical finite element (SAFE) method. I then identify the impact of geometry and material parameters on the characteristic phase velocities of the leaky Lamb waves, i.e., the sensitivity of the phase velocities of the leaky Lamb modes to the variations of bone model parameters. The investigation provides opportunity to study the responses of the ultrasonic guided modes (UGM) to bone parameters, to identify the sensitive regimes in the frequency-phase velocity domain, and to quantify the amount of sensitivity of each mode.

4.2.2 Stratified Transversely-Isotropic Bone Models

I consider a homogeneous transversely-isotropic layered bone model (Figure 4.10), consisting of a cortical bone plate coupled with overlying soft tissue and underlying bone marrow. More details about the model parameters will be discussed later in Section 4.2.3.

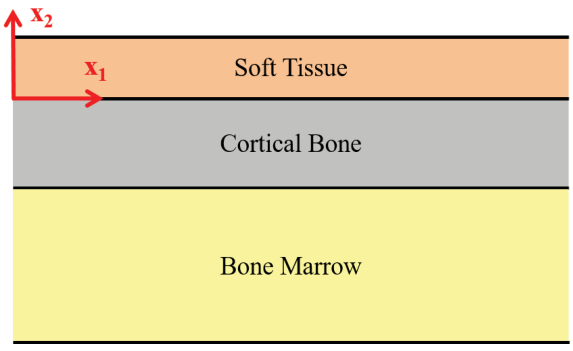

Figure 4.10: A cross-sectional geometry of a trilayered bone model.

4.2.3 Numerical Calculation of Phase-Velocity Dispersion Curves

As discussed in Section 4.1, a simulation framework to compute numerically the ultrasonic dispersion in cortical bone with coupled soft tissue and marrow (Figure 4.10) has been developed using a SAFE method. Recently, the SAFE method is more widely used due to its ability to handle arbitrary cross-sectional waveguides, being able to produce accurate and computationally efficient solutions, and being less prone to missing roots when solving the eigen-equations (Rose, 2014; Nguyen *et al.*, 2017). Here, I would like to briefly reintroduce some key points of the SAFE approach. The mathematical problem is formulated in the frequency-wavenumber (f-k) domain, which handles naturally the implementation of frequency-dependent absorption and permits selection of a k-range to study wavefields traveling at different phase velocities. The SAFE method discretizes the x_2-axis while the guided wave propagation along the x_1-direction is described analytically.

A 1D finite element assembly process along the thickness direction (x_2) gives rise to the characteristic dispersion equation of an infinite viscoelastic plate-like bone structure coupled with fluids

$$\left[\mathbf{K}_1 + k_1^2\mathbf{K}_2 + \mathrm{i}k_1\mathbf{K}_3\right]\ \mathbf{V} = \mathbf{0}, \tag{4.20}$$

where k_1 is the axial wavenumber. $\mathbf{V} = (\mathbf{P}_2, \mathbf{U}, \mathbf{P}_1)^T$ with $\mathbf{P}_\alpha$ ($\alpha = 1, 2$) and $\mathbf{U}$ being the global pressure and displacement fields or global wave structures. The frequency-dependent $\mathbf{K}$-matrices include the masses and the rigidities of cortical bone, soft tissue, and marrow, and the coupled terms between them. The mathematical expressions of these matrices have already been described in Section 4.1. Equation 4.20 can be rearranged into a system of linear eigen-value equations:

$$\left(\begin{bmatrix}\mathbf{0} & \mathbf{K}_1\\ \mathbf{K}_1 & \mathrm{i}\mathbf{K}_3\end{bmatrix} - k_1\begin{bmatrix}\mathbf{K}_1 & \mathbf{0}\\ \mathbf{0} & -\mathbf{K}_2\end{bmatrix}\right)\begin{pmatrix}\mathbf{V}\\ k_1\mathbf{V}\end{pmatrix} = \mathbf{0}. \tag{4.21}$$

Given a frequency value, the eigen-solutions to the characteristic Equations 4.21 are the wavenumbers for different guided modes. The complete set of dispersion curves can be obtained by repeatedly solving the eigen-value equation over a desired frequency range. The frequency-dependent phase velocity c_p is given by

$$c_\mathrm{p} = \frac{\omega}{\mathsf{Re}(k_1)} \tag{4.22}$$

where ω is the angular frequency.

4.2.4 Sensitivity Analysis of Bone Model Parameters

Six material properties were investigated: soft tissue thickness (h_{ST}), cortical bone thickness (h_{CB}), shear wave velocity (V_{S}), longitudinal compressional wave velocity (V_{PL}), transverse compressional wave velocity (V_{PT}) of the cortex, and bone density (ρ). The influence of each parameter to the dispersion characteristics was studied by varying one at a time while holding the others constant at their respective reference values. The reference, minimum, maximum, and step values relevant to the six model parameters are summarized in Table 4.2. Those values were chosen in accordance with the ones reported in the literature for human tibia (Laugier and Haiat, 2011; Le *et al.*, 2010; Capozza *et al.*, 2010; Mesquita *et al.*, 2016). The material absorption was ignored because it did not significantly affect the phase velocity dispersion of the guided modes in the frequency range of interest (Nguyen *et al.*, 2017). The acoustic wave velocity and mass density of the soft tissue and marrow layers are assumed to be approximately 1500 m/s and 1000 kg/m^3 respectively (Gurkan and Akkus, 2008; Culjat *et al.*, 2010). The bone marrow thickness was set at 7 mm, which was based on the narrowest diameter of medullary cavity at human tibial diaphysis.

Table 4.2: Material parameters of bone models used in the sensitivity analysis

Parameter	h_{ST}	h_{CB}	V_{S}	V_{PL}	V_{PT}	ρ
(unit)	(mm)	(mm)	(m/s)	(m/s)	(m/s)	(kg/m^3)
reference	1	5	2000	4000	3000	2000
minimum	1	2	1400	3000	2000	1400
maximum	5	7	2400	4000	3000	2400
step	1	1	200	200	200	200

The analysis of dispersion sensitivity of the UGM to geometry and material characteristics of the model was assessed by comparing phase velocity spectra derived from the different trilayer bone models over the low-frequency range ($<$ 1 MHz) against the reference bone model. This frequency range is typically most relevant to clinical application.

In the frequency range of interest from 0 to 1 MHz, the sensitivity analysis was performed on the first eight leaky Lamb modes. The UGM numbering system (Rose, 2014) was used to name the eight leaky Lamb modes in the bone plate. The eight modes were named mode 1, mode 2, mode 3, mode 4, mode 5, mode 6, mode 7, and mode 8 respectively from the lowest to higher order.

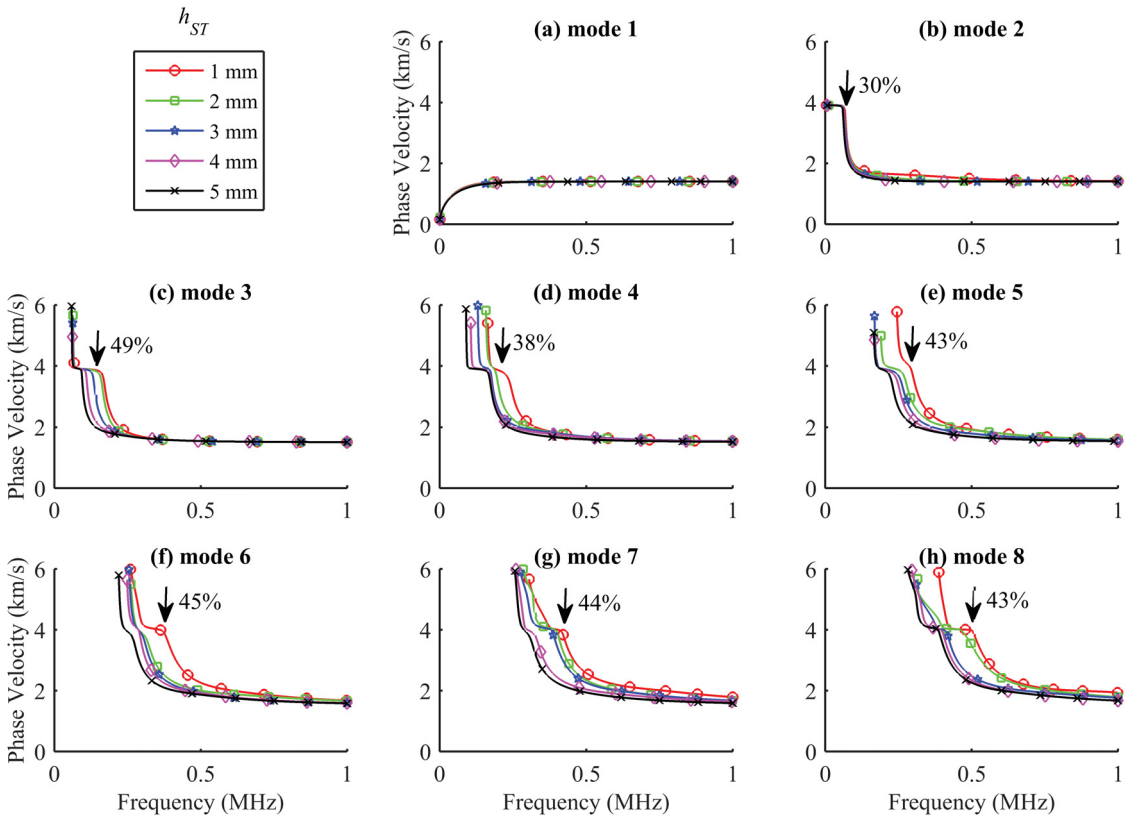

Figure 4.11: Sensitivity of leaky Lamb modes to soft tissue thickness (h_{ST}). The arrows indicate the frequencies which have the biggest change.

Soft tissue thickness was found to have insignificant influence on mode 1 (Figure 4.11a). Its presence only affects the dispersion characteristics of mode 2 at the very low frequency (0.1 - 0.45 MHz) (Figure 4.11b), mode 3 up to 0.35 MHz (Figure 4.11c), modes 4, 5, and 6 up to 0.5 MHz (Figures 4.11d, 4.11e, and 4.11f), and modes 7 and 8 up to 0.8 MHz (Figures 4.11g and 4.11h). Increasing the soft tissue thickness by 400% (1 to 5 mm) results in a reduction of phase velocity by approximately 1100 m/s (30%) in mode 2 at 0.07 MHz, 1900 m/s (49%) in mode 3 at 0.2 MHz, 1500 m/s (38%) in mode 4 at 0.2 MHz, 1600 m/s (43%) in mode 5 at 0.3 MHz, 1800 m/s (45%) in mode 6 at 0.35 MHz, 1750 m/s (44%) in mode 7 at 0.4 MHz, and 1700 m/s (43%) in mode 8 at 0.5 MHz respectively. On the average, the phase velocities of modes 2, 3, 4, 5, 6, 7, and 8 differ by at least 7.5% for 1 mm change in h_{ST}.

Cortical thickness variability has an impact on the phase velocities of the leaky Lamb waves (Figure 4.12). The effect is visible from 0.05 to 0.35 MHz for mode 1 (Figures 4.12a), around 0.1 MHz for mode 2 (Figure 4.12b), from 0.2 to 0.4 MHz for modes 3 and 4 (Figures 4.12c and 4.12d), and from 0.3 to 0.7 MHz for modes 5, 6, 7, and 8 (Figures 4.12e, 4.12f,

4.12g, and 4.12h) respectively. Increasing the bone thickness by 250% (2 to 7 mm) increases the phase velocity over 400 m/s (48%) for mode 1 at 0.1 MHz but reduces approximately by 1300 m/s (37%) for mode 2 at 0.08 MHz, 1400 m/s (38%) for mode 3 at 0.18 MHz, 1700 m/s (44%) for mode 4 at 0.27 MHz, 1500 m/s (39%) for mode 5 at 0.35 MHz, 1400 m/s (36%) for mode 6 at 0.42 MHz, 1500 m/s (39%) for mode 7 at 0.5 MHz, and 1450 m/s (38%) for mode 8 at 0.6 MHz. The phase velocities of the eight modes vary by more than 7% for each 1 mm change in h_{CB} at their respective frequency of sensitivity.

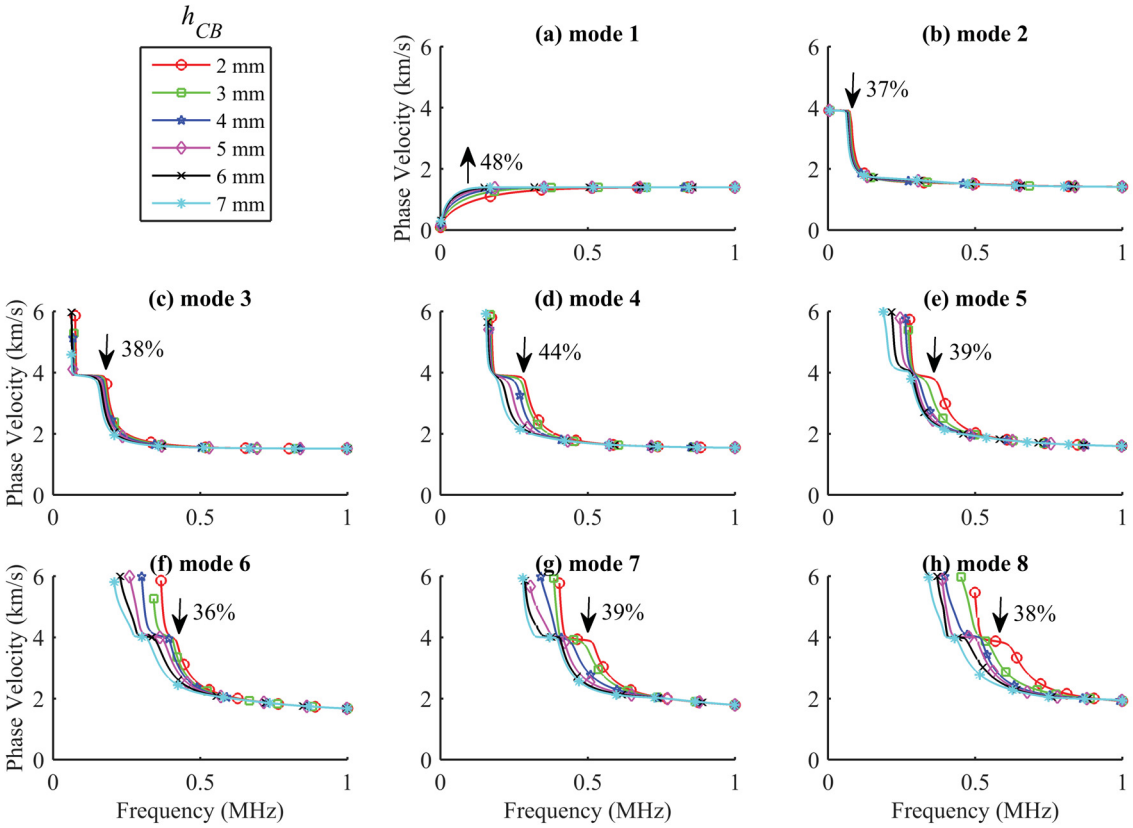

Figure 4.12: Sensitivity of leaky Lamb modes to cortical bone thickness (h_{CB}). The arrows indicate the frequencies which have the biggest change.

Variation in shear wave velocity in cortical bone modifies the dispersion characteristics of UGW slightly (Figure 4.13). When the model has a V_{S} increase of 70% (1400 to 2400 m/s), the relative increases of phase velocity are about 27% (300 m/s) at 0.15 MHz for mode 1, 19% (300 m/s) at 0.25 MHz for mode 2, 10% (200 m/s) at 0.3 MHz for mode 3, 10% (200 m/s) at 0.35 MHz for mode 4, 13% (250 m/s) at 0.45 MHz for mode 5, 17% (300 m/s) at 0.6 MHz for mode 6, 20% (400 m/s) at 0.6 MHz for mode 7, and 26% (450 m/s) at 0.9 MHz for mode 8 respectively.

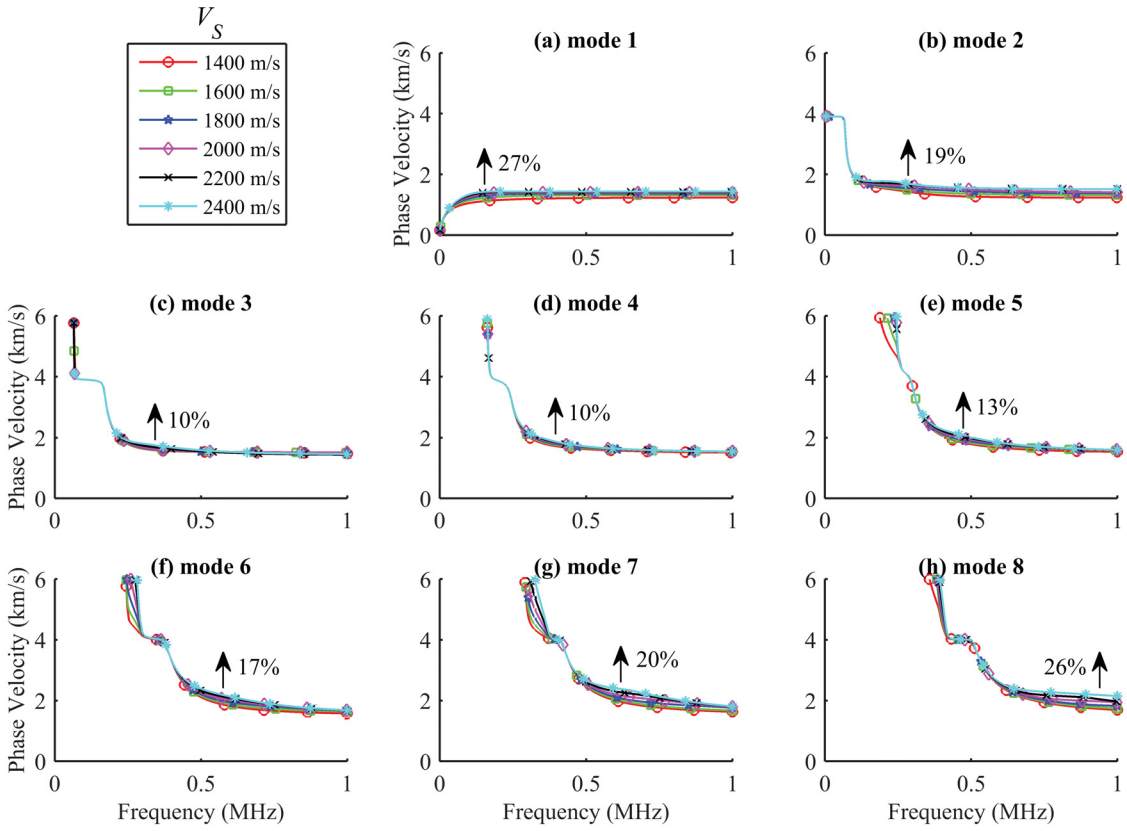

Figure 4.13: Sensitivity of leaky Lamb modes to cortical shear wave velocity (V_S). The arrows indicate the frequencies which have the biggest change.

Longitudinal and transverse compressional wave speeds have comparatively modest impact (Figures 4.14 and 4.15): change by less than 5% on modes 1 and 2 and 5-13% on the other 6 modes in a small low-frequency range for every 200 m/s increase. When the longitudinal compressional wave velocity V_{PL} increases by 33% (3000 to 4000 m/s), the phase velocity also increases by 7% (85 m/s) at 0.1 MHz for mode 1, 35% (1000 m/s) at 0.05 MHz for mode 2, 35% (1000 m/s) at 0.1 MHz for mode 3, 34% (980 m/s) at 0.2 MHz for mode 4, 28% (900 m/s) at 0.275 MHz for mode 5, 31% (1000 m/s) at 0.3 MHz for mode 6, 32% (980 m/s) at 0.4 MHz for mode 7, and 33% (1000 m/s) at 0.45 MHz for mode 8. Similar phenomena have been observed for V_{PT}: 8% (100 m/s) at 0.3 MHz for mode 1, 15% (200 m/s) at 0.4 MHz for mode 2, 66% (1500 m/s) at 0.16 MHz for mode 3, 54% (1300 m/s) at 0.225 MHz for mode 4, 42% (1100 m/s) at 0.3 MHz for mode 5, 62% (1500 m/s) at 0.37 MHz for mode 6, 36% (1000 m/s) at 0.42 MHz for mode 7, and 60% (1500 m/s) at 0.5 MHz for mode 8.

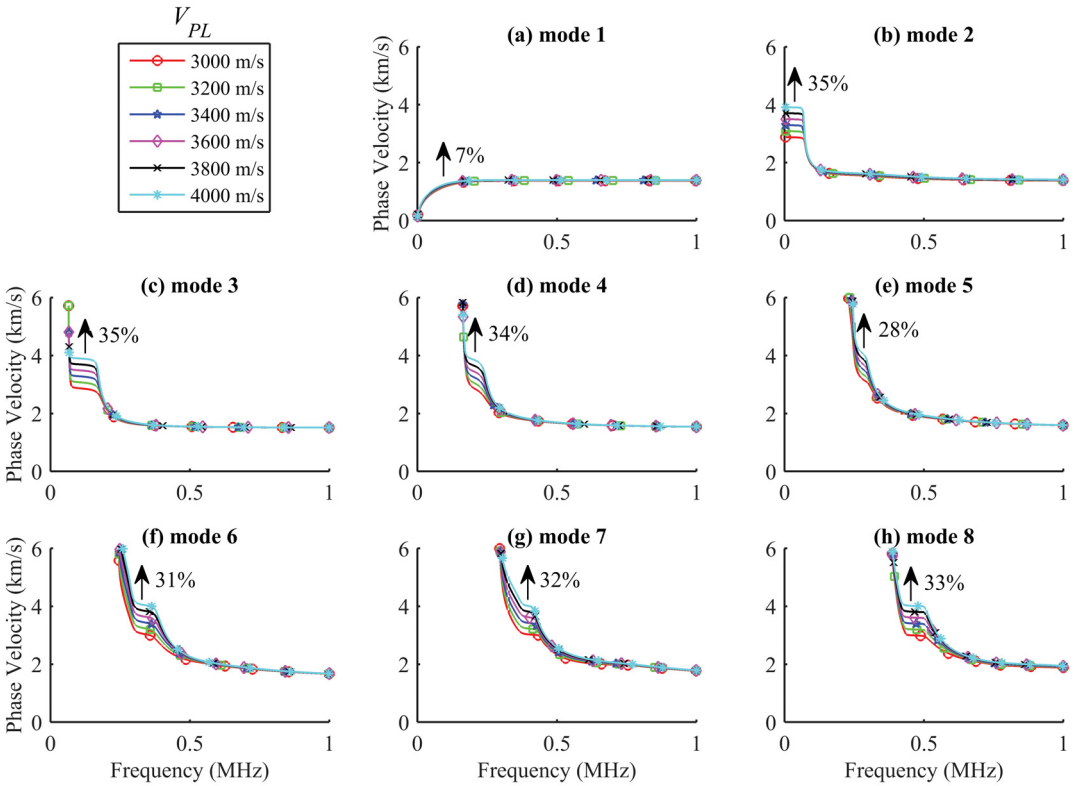

Figure 4.14: Sensitivity of leaky Lamb modes to the longitudinal compressional wave velocity (V_{PL}) of cortical bone. The arrows indicate the frequencies which have the biggest change.

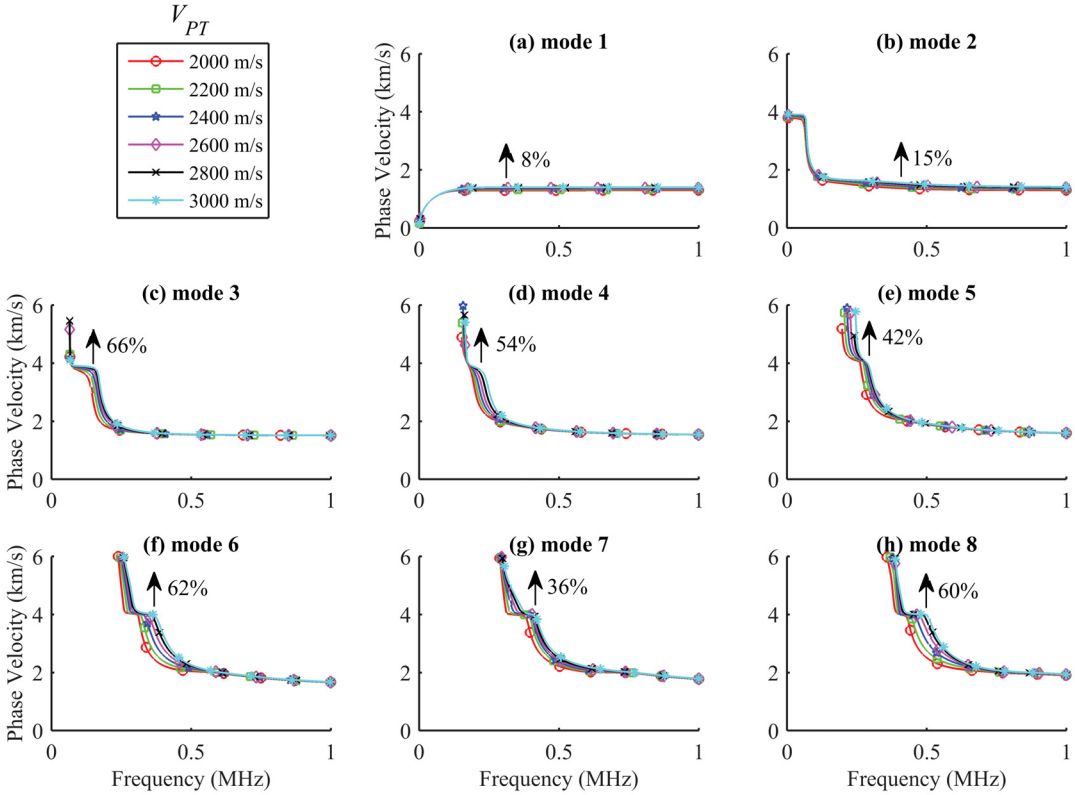

Figure 4.15: Sensitivity of leaky Lamb modes to the transverse compressional wave velocity (V_{PT}) of cortical bone. The arrows indicate the frequencies which have the biggest change.

The cortical bone density has the least effect upon the dispersion of the guided modes of interest (Figure 4.16). In comparison to the material thicknesses h_{ST} and h_{CB}, the changes in the velocities V_{S}, V_{PL}, V_{PT}, and bone density ρ do not cause as much horizontal shift of the phase velocity spectra of the UGM especially for mode 1 (Figures 4.11-4.16).

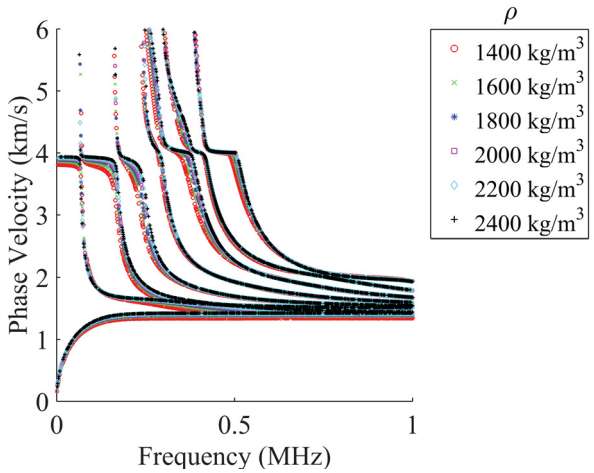

Figure 4.16: Sensitivity of the first eight leaky Lamb modes to bone mass density (ρ).

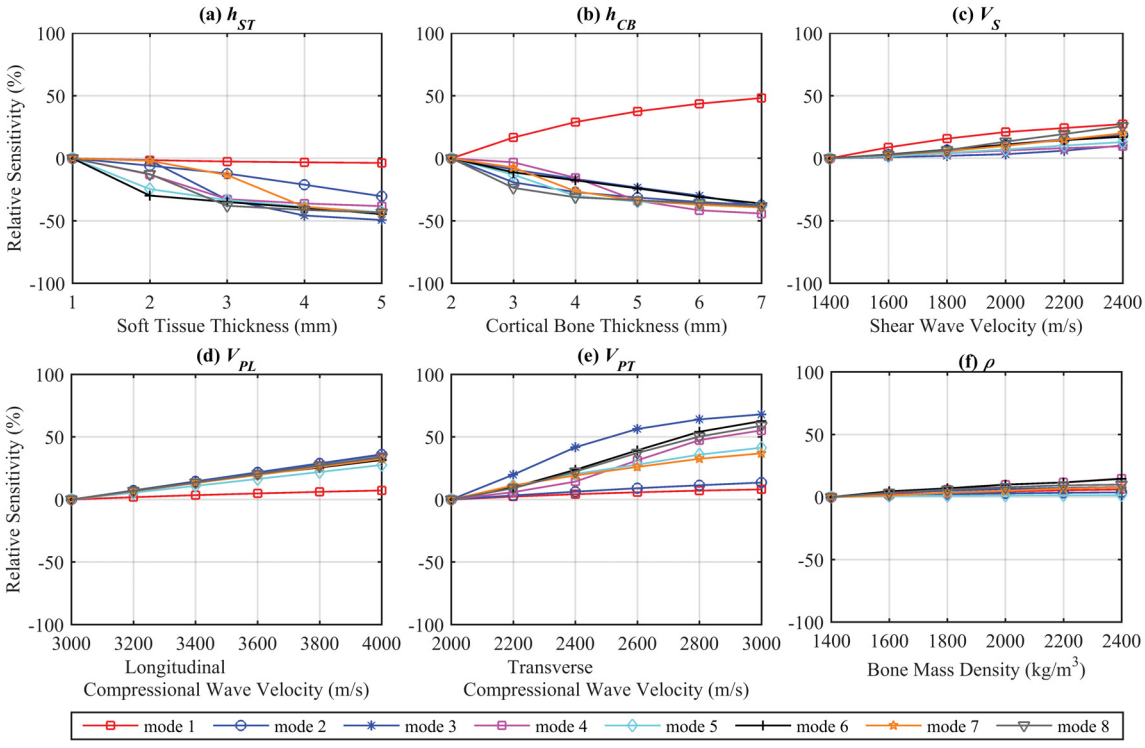

Figure 4.17: The relative sensitivity of the guided modes with respect to the reference model to changes of soft tissue thickness (h_{ST}), cortical bone thickness (h_{CB}), shear wave velocity (V_{S}), and compressional wave velocity (V_{P}) of the cortex respectively.

Figure 4.17 summarizes the phase-velocity sensitivity of the eight guided modes at their respective most sensitive frequency. The modal sensitivity to each model parameter is interpreted in terms of the percentage with respect to the reference phase speed, which is measured at the parameter's smallest value. The increase in soft tissue and cortical bone thickness slows down the phase speed of UGM except mode 1, which remains approximately constant. The impact of the overlying soft tissue on mode 1 is insignificant. Mode 1 propagates faster while other modes decrease speeds as the cortical thickness increases. The UGW phase speed tends to increase with shear, longitudinal compressional, and transverse compressional wave velocity of the cortex. The contribution of bone mass density to the dispersion sensitivity of UGM propagating in long bones is insignificant.

4.2.5 Discussions

This work is mainly focused on simulating phase-velocity dispersion of UGM propagating in bone models with overlying soft tissue, cortex, and underlying marrow and investigating the sensitivity of UGM to the geometry and material properties of interest. Identifying the region of sensitivity of each UGM is important to optimize the selective excitation, acquisition, and model-based inversion of axially-transmitted ultrasound data in long bones.

Mode 1 has been observed to have low sensitivity to h_{ST}, V_{S}, V_{PL}, V_{PT}, and ρ. The low-frequency component of mode 1 (0 - 0.35 MHz) are highly sensitive to the cortical thickness h_{CB} (Figure 4.12a) up to 50% relative sensitivity (Figure 4.17a) and, therefore, is more favorable to be utilized for inverting the bone thickness h_{CB}. The low-frequency region of the lowest-order mode is called the desired range in the field of nondestructive testing and has been used extensively in material monitoring. The fundamental mode exists in the entire frequency spectrum while the higher-order modes have certain frequency cutoffs, below which they don't exist (Firouzi *et al.*, 2016). In practice, compressional wave speed can be estimated by analyzing the first arrivals of the time signals. The cortical density ρ can be negated from the inversion procedure as its contribution to the phase-speed dispersion is relatively small in the frequency range of interest. This study is a good attempt to investigate the interaction of ultrasound waves with cortex under the impact of surrounding soft tissues and the result can be used as a basis for proper dispersion-curve inversion of thickness and elasticity of cortical bone.

The thickness of the soft tissue layer on top of the cortex modifies the dispersion curves of the observed guided modes except mode 1 (Figure 4.11). The phenomenon was observed in the previous *ex-vivo* study by Tran *et al.*, 2013 in the case of bone plate with and without

the presence of overlying soft tissue. Therefore the consideration of soft tissue layer in the inversion scheme is important and cannot be ignored.

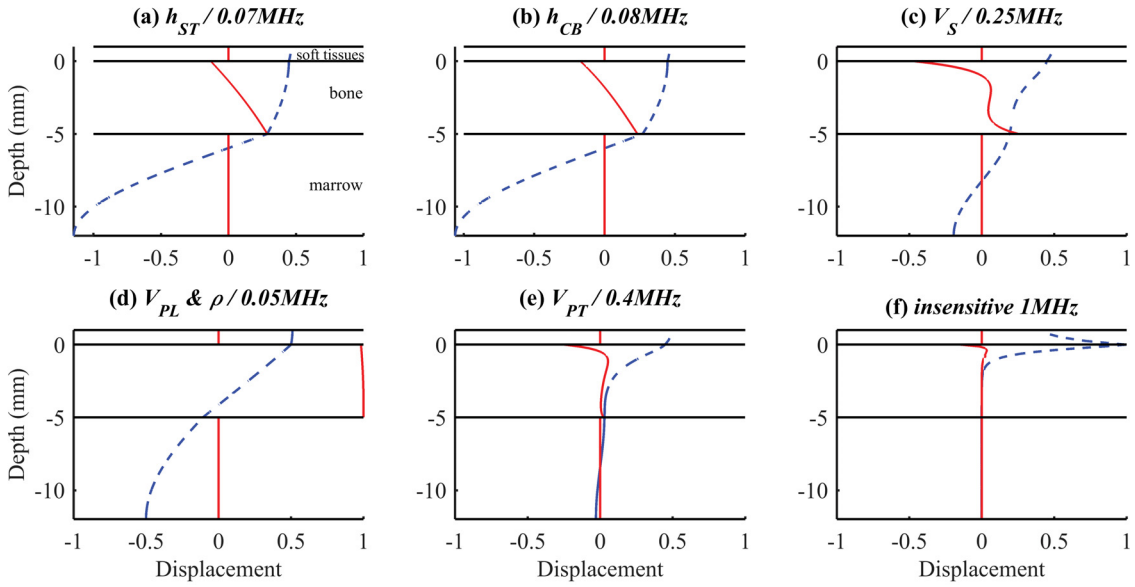

Figure 4.18: The displacement fields (horizontal: solid red, vertical: dashed blue) of the six chosen frequencies on Mode 2's phase-velocity dispersion curve using the reference model. The first five dispersion points at the most sensitive frequencies to (a) h_{ST} (0.07 MHz), (b) h_{CB} (0.08 MHz), (c) V_{S} (0.25 MHz), (d) V_{PL} and ρ (0.05 MHz), and (e) V_{PT} (0.4 MHz). (f) The wave structure of Mode 2 at 1 MHz, which is insensitive to the parameter variation.

In order to study the wave structures in the sensitive and insensitive regions of the dispersion curves, I chose six frequencies on the dispersion curve of Mode 2 using the reference model. Mode 2 was used because its dispersion curve is responsive to the change of all six model properties. The wave structure analysis was performed at six chosen frequencies: five sensitive frequencies, which respond to the parameter variations (h_{ST} at 0.07 MHz, h_{CB} at 0.08 MHz, V_{S} at 0.25 MHz, V_{PL} and ρ at 0.05 MHz, V_{PT} at 0.4 MHz) and one frequency (1 MHz), which is insensitive to the changes of the model parameters. The corresponding particle displacements are graphed in Figure 4.18. The sensitive regimes are toward the lower-frequency end of the dispersion spectra. When UGW propagate in long bones, the high-frequency components decay very quickly because of preferential absorption while the lower-frequency energies can penetrate deeper in the cortex and build up strong guided wave energy. Comparing to the displacement field of the sensitive frequencies (Figures 4.18a-4.18e), the insensitive 1-MHz (Figure 4.18f) has an insignificant horizontal particle motion in the cortex and the vertical motion is very localized to a thin portion at the top of the cortical layer. The particle displacements of the sensitive frequencies have much larger

magnitudes. On the same modal phase-velocity curve, the frequencies that lack particle motion appear to be less sensitive to the model modification.

In practice, only certain modes are excited within a finite frequency range. The UGM excitability depends on which guided mode is excited and where on its dispersion curve it is excited (Rose, 2014). The excitability function $\mathbf{E}$ of an UGM on the excitation surface is related to the acoustic particle velocity $\mathbf{v}$ by Tran *et al.*, 2015; Gao and Rose, 2010

$$\mathbf{E} = |\mathbf{v}| \tag{4.23}$$

where $\mathbf{v}$ is related to the particle displacement $\mathbf{u}$ by $\mathbf{v} = \omega\mathbf{u}$. The particle displacement $\mathbf{u}$ can be obtained from the global displacement field $\mathbf{U}$ via $\mathbf{u} = \mathbf{U}(x_2{=}0)$. The simulated excitability of the eight guided modes for the reference bone model was examined. Figure 4.19 shows the phase velocity spectrum of the eight reference modes superimposed by their excitability responses. Each dispersion curve and each point on the same curve has different excitability attribute. Mode 1's excitability peak exists around 0.2 MHz, which is also the most sensitive dispersion region to cortical thickness and velocities. However for higher order modes, the most sensitive regions do not usually overlap with those of the most excitable areas. The UGM excitation is not only affected by the excitability but also the attenuation nature of the guided modes. Further discussion will be beyond the focus of the current work and will be deferred later to a future communication.

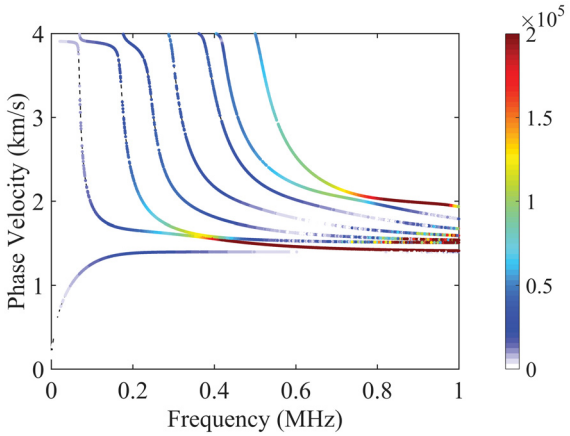

Figure 4.19: The dispersion spectrum of the first eight leaky lamb modes for the reference bone model, superimposed by their excitability. The color bar on the right indicates the the strength of excitability.

Finite element method is a numerical technique which provides an approximation of the solutions and the accuracy depends on the element size. Therefore, appropriate element discretization is important to reduce calculation errors and allow the FEM solutions to

converge to the exact solutions, i.e. a sufficient number of elements must be employed. Usually, at least eight linear elements per wavelength are required to achieve accurate simulation of UGM (Rose, 2014). A large number of elements with smaller element size can be chosen; however more and unnecessary computational time will be consumed. In this study, using eight elements per wavelength is sufficient to yield reasonable results (Nguyen *et al.*, 2017). It took less than one minute to calculate a dispersion profile for a bone model with a Windows 10 Pro 64-bit computer with Intel Core i7 4.00-GHz CPU and 32-Gb RAM.

This study has been designed to identify regions of sensitivity of UGM for the subsequent dispersion-curve inversion to assess cortical thinning in the prediction of osteoporosis and fracture risk. The analysis of guided-mode sensitiveness suggests that cortical thickness is a determinant of guided wave dispersion. It is possible to detect the phase velocity change with cortical properties. By means of frequency-phase velocity spectrum analysis, detectability was quantified with variability of soft tissue thickness, bone geometry and material properties. The material characteristics contribute differently to the dispersion map. Through the process, choosing the modes which are sensitive to the material properties of interest along with its sensitivity region is an important step to any successful inversion strategy. A multi-modal inversion approach of UGM allows more information to be exploited. Mode 1 should have high weighting in the misfit function due to its independence to soft tissue thickness especially when cortical thickness is the parameter of interest. Inverting the UGM dispersion data for bone properties can provide reliable information about the bone tissue status which has relevance for osteoporosis assessment. This study has also demonstrated that SAFE modeling is a powerful tool to gain insight into the ultrasound interaction with cortical bone in the presence of the surrounding tissues.

Chapter 5

Dipsersion Curve Inversion

In this chapter, I propose a nonlinear grid-search inversion algorithm to estimate the thickness and elastic velocities of long cortical bones, which are important determinants of bone strength, from axially-transmitted ultrasonic data. The inversion scheme is formulated in the dispersive frequency-phase velocity domain to recover bone properties. The method uses ultrasonic guided waves to retrieve overlying soft tissue thickness, cortical thickness, compressional, and shear-wave velocities of the cortex. The inversion strategy requires systematic examination of a large set of trial dispersion-curve solutions within a pre-defined model space to match the data with minimum cost in a least-squares sense. The theoretical dispersion curves required to solve the inverse problem, i.e. to extract bone parameters from the acquired ultrasound data, are computed for bilayered bone models using a semi-analytical finite-element method (Section 4.1). Developing accurate forward modeling algorithms plays a keystone to solve the model-based inverse problem to recover bone properties. The feasibility of the proposed approach is demonstrated using the numerically simulated data for a 1 mm soft tissue-5 mm bone bilayer and *ex-vivo* data from a bovine femur plate with an overlying 2 mm-thick soft-tissue mimic. The results show that the cortical thickness and wave speeds can be recovered with fair accuracy. The algorithm is also capable of inverting UGW dispersion energy branches from human tibia to infer for the thickness and velocities of the cortical bone with acceptable discrepancy. The bootstrap method is employed to statistically evaluate the inversion uncertainty and stability.

5.1 Nonlinear Grid-Search Inversion

5.1.1 Dispersion Curve Extraction

The multi-modal grid-search inversion scheme is formulated in the f-c domain to recover the bone properties. The phase-velocity dispersion curves of the UGW modes propagating

in cortical bone are sensitive to the cortical thickness and velocities (Tran *et al.*, 2018*a*). The inversion strategy is to systematically examine a set of trial dispersion curves within a pre-defined parameter space/dictionary to match the measured data, which minimizes the objective function in a least-squares sense. First, the f-c dispersion energy is extracted from the time-offset (t-x) multi-channel acquisition of UGW using high-resolution Radon transform method (Chapter 3; Tran *et al.*, 2014*a*; Tran *et al.*, 2014*b*). Next, the maximum intensity loci of the extracted dispersive energies are automatically traced to form the dispersion curves of the ultrasonic data.

5.1.2 Forward Modeling

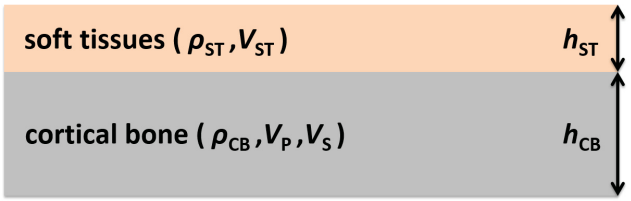

Figure 5.1: Cross section of a bilayered bone model.

The theoretical dispersion curves are solved for a bilayered isotropic and elastic bone plate overlaid by a fluid layer of finite thickness (Figure 5.1). Each layer is characterized by its thickness, density, and wave velocities. The semi-analytical finite-element method (Chapter 4; Nguyen *et al.*, 2017; Tran *et al.*, 2018*a*) has been employed to derive the dispersion characteristic equations in the frequency domain, which can be expressed by a quadratic eigen-value system as

$$\left[\mathbf{K}_1 + k^2\mathbf{K}_2 + \mathrm{i}k\mathbf{K}_3\right]\ \mathbf{V} = \mathbf{0} \tag{5.1}$$

where k denotes the wavenumber in the x direction; $\mathrm{i}^2 = -1$; $\mathbf{K}_1$, $\mathbf{K}_2$ and $\mathbf{K}_3$ are global mass- and rigidity-related matrices; the vector $\mathbf{V}$ consists of the global nodal pressures and displacements, which represent the wave structure associated to each mode.

By solving Equation 5.1 for each value of the angular frequency ω, the eigen-values k and the associated eigen-vectors, $\mathbf{V}(\omega,k)$ of guided modes can be determined. The frequency-dependent phase velocity c_p of a guided mode is obtained from k using the following relationship

$$c_\mathrm{p} = \frac{\omega}{\mathsf{Re}(k)} \tag{5.2}$$

where $\mathsf{Re}()$ is the real part of a complex quantity.

The forward calculation can be computationally intensive if the model space (or number of parameters) becomes large. Therefore, in order to minimize the computation cost of the inversion procedure, a data bank of possible solutions has been built in advance. The parameter ranges are as follows: 0 - 5 mm for soft tissue thickness h_{ST}, 1 - 10 mm for cortical thickness h_{CB}, 3000 - 4000 m/s for compressional-wave velocity (V_P), and 1500 - 2500 m/s for shear-wave velocity (V_S) with the incremental steps of 0.5 mm, 0.5 mm, 100 m/s, and 100 m/s respectively. The acoustic velocity of the soft tissue is assumed to be a constant 1500 m/s. Pre-computing the dispersion curves for a pre-defined model space avoids repeatedly executing the forward modeling step, thus speeding up the inversion process.

5.1.3 Grid-Search Algorithm

Figure 5.2a demonstrates the concept of grid search or parameter sweeping, which is basically a systematic search through each point in a pre-defined solution space to locate the optimal or best-fit bone model (Sen and Stoffa, 1995). The enumerative technique seeks the global rather than a local minimum in a multi-dimensional non-linear objective function (Figure 5.2b). The method is only practical when the number of inverted parameters is small (usually < 7) and the parameters lie within specific ranges of values (Menke, 2012).

In this study, the objective or misfit function J is defined in a least squared sense as the squared difference between the experimentally measured and theoretically calculated phase velocities, c^e and c^t,

$$J = \sum_{i=1}^{I} \sum_{j=1}^{J} (c_{i,j}^{e} - c_{i,j}^{t})^2 \tag{5.3}$$

where i is the number of existing guided modes and j is the number of dispersion points of each mode.

The parameter optimization is applied to the guided modes' dispersive energy loci to invert for the parameters of interest (POI), which are thickness of overlying soft tissue and cortical bone, compressional- and shear-wave velocities of the cortex. Figure 5.3 is a flowchart summarizing the grid-search optimization with a data bank, which holds all possible combinations of solutions within defined ranges of parameter values and increments. The method is conceptually simple and straightforward to implement. First, a pool of candidate dispersion curve solutions is generated from a pre-specified uniform grid of POI values. Secondly, the experimental dispersion curves are extracted from the Radon-transformed ultrasonic signals. Then the misfit function between experimental and theoretical dispersion

curves is evaluated in a multidimensional model space for the best-fit solution.

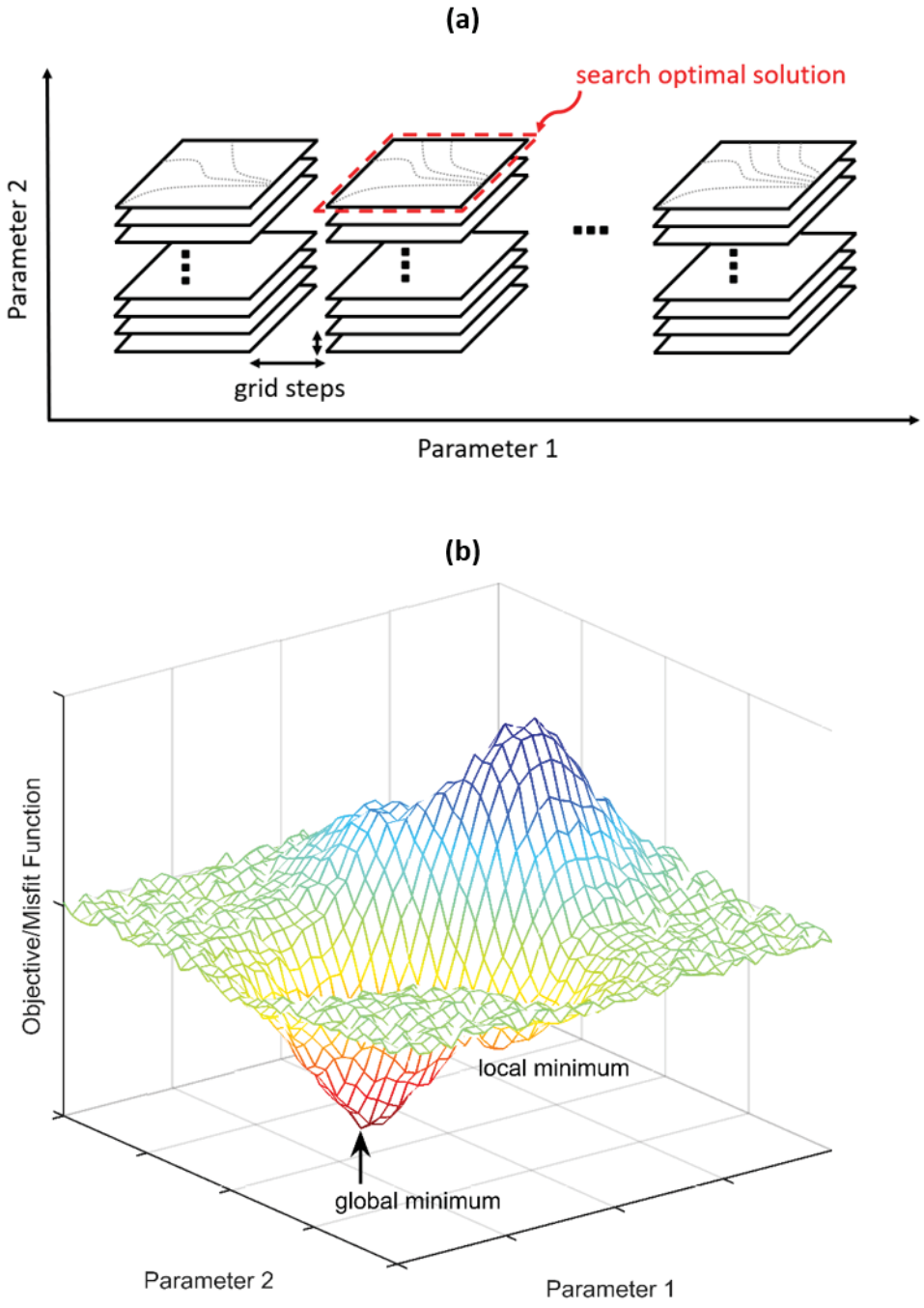

Figure 5.2: Illustration of the grid search optimization strategy using two parameters. (a) Pre-determined model space. (b) The technique seeks the global rather than a local minimum.

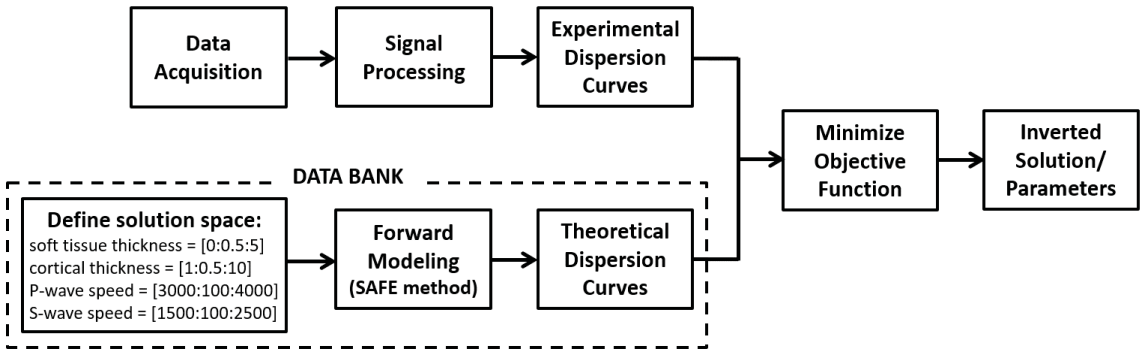

Figure 5.3: Flowchart of the grid-search optimization method.

5.1.4 Uncertainty Estimation by Bootstrapping

The bootstrap method was first introduced by Efron, 1979 for nonparametric error rate estimation problems. Bootstrapping can commonly be thought of as a cross validation approach. The method is employed to test the estimator's accuracy in small sample situations where conventional techniques are not valid (Ulrych and Sacchi, 2005). In clinical QUS application, the size of the data set is not sufficiently large due to time constraints in data acquisition to avoid patient motion or limited number of channels in an array. In practice, large data sample is inapplicable and the ultrasound scan can not be repeated many times, which keeps the patient in the clinics longer than necessary. Besides, there are estimated parameters with unknown true values, which can not be experimentally measured for verification. In this case, bootstrap technique offers some uncertainty measures of the parameters with respect to their unknown true values. Uncertainty estimate associated with the parameter optimization is important to avoid misleading data inference.

With bootstrapping, subsets of the observed data are randomly re-assigned and re-inverted for the bone properties. These re-sampling assignments are automatically input into the inversion scheme and treated as repeated measurements. After n repetitions, the mean and standard deviation (SD) of a POI estimate can be computed respectively by

$$\overline{\mathrm{POI}} = \frac{1}{n}\sum_{i=1}^{n}\mathrm{POI}_i \tag{5.4}$$

and

$$\sigma = \sqrt{\frac{1}{n-1}\sum_{i=1}^{n}(\mathrm{POI}_i - \overline{\mathrm{POI}})^2}. \tag{5.5}$$

5.2 Method Validation

5.2.1 Time-Domain Synthetic Data

Synthetic data for a 5 mm-thick bone plate with 1 mm-thick overlying soft tissues was used to validate the inversion algorithm. As described in Section 2.1.2, the cortex and the soft tissue are modeled as homogeneous, isotropic, and elastic solid and acoustic fluid, respectively. The compressional wave speed, shear wave speed, and mass density of the cortex were 3200 m/s, 2400 m/s, and 1930 kg/m^3 respectively. The properties are similar to those of human cortical bone (Tran *et al.*, 2018*a*). Ultrasound velocity and mass density of the soft tissue were 1700 m/s and 1000 kg/m^3, respectively. No absorption was assumed. The lower surface of the plate was assumed to be under traction-free condition and the upper surface of the fluid was excited by a point pressure force. The source wavelet was a time history function given by Tran *et al.*, 2014*b*

$$F(t) = F_0 e^{-4(f_c t-1)^2} \sin(2\pi f_c t) \tag{5.6}$$

where $F_0 = 1$ N.m^{-2} and the center frequency f_c was 1 MHz. A set of 64 ultrasound records were simulated with 1 mm spacing interval and a minimum offset of 20 mm. The numerical solution of this problem was computed by using an in-house code based on the time-domain finite element method which has been shown to be efficient for the simulation of ultrasound in bone plate coupled with fluids (Nguyen and Naili, 2011; Nguyen and Naili, 2012; Tran *et al.*, 2014*b*).

5.2.2 Inversion of Simulated Data

A numerically simulated dataset was used to validate the proposed grid-search technique. Figure 5.4 plots the 64-channel synthetic time signals (Figure 5.4a) and its corresponding dispersion map (Figure 5.4b). The time series were transformed into the dispersive f-c panel using the high-resolution Radon algorithm as described in Section 2.1.1. The dispersion curves were then obtained by locating the maximal-intensity at each frequency.

The combined grid search - bootstrap algorithm was applied to estimate the material properties from the simulated temporal wavefield. Bootstrap statistics with a sample size of 100 was utilized to evaluate the inversion uncertainty. The originally simulated data were re-sampled 100 times to produce 100 sub-datasets. Each sub-dataset included 32 records drawn at random from the primary 64 records. In every bootstrapping iteration, the optimal model solution was obtained by minimizing the misfit function between the dispersion curves of the re-sampled data and data-bank candidates.

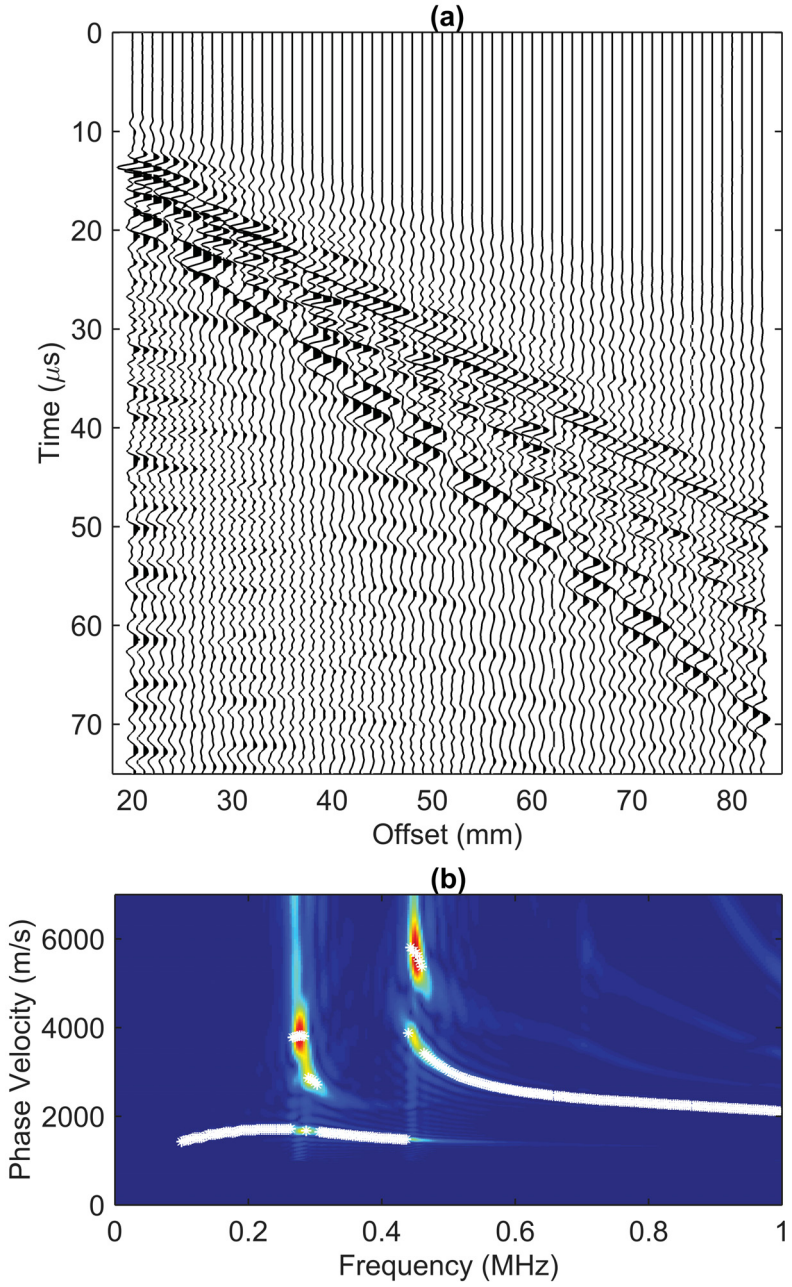

Figure 5.4: (a) Simulated waveforms of UGW propagating in a soft tissue-cortical bone bilayer and (b) the corresponding phase velocity dispersion panel. Superimposed white dots are the maximum intensity loci.

Table 5.1 summarizes the outcomes of grid-search inversion of the synthetic UGW signals and comparison with the reference POI values. The input parameters (h_{ST}, h_{CB}, V_{P}, and V_{S}) were accurately recovered. The thickness of soft tissue was precisely retrieved for 1 mm. The recovered cortical thickness ranges from 5 mm to 5.5 mm with a mean value of 5.025 mm and a standard deviation of 0.11 mm. Inverted compressional- and shear-wave speeds are 3211 ± 40 m/s and 2411 ± 31 m/s respectively. The small SDs signify that the inverted POI values are closely distributed around the mean quantities. This generally implies that the UGW inversion outcomes are relatively stable. Figure 5.5a displays the good fitting between the observed and predicted f-c spectra by the most popular recovered model, i.e., 1 mm h_{ST} - 5 mm h_{CB} - 3200 m/s V_{P} - 2400 m/s V_{S}. The first five fundamental guided modes were matched between the simulated and optimal models. The modes were named from 1 to 5 by the numbering nomenclature applied to leaky Lamb waves (Rose, 2014) because the bone model used in this study was a soft tissues-cortical bone bilayer. The misfit function graphs (Figures 5.5b and 5.5c) show its global minimum at 1 mm soft tissue and 5 mm cortex. The CPU processing time for 100 repetitions was 25.5 hours with a Windows 10 Pro 64-bit Intel Core i7 4.00-GHz CPU computer and 64-Gb RAM. Inversion of simulated wavefields has demonstrated the ability of parameter sweeping to effectively invert UGW energy traveling through the bone medium to retrieve cortical velocities and thickness.

Table 5.1: Comparison of the inverted and reference material properties

Experiment	POI	h_{ST} (mm)	h_{CB} (mm)	V_{P} (m/s)	V_{S} (m/s)
Simulation	Reference values	1	5	3200	2400
	Inverted values	1 ± 0	5.03± 0.11	3211 ± 40	2411 ± 31
Ex-vivo	Reference values	2	5.89	3886	N/A
	Inverted values	2.19 ± 0.24	6.16 ± 0.24	3881 ± 124	1783 ± 53
In-vivo	Reference values	3.25	5.25	4012	N/A
	Inverted values	3.08 ± 0.36	5.17 ± 0.42	3989 ± 63	2016 ± 56

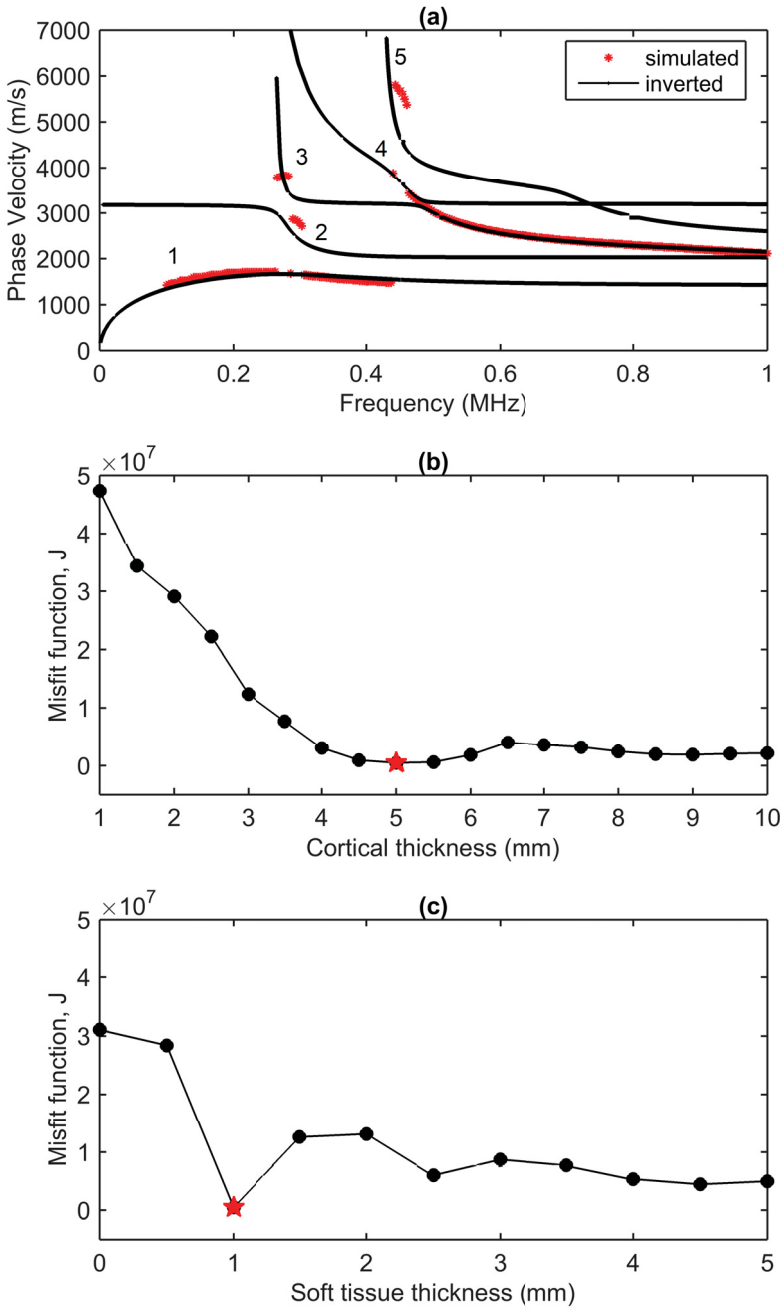

Figure 5.5: Simulated inversion experiment using the t-x data shown in Figure 5.4a. (a) Superposition of numerical simulation data (red) and the most popular inverted bone model (black) in f-c domain. The misfit function value varies with (b) cortical bone thickness and (c) soft tissue thickness. The global minimum is labeled with a red star.

5.3 Ex-vivo Data Inversion

5.3.1 Ex-vivo Ultrasound Measurement

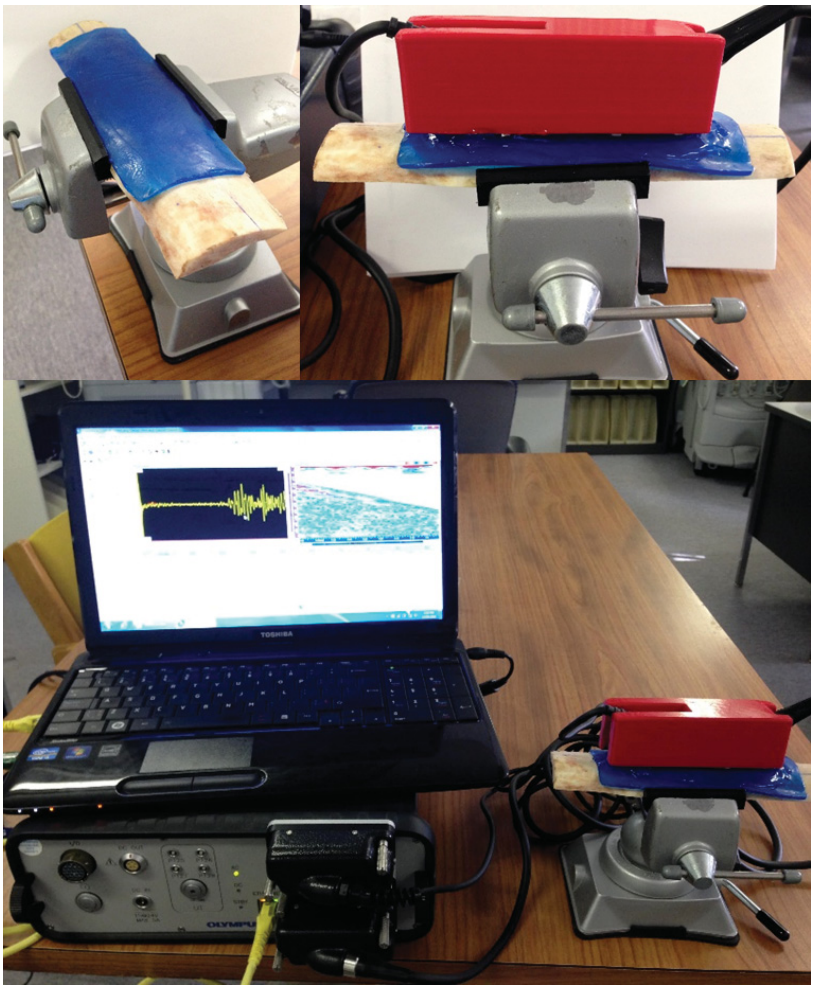

Figure 5.6: *Ex-vivo* experiment setup on bone phantom.

Following Nguyen *et al.*, 2014, the *ex-vivo* experiment was performed on a bovine femur plate with a 2 mm-thick tissue-mimicking material on top (Figure 5.6). A 220 mm × 45 mm bovine femur sample was cut along the long axis to make a bone plate with a mean thickness of 5.89 mm, measured by a digital caliper. The plate was cleaned; the soft tissue and marrow were completely removed. The soft tissue mimic is 2 mm thick and made of synthetic biopsy material (Blue Phantom^{TM}, USA). A TomoScan Focus LT^{TM} ultrasound scanner (Olympus NDT Inc., Canada) with 2 phased array transducers was used as shown in Figure 5.6 with one transducer being the transmitter and the other the receiver. The probes were placed in a 3D-printed housing to ensure their stabilization and to maintain their relative distance during data acquisition. Via an ethernet port, the system was connected to a Windows

7-based computer with TomoView^{TM} software to control the acquisition process and data export. The transmitter is a 16-element (2.25L16) probe pulsed at a central frequency of 1 MHz and the receiver is a 64-element (2.25L64) probe. Only five elements (out of the sixteen elements) were used as a group to transmit ultrasound. For the receiver, five elements were used as a group to generate a time series. Experiment was performed at room temperature of 22°C. A bench vise was used to clamp the bone plate in place. Ultrasound gel was applied to all contacting surfaces to ensure good coupling. A set of 60 ultrasound channels was recorded with 100 MHz sampling frequency, 0.75 mm spacing interval, and 21.75 mm closest offset.

5.3.2 Inversion of Bone Phantom Data

The proposed enumerative inversion technique has been applied to the *ex-vivo* dataset (Figure 5.7a) to estimate the cortical properties. Figure 5.7b shows the dispersion map of the recorded radiofrequency data. Similar to the simulation data above, we ran the bootstrap procedure to evaluate the performance of the inversion operator. The original *ex-vivo* 60-record dataset were resampled by randomly selecting 30 time series at a time. This resampling procedure was repeated 100 times to form the bootstrapping statistical analysis. The 100 bootstrap samples' estimates were used to calculate the mean and variance.

Using the iterative parameter optimization, the recovered values of h_{ST}, h_{CB}, V_{P}, and V_{S} were 2.190 ± 0.244 mm, 6.155 ± 0.243 mm, 3881 ± 124 m/s, and 1783 ± 53 m/s respectively. Despite the discrepancy of this *ex-vivo* experiment is bigger compared to the synthetic data case, the UGW inverted profile's accuracy is still acceptable. The estimates perform stably on a series of 100 test runs. A 2.19 mm-thick tissue layer on average is a good estimate to its true 2 mm thickness. The cortical thickness was reasonably determined as compared to the mean thickness 5.89 mm measured by a digital caliper. Cortical V_{P} was approximately determined by ray tracing to be 3886 m/s, which is close to the mean inverted value of 3881 m/s. The 6-mode matching between the experimentally measured dispersion spectrum and the inverted one is shown in Figure 5.8a. Figures 5.8b and 5.8c demonstrate the objective function in variation of cortical bone and soft tissue thickness. The misfit function is rough over the scale of the grid spacing with coexisting local minima and maxima. This illustrates the non-linearity of the bone inverse problem in hand. The J function reaches its global minimum at 2 mm-thick soft tissue - 6 mm-thick cortical bilayer.

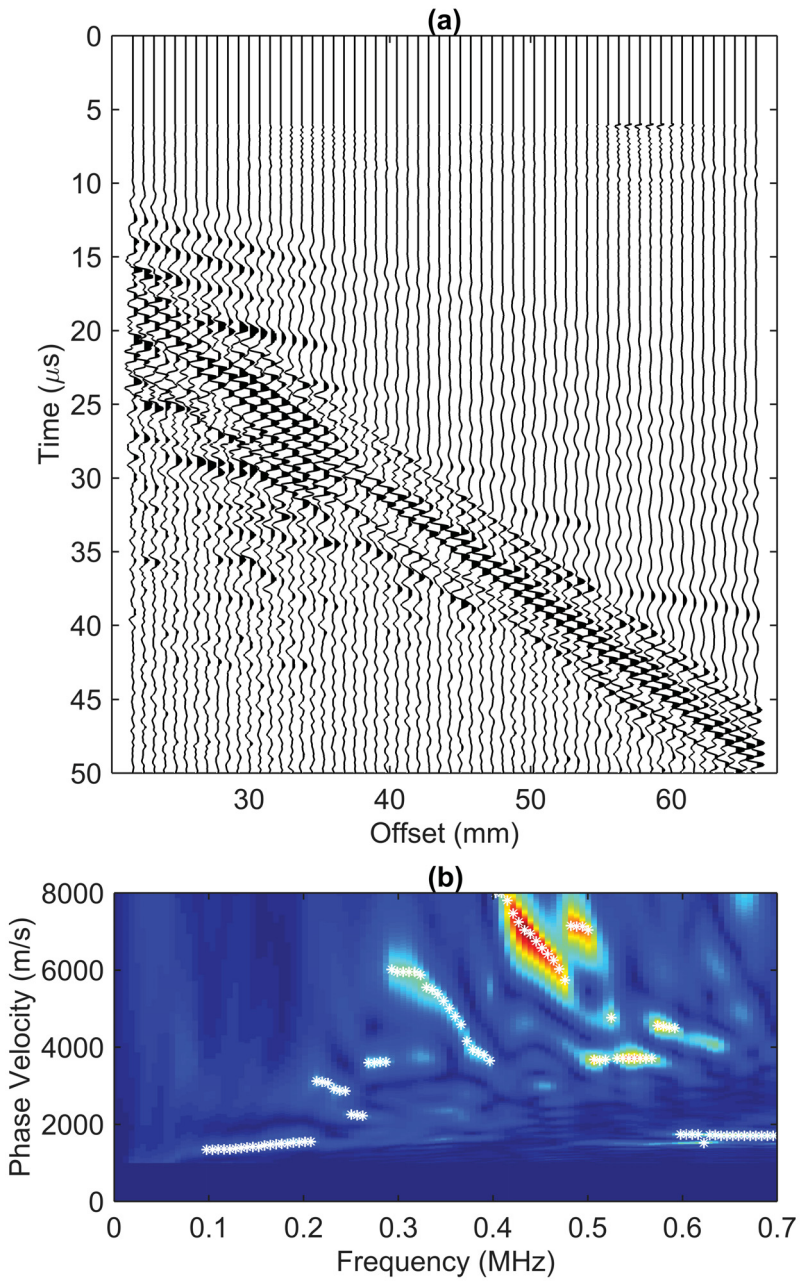

Figure 5.7: (a) Dispersive time signals measured from the *ex-vivo* experiment and (b) its dispersion map. Superimposed in white are the maximum intensity loci.

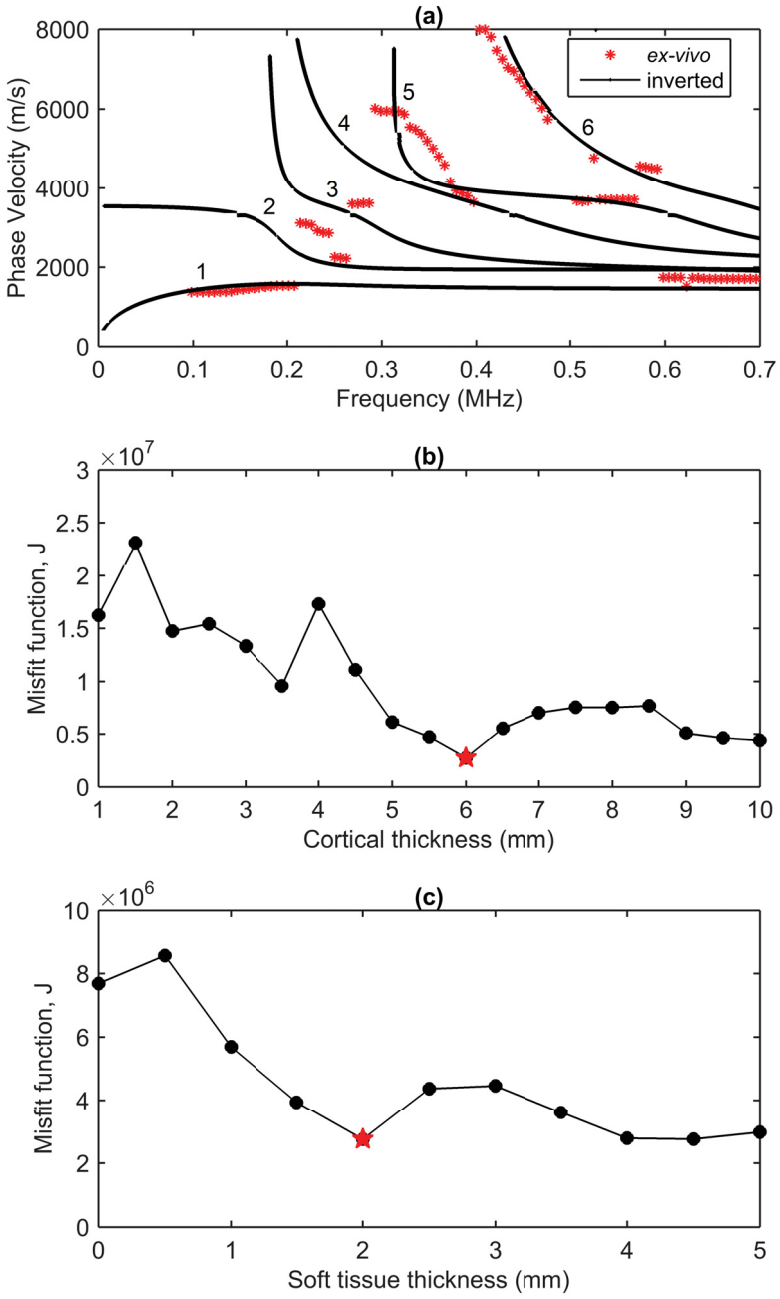

Figure 5.8: *Ex-vivo* inversion experiment using the t-x data shown in Figure 5.7a. (a) The measured dispersion spectrum (red) is fitted by the inverted bone model (shown in black). The objective function varies with (b) cortical bone thickness and (c) soft tissue thickness. The red star marks the global minimum of misfit.

5.4 In-vivo Data Inversion

5.4.1 Human Data Acquisition

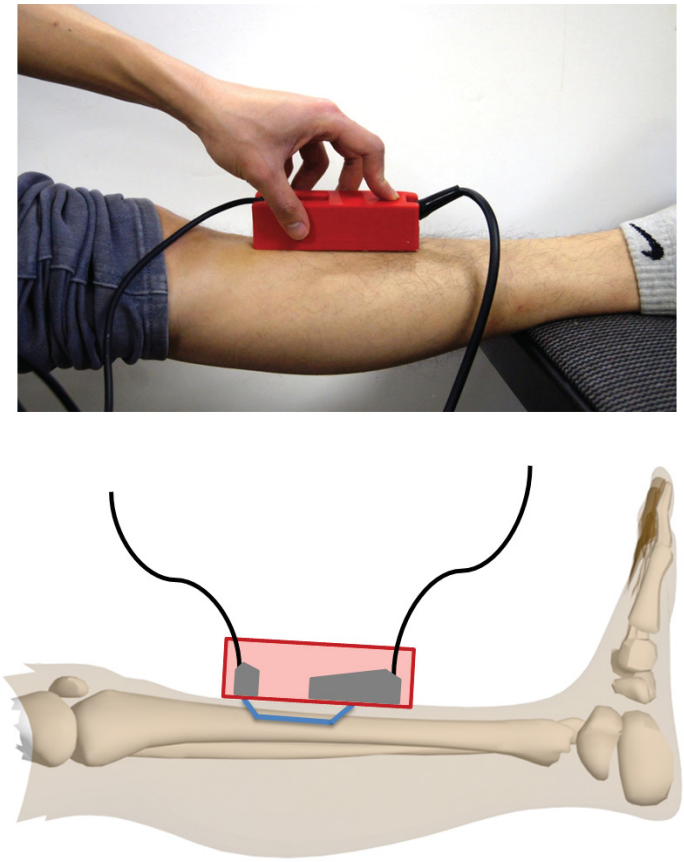

Figure 5.9: *In-vivo* axial transmission ultrasound scan on a human volunteer's tibia.

The *in-vivo* experiment was performed on the tibia of a 40-year-old female volunteer using axial transmission setup (Figure 5.9). Similar to the previous works (Le *et al.*, 2010; Tran *et al.*, 2014*a*; Tran *et al.*, 2014*b*), two 1-MHz compressional wave transducers (Panametrics C548, Waltham, MA, USA) were attached to two angle wedges (Panametrics ABWM-7T-30 deg). The transmitter was pulsed by a Panametrics 5800 P/R (Panametrics, Waltham, MA). During data acquisition, the leg of the subject rested on a chair. The transmitter was tightly held in contact with the skin surface by duct tape. One ruler, laid on the relatively flat section of the tibia and held in place by 3M™ medical tape (3M, St. Paul, MN, USA), was used to guide the receiver. Ultrasound gel (Aquasonic 100, Parker Laboratories, Inc, USA) was applied to all contact surfaces to ensure good coupling. The experiment was performed at room temperature of 22°C. The detected signals were digitized by and displayed on a 200-MHz digital storage oscilloscope (LeCroy 422 WaveSurfer, Chestnut

Ridge, NY). A set of 40 ultrasound records was acquired with 2 mm spacing interval and 46 mm closest offset (Figure 5.10a). The aperture of the acquisition was 78 mm. Each record was averaged 32 times during acquisition to eliminate random noise and increase signal-to-noise ratio. The recorded signals were further decimated to 1050 points per channel for a final sampling interval of 0.1 μs.

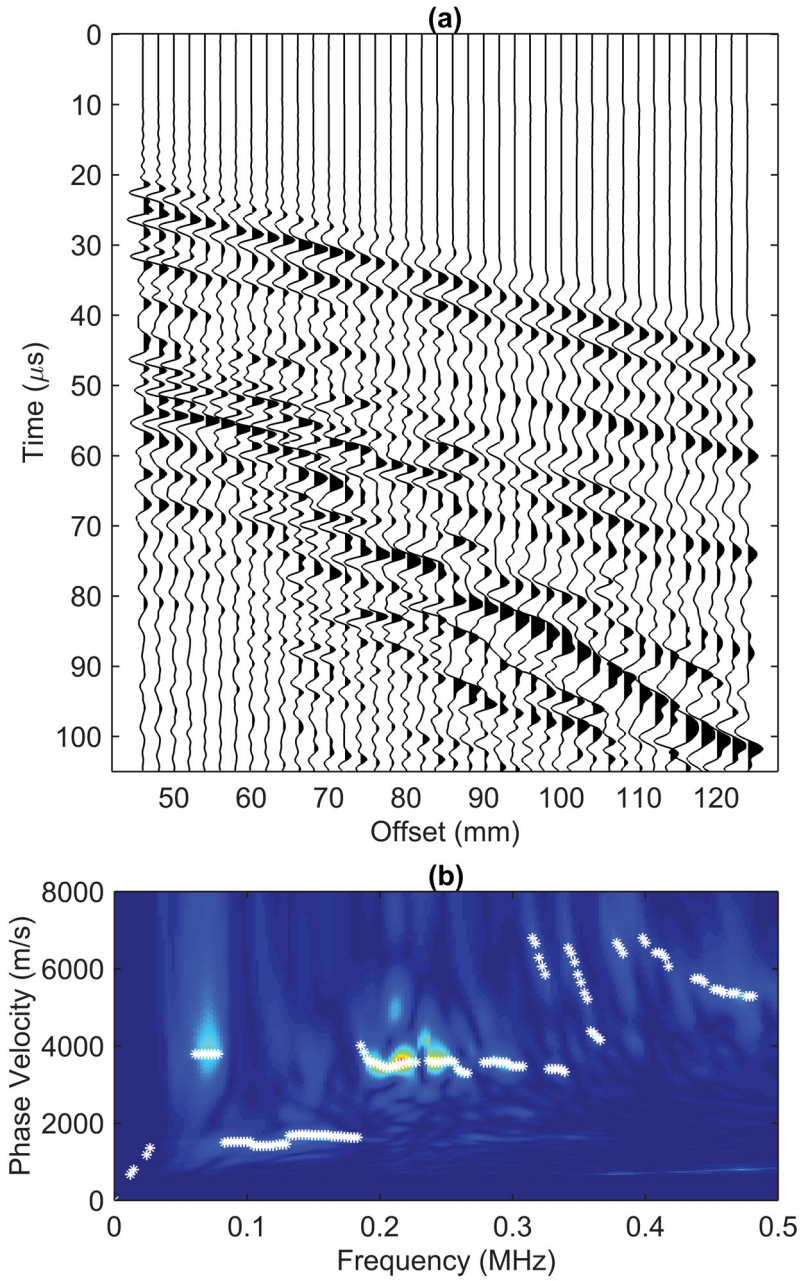

Figure 5.10: (a) The multi-channel dispersive data acquired from the *in-vivo* experiment on the right tibia of a female volunteer and (b) its dispersion map. Superimposed in white are the maximum intensity loci.

5.4.2 Inversion of In-vivo Data

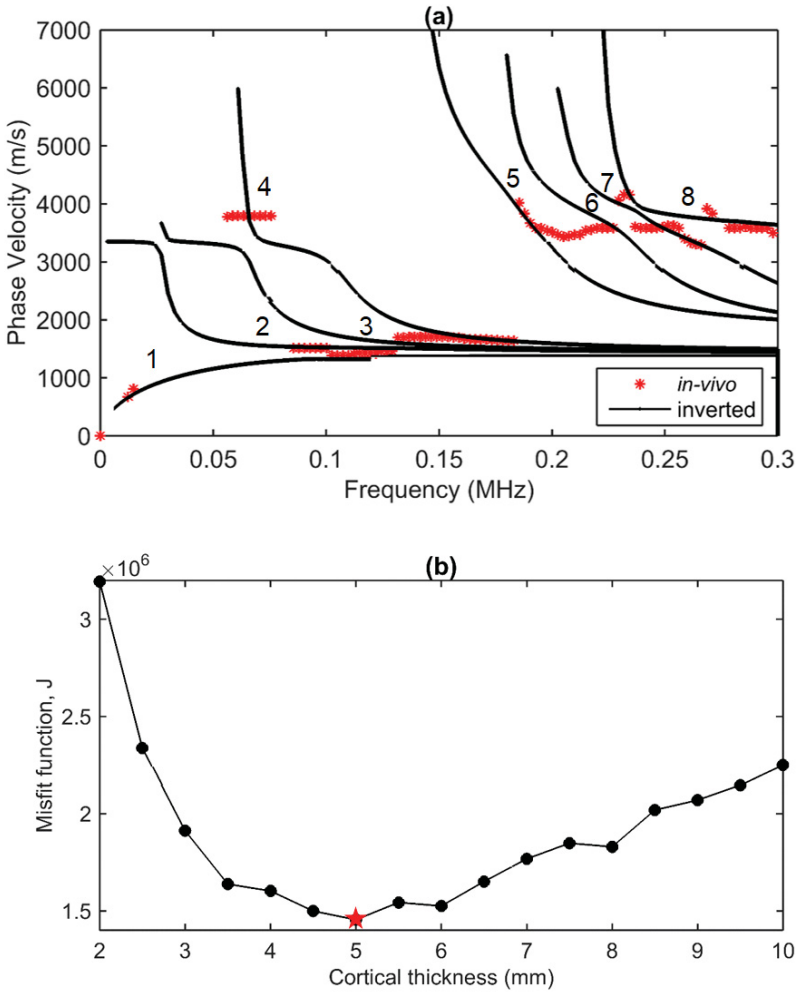

Figure 5.11: *In-vivo* inversion experiment using the t-x data shown in Figure 5.10a. (a) The measured dispersion spectrum (red) is fitted by the inverted bone model (shown in black). The objective function varies with (b) cortical bone thickness. The red star marks the global minimum of misfit.

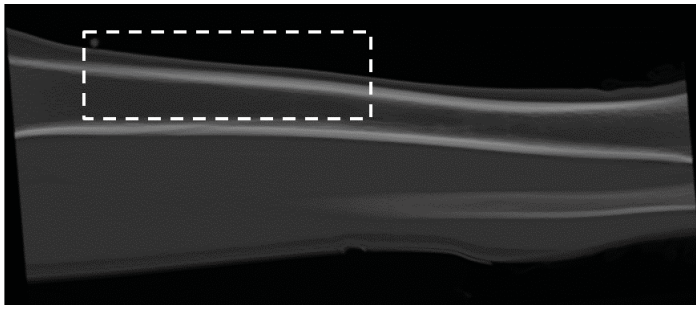

Figure 5.12: A radiograph of the volunteer's tibia. The white-dashed rectangle outlines the area used to estimate the tissue and bone thickness.

The grid search-bootstrapping inversion scheme was then applied to the *in-vivo* tibial UGW data described above (Figure 5.10a). Figure 5.10b is the dispersion map of the human subject's radiofrequency data. The original *in-vivo* 40-record dataset were resampled by randomly selecting 20 time series at a time. Again, the resampling was repeated 100 times to establish the bootstrapping statistics. The recovered values of soft tissue thickness h_{ST}, bone thickness h_{CB}, V_{P}, and V_{S} were 3.08 $\pm$ 0.35 mm, 5.17 $\pm$ 0.42 mm, 3989 $\pm$ 63 m/s, and 2016 $\pm$ 56 m/s respectively. The inverted profile's accuracy is considerably fair. The soft tissue and cortical thicknesses were reasonably determined compared to the mean thicknesses of 3.25 mm and 5.25 mm respectively measured from the CT radiograph (Figure 5.12). Cortical V_{P} was estimated by ray tracing method to be approximately 4012 m/s, which is very close to the mean inverted value of 3989 m/s. 8 guided modes matched between the *in-vivo* dispersion and the inverted spectra as shown in Figure 5.11a. Figures 5.11b graphs the misfit function J with respect to cortical bone thickness. The objective function reaches global minimum with 5 mm-thick cortex.

5.5 Correlation of Ultrasonic Velocity with Bone Mineral Density

The ultrasonic data were collected at a Medical Imaging Consultant (MIC) clinic in Edmonton with ethics approval from the University of Alberta - Health Research Ethics Board (No. Pro00047967). 100 consented subjects, who had bone densitometry examinations, were recruited. The left mid-tibia was chosen as the measured site for this clinical trial. Each subject was scanned 3 times using the TomoScan Focus LT^{TM} phased array ultrasound system (Figure 5.6) with different beam-steering configurations at a fixed transmitter-receiver distance. Data from 20 subjects aged 50 to 80 years were used for a pilot study. The mid-tibial ultrasound velocity could then be estimated from each dataset. The average speed was estimated from the 3 ultrasound records for each subject. The cortical speed of sound was found to increase ($R^2 = 0.337$) with bone mineral density (Figure 5.13), i.e. they are sensitive to osteoporosis-related changes in bone. This may be due to the trabecularization of cortical bones, leading to cortical thinning and increasing intra-cortical porosity. The preliminary result will be used as a basis for the analysis of the remaining subjects' data and to further examine the relationship between ultrasonic parameters and skeletal health status.

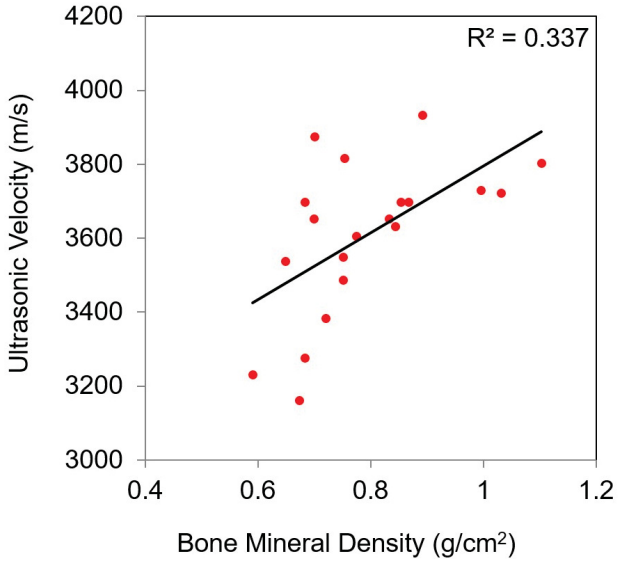

Figure 5.13: Correlation of ultrasonic velocity with the subjects' bone mineral density measured by DXA.

5.6 Discussions

This chapter presented the scheme of model-based grid-search inversion of UGW in long bones, including the dispersion curve extraction, forward modeling as well as the inverse formulation. The relationship between the measurement data and the model is nonlinear. The inversion was based on a global optimization of a dispersion misfit function between the modeled and measured UGW data. The phase velocity maps of the guided modes were inverted for the geometrical and mechanical characteristics of cortex. The feasibility of the proposed method to extract the cortical properties of interest was demonstrated by its application on numerical simulation data from bilayered bone model, *ex-vivo* experimental dataset from bone phantom, and also *in-vivo* data.

Creating a large solution database has reduced the computational expense significantly when solving the inverse problem in hand. However, the grid-search scheme can still be computationally expensive because it tries out all possible combinations of the model properties' values. The methodical technique performs an exhaustive search in the solution space by sequentially computing the corresponding values of the objective function. While about 10 minutes are needed on a 24 core computer (Intel Xeon CPU E5-2620 v2 @ 2.10 GHz) for genetic algorithm to solve the bone inverse problem for a single dataset (Bochud *et al.*, 2016), the proposed grid search technique needs around 10 to 15 minutes for one run depending on the data size on a Intel Core i7 4.00-GHz CPU - 64-Gb RAM desktop computer. Note

that both methods do not use the same datasets for calculation and do not run on the same computer therefore the comparison is relative. Although the current computational speed is acceptable as an offline imaging method at this stage, the time efficiency of the inversion algorithm needs to be improved for real-time bone quality diagnosis. This can be possibly done by adjusting the grid spacing in model space, i.e. the parameter increment values used for forward calculation. But it should be born in mind that sampling the parameter grid too coarsely results in missed solutions or lower-resolution output whereas fine sampling results in excessive computational cost. Another drawback of the grid search is that it can be a tedious problem when dealing with more POIs or very large-sized data set.

It is worth mentioning that each mode has a different dispersive sensitivity to the model parameters (Tran *et al.*, 2018*a*). One mode's propagation characteristics might be more sensitive to the parameter variation than the others. In future works, an overall objective function, denoted by the weighted sum of the misfit functions from all existing modes in the data, might be investigated. Generally, larger weighting coefficients should be assigned to the UGW modes that have higher sensitivities to the favorable properties. Another possibility is that the guided modes can be inverted separately. The rationale behind this choice is that the fundamental mode contains more dispersive energy, is independent to soft tissue thickness, is sensitive to cortical thickness (Tran *et al.*, 2018*a*), and is easier to be separated from the higher-order modes by means of wavefield separation technique (Tran *et al.*, 2014*a*; Tran *et al.*, 2014*b*).

Boot strapping technique is a valuable tool to provide statistical confidence to the inverted parameters when their true values are not known and the sample size is small. The technique is particularly practical when dealing with QUS data where the number of time series per acquisition can only goes up to 128 and repeated measurements at various positions in a clinical setting is generally impossible. In the lack of shear wave information of the cortical plate in the *ex-vivo* study, V_S was determined to be 1783$\pm$53 m/s, where the small variance provides us valuable indication and guidance about the performance of the grid-search method and the trustworthiness of the recovered V_S value. Similarly, with the boot strapping method, the proposed inversion strategy can be used to recover the transverse compressional velocity of the cortical bone in future studies.

Chapter 6

Conclusions and Future Directions

6.1 Summary and Contributions of this Thesis

Numerical and experimental studies were performed to investigate the validity and applicability of UGW-based cortical bone characterization. The bone inverse problem in hand is significant but also challenging due to complicated ultrasound interaction of cortical bone under the impact of surrounding soft tissues. Multiple modes are excited when guided waves propagate in thin structures like cortical bone which makes the propagation law become complex. The main positive findings of this thesis are summarized as follows:

- High-resolution Radon transform offers a robust and powerful technique to analyze the multi-channel axially-transmitting UGW signals from long cortical bones. HRRT supplements the current signal-processing (Fourier- or SVD-based) techniques especially when the data acquisition aperture is limited and uneven station sampling occurs in clinical routine. The method's efficacy has been proven in extracting guided modes, reconstructing wave field, and importantly enhancing imaging resolution of dispersive guided wave energies.

- SAFE simulation has been validated to be a sophisticated and accurate computational tool to calculate dispersion characteristics of UGW propagating in layered bone structures and to gain insight into the ultrasound-bone interaction.

- UGW sensitivity to material properties has been well demonstrated by means of phase-velocity spectrum analysis. This again supports the claim that it is possible to detect cortical geometrical and mechanical changes with UGW dispersion curves.

- The model-based dispersion optimization approach, which was formulated in frequency-phase velocity domain in a multi-variable and multi-modal manner, reliably recovered

cortical tissue properties from UGW data. The approximate solutions could be non-unique and unstable for experimental noisy signals but the error is acceptable.

- Cortical bone thickness and mechanics contribute to the mechanical competence and fragility of the whole bone. Cortical bone property estimation provided meaningful information about the bone health status relevant to osteoporosis. Therefore, simultaneous measurement of site-specific cortical thickness and mechanics properties may improve the clinical estimation of fracture risk and facilitate effective management of osteoporosis.

This research improves the current fundamental understanding of the UGW propagation in long bones and fosters the application of ATU in non-invasive cortical thinning assessment to diagnose osteoporosis. Even though a true gray-scale bone sonogram will be unfeasible, guided wave ultrasonography can be expected to become more widely clinical use in the near future to complement X-ray based medical imaging modalities for screening and diagnosis of skeletal diseases.

6.2 Limitations of this Thesis

Despite the encouraging results, there were certain weaknesses in undertaking this research work:

- The mechanics of the bone model to simulate dispersion characteristics of UGW was assumed to be homogeneous, elastic, and transversely isotropic.
- The solution domain was limited in terms of resolution. The thickness and velocity resolutions were 0.5 mm and 100 m/s respectively. This reduces the ability to detect bone tissue changes below the imaging resolution.
- The current computational cost is not low enough for real-time imaging of cortical bone in clinical practice.
- Being a pilot trial, the sample size was restricted. The small number of clinical datasets limited the statistical reliability of the results.

6.3 Recommendations for Future Work

The following research areas should be considered in future studies to advance bone guided wave ultrasound:

- In terms of data acquisition, ultrasonic guided mode excitation, excitability, and selectivity are good research topics. Selective modal excitation can be achieved by beam steering, i.e. beam directivity and divergence. From our clinical experience, some UGM are more strongly excited than the others. Development of experimental protocols enabling optimal excitation and transmission of UGW should be investigated to enhance the modes' excitability.

- The inversion accuracy and precision can possibly be improved by refining the parameter grids leading to higher resolution bone models. A multi-layer cylindrical waveguide, which has closer similarity to human long bone geometry, should also be looked into.

- More bone properties, e.g. attenuation and porosity, and a weighted objective function should be considered in the inversion process to take into account the different sensitivity level of UGM. The computation cost needs to speed up for real-time assessment. In order to do that, other high-performance dynamic programming languages such as C++ or Julia are attractive to replace the current Matlab codes. Full-waveform inversion is also a promising and appealing research direction.

- To achieve a more meaningful clinical validation, expansion of the study population is necessary, not only in Canada but also abroad through international collaboration. Comparative studies can be conducted to correlate the extracted ultrasonic indicators with the current gold-standard DXA-BMD or other diagnostic modalities such as pQCT and micro-computed tomography (μCT). The correlation of axial transmission with other ultrasonic techniques like transverse transmission and backscattering is an interested research question.

- Ultrasound velocity is probably the most difficult parameter to measure accurately with high reproducibility especially *in-vivo*. Many factors are potential sources of error including operator experience. The participant of multiple raters in the data collection and analysis will make inter-rater reliability and cross validation possible.

- The ATU methodologies can be extended to the development of ultrasound-based inspection techniques for many other applications such as bone fracture detection, fracture healing monitoring, bone fatigue evaluation, brain imaging, and therapeutic ultrasound, and neural activity tracking.

Bibliography

Alleyne, D. and P. Cawley (1991). A 2-dimensional Fourier-transform method for the measurement of propagating multimode signals. *J Acoust Soc Am* **89**, 1159–1168.

Anast, G.T., T. Fields and I.M. Siegel (1958). Ultrasonic technique for the evaluation of bone fractures. *Am J Phys Med* **37**, 157–159.

Andrews, H. and C. Patterson (1976). Singular value decompositions and digital image processing. *IEEE Trans Acoust Speech Signal Process* **24**, 26–53.

Bernard, A., M.J.S. Lowe and M. Deschamps (2001). Guided waves energy velocity in absorbing and non-absorbing plates. *J Acoust Soc Am* **110**, 186–196.

Bernard, S., V. Monteiller, D. Komatitsch and P. Lasaygues (2017). Ultrasonic computed tomography based on full-waveform inversion for bone quantitative imaging. *Phys Med Biol* **62**, 7011–7035.

Bochud, N., Q. Vallet, J.G. Minonzio and P. Laugier (2017). Predicting bone strength with ultrasonic guided waves. *Sci Rep* **7**, 43628.

Bochud, N., Q. Vallet, Y. Bala, H. Follet, J.G. Minonzio and P. Laugier (2016). Genetic algorithms-based inversion of multimode guided waves for cortical bone characterization. *Phys Med Biol* **61**, 6953–6974.

Bossy, E., M. Talmant and P. Laugier (2002). Effect of bone cortical thickness on velocity measurements using ultrasonic axial transmission: a 2D simulation study. *J Acoust Soc Am* **112**, 297–307.

Bossy, E., M. Talmant, F. Peyrin, L. Akrout, P. Cloetens and P. Laugier (2004). An in vitro study of the ultrasonic axial transmission technique at the radius: 1-MHz velocity measurements are sensitive to both mineralization and intracortical porosity. *J Bone Miner Res* **19**, 1548–1556.

Camus, E., M. Talmant, G. Berger and P. Laugier (2000). Analysis of the axial transmission technique for the assessment of skeletal status. *J Acoust Soc Am* **108**, 3058–3065.

Capon, J. (1969). High-resolution frequency-wavenumber spectrum analysis. *Proc IEEE* **57**, 1408–1418.

Capozza, R.F., S. Feldman, P. Mortarino, P.S. Reina, H. Schiessl, J. Rittweger, J.L. Ferretti and G.R. Cointry (2010). Structural analysis of the human tibia by tomographic (pQCT) serial scans. *J Anat* **216**, 470–481.

Carcione, J. (2001). *Wave fields in real media: Wave propagation in anisotropic, anelastic and porous media*. The Netherlands: Elsevier.

Cawley, P., M.J.S. Lowe, D.N. Alleyne, B. Pavlakovic and P.D. Wilcox (2003). Practical long range guided wave testing: applications to pipes and rail. *Mater Eval* **61**, 66–74.

Chapman, C.H. (1978). A new method for computing synthetic seismograms. *Geophysical Journal of the Royal Astronomical Society* **54**, 481–518.

Chen, J., J. Foiret, J. Minonzio, M. Talmant, Z. Su, L. Cheng, and P. Laugier (2012). Measurement of guided mode wavenumbers in soft tissue-bone mimicking phantoms using ultrasonic axial transmission. *Phys Med Biol* **57**, 3025–3037.

Chiras, D.D. (2013). *Human biology (Chapter 10)*. Burlington, MA, USA: Jones and Bartlett Learning.

Coccia, S., I. Bartoli, A. Marzanic, F. Lanza di Scaleaa, S. Salamoned and M. Fateh (2011). Numerical and experimental study of guided waves for detection of defects in the rail head. *NDT E Int* **44**, 93–100.

Culjat, M. O., D. Goldenberg, P. Tewari and R. S. Singh (2010). A review of tissue substitutes for ultrasound imaging. *Ultrasound Med Biol* **36**, 861–873.

Daubechies, I., R. DeVore, M. Fornasier and C.S. Gunturk (2010). Iteratively reweighted least squares minimization for sparse recovery. *Commun Pure Appl Math* **63**, 1–38.

Decker, K.T. and M.M. Haney (2010). Guided waves in GPR data: depth imaging and analysis of phase and group velocities. *Society of Exploration Geophysicists Technical Program Expanded Abstracts* **2010**, 1866–1870.

Docstoc (2012). http://docstoc.com/docs/21874509/blank-long-bone-diagram, accessed September 2012.

Efron, B. (1979). Bootstrap methods: Another look at the jackknife. *Ann Stat* **7**, 1–26.

Engl, H.W. and W. Grever (1994). Using the L-curve for determining optimal regularization parameters. *Numer Math* **69**, 25–31.

Firouzi, K., A. Nikoozadeh, E.T. Carver and T.B. Khuri-Yakub (2016). Lamb wave multitouch ultrasonic touchscreen. *IEEE Trans Ultrason Ferroelect Freq Control* **63**, 2174–2186.

Foiret, J., J.G. Minonzio, C. Chappard, M. Talmant and P. Laugier (2014). Combined estimation of thickness and velocities using ultrasound guided waves: a pioneering study on in vitro cortical bone samples. *IEEE Trans Ultrason Ferroelectr Freq Control* **61**, 1478–1488.

Foster, D.J. and C.C. Mosher (1992). Suppression of multiple reflections using the Radon transform. *Geophys* **57**, 386–395.

Freire, S.L.M. and T.J. Ulrych (1988). Application of singular value decomposition to vertical seismic profiling. *Geophys* **53**, 778–785.

Gao, H. and J.L. Rose (2010). Goodness dispersion curves for ultrasonic guided wave based SHM: a sample problem in corrosion monitoring. *Aeronaut J* **114**, 49–56.

Gao, H.D. and J.L. Rose (2009). Ice detection and classification on an aircraft wing with ultrasonic shear horizontal guided waves. *IEEE Trans Ultrason Ferroelectr Freq Control* **56**, 334–344.

Greenhalgh, S.A., I.M. Mason, C.C. Mosher and E. Lucas (1990). Seismic wavefield separation by multicomponent τ-p polarisation filtering. *Tectonophysics* **173**, 53–61.

Gu, Y.J. and M.D. Sacchi (2009). Radon transform methods and their applications in mapping mantle reflectivity structure. *Surv Geophys* **30**, 327–354.

Gullberg, B., O. Johnell and J.A. Kanis (1997). World-wide projections for hip fractures. *Osteoporosis Int* **7**, 407–413.

Gurkan, U.A. and O. Akkus (2008). The mechanical environment of bone marrow: a review. *Ann Biomed Eng* **36**, 1978–1991.

Hacihaliloglu, I., R. Abugharbieh, A.J. Hodgson and R.N. Rohling (2011). Automatic adaptive parameterization in local phase feature-based bone segmentation in ultrasound. *Ultrasound Med Biol* **37**, 1689–1703.

Hata, T., Y. Nagatani, K. Takano and M. Matsukawa (2016). Simulation study of axial ultrasonic wave propagation in heterogeneous bovine cortical bone. *J Acoust Soc Am* **140**, 3710–3717.

Herman, G.T. (1980). *Image reconstruction from projections-The fundamentals of computerized tomography*. Oxford, UK: Academic Press, Elsevier.

Hoffmeister, B.K., A.R. Wilson, M.J. Gilbert and M.E. Sellers (2012). A backscatter difference technique for ultrasonic bone assessment. *J Acoust Soc Am* **132**, 4069–4076.

Hughes, T.J.R. (2000). *The finite element method: linear static and dynamic finite element analysis*. Mineola, NY, USA: Dover Publications, Inc.

Jansson, T., M. Almqvist, K. Strahlen, R. Eriksson, G. Sparr, H.W. Persson and K. Lindstrom (1997). Ultrasound Doppler vector tomography measurements of directional blood flow. *Ultrasound Med Biol* **23**, 47–57.

Jones, I.F. and S. Levy (1987). Signal-to-noise ratio enhancement in multichannel seismic data via the Karhunen-Loéve transform. *Geophys Prospect* **35**, 12–32.

Kanasewich, E.R. (1981). *Time sequence analysis in geophysics*. Edmonton, AB, Canada: The University of Alberta Press.

Kim, Y.H., D.H. Kim, J.H. Han and C.G. Kim (2007). Damage assessment in layered composites using spectral analysis and Lamb wave. *Compos Part B Eng* **38**, 800–809.

Korneev, V.A., R.M. Nadeau and T.V. McEvilly (2003). Seismological studies at Parkfield IX: fault-zone imaging using guided wave attenuation. *B Seismol Soc Am* **93**, 1415–1426.

Langton, C.M. and C.F. Njeh (2008). The measurement of broadband ultrasonic attenuation in cancellous bone: a review of the science and technology. *IEEE Trans Ultrason Ferroelectr Freq Control* **55**, 1546–1554.

Laugier, P. and G. Haiat (2011). *Bone quantitative ultrasound*. The Netherlands: Springer.

Le, L.H. (1998). An investigation of pulse-timing techniques for broadband ultrasonic velocity determination in cancellous bone: a simulation study. *Phys Med Biol* **43**, 2295–2308.

Le, L.H., T.N.H.T. Tran and M.D. Sacchi (2013). Radon or τ-p transform: a new tool to image dispersive guided-wave energies in long bones. *The Proceeding of 5th European Symposium on Ultrasonic Characterization of Bone* **2013**, 52–53.

Le, L.H., Y.J. Gu, Y.P. Li and C. Zhang (2010). Probing long bones with ultrasonic body waves. *Appl Phys Lett* **96**, 114102.

Lee, C.M., J.L. Rose and Y.H. Cho (2009). A guided wave approach to defect detection under shelling in rail. *NDT E Int* **42**, 174–180.

Lee, K.I. and S.W. Yoon (2004). Feasibility of bone assessment with leaky Lamb waves in bone phantoms and a bovine tibia. *J Acoust Soc Am* **115**, 3210–3217.

Lefebvre, F., Y. Deblock, P. Campistron, D. Ahite and J.J. Fabre (2002). Development of a new ultrasonic technique for bone and biomaterials in vitro characterization. *J Biomed Mater Res* **63**, 441–446.

Leslie, W.D., S. O'Donnell, C. Lagacé, P. Walsh, C. Bancej, S. Jean, K. Siminoski, S. Kaiser, D.L. Kendler and S. Jaglal (2010). Population-based Canadian hip fracture rates with international comparisons. *Osteoporosis Int* **21**, 1317–1322.

Li, H., L.H. Le, M.D. Sacchi and E. Lou (2013). Ultrasound imaging of long bone fractures and healing with split-step Fourier imaging method. *Ultrasound Med Biol* **39**, 1482–1490.

Liu, C., F. Xu, D. Ta, T. Tang, Y. Jiang, J. Dong, W.P. Wang, X. Liu, Y. Wang and W.Q. Wang (2016). Measurement of the human calcaneus in vivo using ultrasonic backscatter spectral centroid shift. *J Ultrasound Med* **35**, 2197–2208.

Louis, A.K. (1992). Medical imaging: state of the art and future development. *Inverse Probl* **8**, 709–738.

Lowe, M.J.S. (2002). Guided waves in structures. *Encyclopedia of vibration* pp. 1551–1559.

Luo, Y., J. Xia, R.D. Miller, J. Liu, Y. Xu and Q. Liu (2008*a*). Application of high-resolution linear Radon transform for Rayleigh-wave dispersive energy imaging and mode separating. *Society of Exploration Geophysicists Technical Program Expanded Abstracts* **2008**, 1233–1237.

Luo, Y., J. Xia, R.D. Miller, Y. Xu, J. Liu and Q. Liu (2008*b*). Rayleigh-wave dispersive energy imaging using a high-resolution linear Radon transform. *Pure Appl Geophys* **165**, 903–922.

Marcus, R., D. Feldman, D.A. Nelson and C.J. Rosen (2008). *Osteoporosis*. Oxford, UK: Academic Press, Elsevier.

Marple, S.L. (1987). *Digital spectral analysis with applications*. Upper Saddle River, NJ, USA: Prentice Hall, Inc.

Masserey, B., L. Aebi and E. Mazza (2006). Ultrasonic surface crack characterization on complex geometries using surface waves. *Ultrasonics* **44**, e957–e961.

McMechan, G.A. and M.J. Yedlin (1981). Analysis of dispersive waves by wave field transformation. *Geophys* **46**, 869–874.

Menke, W. (2012). *Geophysical data analysis: Discrete inverse theory*. Oxford, UK: Academic Press, Elsevier.

Mesquita, A.Q., G. Barbieri and C.H. Barbieri (2016). Correlation between ultrasound velocity and densitometry in fresh and demineralized cortical bone. *Clinics* **71**, 657–663.

Michaels, T.E., J.E. Michaels and M. Ruzzene (2011). Frequency-wavenumber domain analysis of guided wavefields. *Ultrasonics* **51**, 452–466.

Minonzio, J.G., J. Foiret, P. Moilanen, J. Pirhonen, Z. Zhao, M. Talmant, J. Timonen and P. Laugier (2014). A free plate model can predict guided modes propagating in tubular bone-mimicking phantoms. *J Acoust Soc Am* **137**, EL98–EL104.

Minonzio, J.G., M. Talmant and P. Laugier (2010). Guided wave phase velocity measurement using multi-emitter and multi-receiver arrays in the axial transmission configuration. *J Acoust Soc Am* **127**, 2913–2919.

Moilanen, P. (2008). Ultrasonic guided waves in bone. *IEEE Trans Ultrason Ferroelectr Freq Control* **55**, 1277–1286.

Moilanen, P., P.H.F. Nicholson, V. Kilappa, S. Cheng and J. Timonen (2006). Measuring guided waves in long bones: modeling and experiments in free and immersed plates. *Ultrasound Med Biol* **32**, 709–719.

Moilanen, P., V. Kilappa, P.H.F. Nicholson, J. Timonen and S. Cheng (2004). Thickness sensitivity of ultrasound velocity in long bone phantoms. *Ultrasound Med Biol* **30**, 1517–1521.

Moldoveanu-Constantinescu, C. (2006). Coherent noise attenuation using Radon techniques. Master's thesis. University of Alberta.

Naili, S., M.B. Vu, Q. Grimal, M. Talmant, C. Desceliers, C. Soize and G. Haiat (2010). Influence of viscoelastic and viscous absorption on ultrasonic wave propagation in cortical bone: Application to axial transmission. *J Acoust Soc Am* **127**, 2622–2634.

Nguyen, K.C.T., L.H. Le and E. Lou (2013). Excitation of guided waves in long bones by beam steering. *The Proceeding of 5th European Symposium on Ultrasonic Characterization of Bone* **2013**, 76–77.

Nguyen, K.C.T., L.H. Le, T.N.H.T. Tran, M.D. Sacchi and E. Lou (2014). Excitation of ultrasonic Lamb waves using a phased array system with two array probes: phantom and in-vitro bone studies. *Ultrasonics* **54**, 1178–1185.

Nguyen, V.H. and S. Naili (2011). Simulation of transient ultrasonic wave propagation in fluid-loaded heterogeneous cortical bone. *Vietnam J Mech* **33**, 225–243.

Nguyen, V.H. and S. Naili (2012). Ultrasonic wave propagation in viscoelastic cortical bone plate coupled with fluids: a spectral finite element study. *Comput Methods Biomech Biomed Engin* **1**, 1–12.

Nguyen, V.H., T.N.H.T. Tran, M.D. Sacchi, S. Naili and L.H. Le (2017). Computing dispersion curves of elastic/viscoelastic transversely-isotropic bone plates coupled with soft tissue and marrow using semi-analytical finite element (SAFE) method. *Comput Biol Med* **87**, 371–381.

Okumura, S., V.H. Nguyen, H. Taki, G. Haiat, S. Naili and T. Sato (2017). Phase velocity estimation technique based on adaptive beamforming for ultrasonic guided waves propagating along cortical long bones. *Jpn J Appl Phys* **56**, 07JF06.

Okumura, S., V.H. Nguyen, H. Taki, G. Haiat, S. Naili and T. Sato (2018). Rapid high-resolution wavenumber extraction from ultrasonic guided waves using adaptive array signal processing. *Appl Sci* **8**, 652.

Osteoporosis Canada (2018). https://osteoporosis.ca/about-the-disease/fast-facts/, accessed December 2018.

Pavlakovic, B. and M. Lowe (2001). *DISPERSE user's manual, version 2.0*. London, UK: Imperial College London.

Pawlowski, R.S. (1997). Use of the slant stack for geologic or geophysical map lineament analysis. *Geophys* **62**, 1774–1778.

Pereira, D., G. Haiat, J. Fernandes and P. Belanger (2017). Simulation of acoustic guided wave propagation in cortical bone using a semi-analytical finite element method. *J Acoust Soc Am* **141**, 2538–2547.

PharmacyPedia (2018). https://pharmacypedia.org/can-vitamin-d-help-osteoporosis/, accessed December 2018.

Phinney, R.A. and K.R. Chowdhury (1981). Transformation and analysis of record sections. *J Geophys Res* **86**, 359–377.

Pithioux, M., P. Lasaygues and P. Chabrand (2002). An alternative ultrasonic method for measuring the elastic properties of cortical bone. *J Biomech* **35**, 961–968.

Potsika, V.T., D. Polyzos and D.I. Fotiadis (2017). Computational modeling of long bone microstructure and ultrasonic evaluation of the fracture healing process. *J Serb Soc Comput Mech* **11**, 98–107.

Protopappas, V.C., D.I. Fotiadis and K.N. Malizos (2006). Guided ultrasound wave propagation in intact and healing long bones. *Ultrasound Med Biol* **32**, 693–708.

Protopappas, V.C., I.C. Kourtis, D.I. Fotiadis and K.N. Malizos (2007). Three-dimensional finite element modeling of guided ultrasound wave propagation in intact and healing long bones. *J Acoust Soc Am* **121**, 3907–3921.

Renaud, G., P. Kruizinga, D. Cassereau and P. Laugier (2018). In vivo ultrasound imaging of the bone cortex. *Phys Med Biol* **63**, 125010.

Ricker, N. (1953). The form and laws of propagation of seismic wavelets. *Geophys* **18**, 10–40.

Rose, J.L. (1999). *Ultrasonic waves in solid media*. Cambridge, NY, USA: Cambridge University Press.

Rose, J.L. (2002). A baseline and vision of ultrasonic guided wave inspection potential. *J Press Vess T* **124**, 273–282.

Rose, J.L. (2004). Ultrasonic guided waves in structural health monitoring. *Key Eng Mat* **270-273**, 14–21.

Rose, J.L. (2014). *Ultrasonic guided waves in solid media*. Cambridge, NY, USA: Cambridge University Press.

Rouze, N.C., M.H. Wang, M.L. Palmeri and K.R. Nightingale (2010). Robust estimation of time-of-flight shear wave speed using a Radon sum transformation. *IEEE Trans Ultrason Ferroelectr Freq Control* **57**, 2662–2670.

Sacchi, M.D. (1997). Reweighting strategies in seismic deconvolution. *Geophys J Int* **129**, 651–656.

Sacchi, M.D. and T.J. Ulrych (1995). High resolution velocity gathers and offset space reconstruction. *Geophys* **60**, 1169–1177.

Sacchi, M.D. and T.J. Ulrych (1996). Estimation of the discrete Fourier transform, a linear inversion approach. *Geophys* **61**, 1128–1136.

Sasso, M., G. Haiat, Y. Yamato, S. Naili and M Matsukawa (2007). Frequency dependence of ultrasonic attenuation in bovine cortical bone: an in vitro study. *Ultrasound Med Biol* **33**, 1933–1942.

Sasso, M., M. Talmant, G. Haiat, S. Naili and P. Laugier (2009). Analysis of the most energetic late arrival in axially transmitted signals in cortical bone. *IEEE Trans Ultrason Ferroelectr Freq Control* **56**, 2463–2470.

Scales, J.A., A. Gersztenkorn and S. Treitel (1988). Fast l_p solution of large, sparse, linear systems: application to seismic travel time tomography. *J Comput Phys* **75**, 314–333.

Schmidt, R.O. (1986). Multiple emitter location and signal parameter estimation. *IEEE Trans Antennas Propagat* **AP-34**, 276–280.

Sen, M. and P.L. Stoffa (1995). *Global optimization methods in geophysical inversion*. Amsterdam, The Netherlands: Elsevier Science.

Simonetti, F. and P. Cawley (2003). A guided wave technique for the characterization of highly attenuative viscoelastic materials. *J Acoust Soc Am* **114**, 158–165.

Song, X., D. Ta and W. Wang (2011). Analysis of superimposed ultrasonic guided waves in long bones by the joint approximate diagonalization of eigen-matrices algorithm. *Ultrasound Med Biol* **37**, 1704–1713.

Ta, D.A., K. Huang, W.Q. Wang, Y.Y. Wang and L.H. Le (2006*a*). Identification and analysis of multimode guided waves in tibia cortical bone. *Ultrasonics* **44**, 279–284.

Ta, D.A., W.Q. Wang, Y.Y. Wang, L.H. Le and Y.Q. Zhou (2009). Measurement of the dispersion and attenuation of cylindrical ultrasonic guided waves in long bones. *Ultrasound Med Biol* **35**, 641–652.

Ta, D.A., Z.Q. Liu and X. Liu (2006*b*). Combined spectral estimator for phase velocities of multimode Lamb waves in multilayer plates. *Ultrasonics* **44**, e1145–e1150.

Takano, K., Y. Nagatani and M. Matsukawa (2017). Simulation study of axial ultrasound transmission in heterogeneous cortical bone model. *Jpn J Appl Phys* **56**, 07JF29.

Tasinkevych, Y., J. Podhajecki, K. Falinska and J. Litniewski (2016). Simultaneous estimation of cortical bone thickness and acoustic wave velocity using a multivariable optimization approach: bone phantom and in-vitro study. *Ultrasonics* **65**, 105–112.

Tatham, R.H. (1984). Multidimensional filtering of seismic data. *Proc IEEE* **72**, 1357–1369.

Telford, W.M., L.P. Geldart and R.E. Sheriff (1990). *Applied geophysics*. New York, USA: Cambridge University Press.

Temsamani, A.B., S. Vandenplas and L.V. Biesen (2002). Surface waves investigation for ultrasonic materials characterization: theory and experimental verification. *Ultrasonics* **40**, 73–76.

Tenenhouse, A., L. Joseph, N. Kreiger, S. Poliquin, T.M. Murray, L. Blondeau, C. Berger, D.A. Hanley and J.C. Prior (2000). Estimation of the prevalence of low bone density in Canadian women and men using a population-specific DXA reference standard: the Canadian Multicentre osteoporosis study (CaMos). *Osteoporosis Int* **11**, 897–904.

Thakare, D.R., A. Abid, D. Pereira, J. Fernandes, P. Belanger and P. Rajagopal (2017). Semi-analytical finite-element modeling approach for guided wave assessment of mechanical degradation in bones. *Int Biomech* **4**, 17–27.

Tikhonov, A.N. and A.V. Goncharsky (1987). *Ill-posed problems in the natural sciences*. Moscow, Russia: MIR Publisher.

Trad, D.O., T.J. Ulrych and M.D. Sacchi (2002). Accurate interpolation with high-resolution time-variant Radon transform. *Geophys* **67**, 644–656.

Tran, T.N.H.T., K.T. Nguyen, M.D. Sacchi and L.H. Le (2014*a*). Imaging ultrasonic dispersive guided wave energy in long bones using linear Radon transform. *Ultrasound Med Biol* **40**, 2715–2727.

Tran, T.N.H.T., L. Stieglitz, Y.J. Gu and L.H. Le (2013). Analysis of ultrasonic waves propagating in a bone plate over a water half-space with and without overlying soft tissue. *Ultrasound Med Biol* **39**, 2422–2430.

Tran, T.N.H.T., L.H. Le, M.D. Sacchi and V.H. Nguyen (2018*a*). Sensitivity analysis of ultrasonic guided waves propagating in trilayered bone models: a numerical study. *Biomech Model Mechanobiol* **17**, 1269–1279.

Tran, T.N.H.T., L.H. Le, M.D. Sacchi, V.H. Nguyen and E. Lou (2014*b*). Multichannel filtering and reconstruction of ultrasonic guided wave fields using time intercept-slowness transform. *J Acoust Soc Am* **136**, 248–259.

Tran, T.N.H.T., L.H. Le, V.H. Nguyen and M.D. Sacchi (2015). Excitability of ultrasonic Lamb waves in a cortical bone plate: a simulation study. *The Proceeding of 6th European Symposium on Ultrasonic Characterization of Bone* **2015**, doi: 10.1109/ESUCB.2015.7169887.

Tran, T.N.H.T., M.D. Sacchi, D. Ta, V.H. Nguyen and L.H. Le (2018*b*). Model-based inversion of ultrasonic guided waves for cortical bone properties. *J Acoust Soc Am* **144**, 1821.

Tran, T.N.H.T., M.D. Sacchi, D. Ta, V.H. Nguyen, E. Lou and L.H. Le (2019 submitted). Nonlinear inversion of ultrasonic dispersion curves for cortical bone thickness and elastic velocities. *Ann Biomed Eng.*

Tran, T.N.H.T., M.D. Sacchi, V.H. Nguyen, D. Ta and L.H. Le (2018*c*). A nonlinear grid-search inversion for cortical bone thickness and ultrasonic velocities. *J Acoust Soc Am* **143**, 1775.

Tsuji, T., T.A. Johansen, B.O. Ruud, T. Ikeda and T. Matsuoka (2012). Surface-wave analysis for identifying unfrozen zones in subglacial sediments. *Geophys* **77**, EN17–EN27.

Turner, G. (1990). Aliasing in the τ-p transform and the removal of spatially aliased coherent noise. *Geophys* **55**, 1496–1503.

Ulrych, T.J. and M.D. Sacchi (2005). *Information-based inversion and processing with applications.* Oxford, UK: Elsevier Science.

Vallet, Q., N. Bochud, C. Chappard, P. Laugier and J.G. Minonzio (2016). In vivo characterization of cortical bone using guided waves measured by axial transmission. *IEEE Trans Ultrason Ferroelectr Freq Control* **63**, 1361–1371.

Werner, P. (2005). Knowledge about osteoporosis: assessment, correlates and outcomes. *Osteoporosis Int* **16**, 115–127.

Wikipedia (2018). https://en.wikipedia.org/wiki/Dual-energy_X-ray_absorptiometry, accessed December 2018.

Wiktorowicz, M.E., R. Goeree, A. Papaioannou, J.D. Adachi and E. Papadimitropoulos (2001). Economic implications of hip fracture: health service use, institutional care and cost in Canada. *Osteoporosis Int* **12**, 271–278.

Wilson, C. and A. Guitton (2007). Teleseismic wavefield interpolation and signal extraction using high-resolution linear Radon transforms. *Geophys J Int* **168**, 171–181.

World Health Organisation (1994). Assessment of fracture risk and its implication to screening for postmenopausal osteoporosis: WHO Technical report series No 843.

Xu, K., D. Ta and W. Wang (2010). Multiridge-based analysis for separating individual modes from multimodal guided wave signals in long bones. *IEEE Trans Ultrason Ferroelectr Freq Control* **57**, 2480–2490.

Xu, K., D. Ta, B. Hu, P. Laugier and W. Wang (2014). Wideband dispersion reversal of Lamb waves. *IEEE Trans Ultrason Ferroelectr Freq Control* **61**, 997–1005.

Xu, K., D. Ta, P. Moilanen and W. Wang (2012). Mode separation of Lamb waves based on dispersion compensation method. *J Acoust Soc Am* **131**, 2714–2722.

Xu, K., J. Minonzio and P. Laugier (2018). Dispersive Radon transform. *J Acoust Soc Am* **143**, 2729–2743.

Xu, K., J. Minonzio, D. Ta, B. Hu, W. Wang and P. Laugier (2016). Sparse SVD method for high-resolution extraction of the dispersion curves of ultrasonic guided waves. *IEEE Trans Ultrason Ferroelectr Freq Control* **63**, 1514–1524.

Yapura, D.L. and V.K. Kinra (1995). Guided waves in a fluid-solid bilayer. *Wave Motion* **21**, 35–46.

Yeh, C.H. and C.H. Yang (2011). Characterization and mechanical and geometrical properties of a tube with axial and circumferential guided waves. *Ultrasonics* **51**, 472–479.

Zhang, Z., K. Xu, D. Ta and W. Wang (2013). Joint spectrogram segmentation and ridge-extraction method for separating multimodal guided waves in long bones. *Sci China Phys Mech* **56**, 1317–1323.

Zheng, R., L.H. Le, M.D. Sacchi and E. Lou (2015). Imaging internal structure of long bones using wave scattering theory. *Ultrasound Med Biol* **41**, 2955–2965.

Zheng, R., L.H. Le, M.D. Sacchi, D.A. Ta and E. Lou (2007). Spectral ratio method to estimate broadband ultrasound attenuation of cortical bones in vitro using multiple reflections. *Phys Med Biol* **52**, 5855–5869.

Zou, D.H. and Y. Cui (2011). A new approach for field instrumentation in grouted rock bolt using guided ultrasonic waves. *J Appl Geophys* **75**, 506–512.

Appendix A: High-Resolution Radon Solution by Iteratively Re-Weighted Least-Squares Method

I would like to compute the Radon solution $\mathbf{M}$ via Equation 3.9, which is

$$\mathbf{M} = (\mathbf{L}^H\mathbf{L} + \mu\mathbf{Q}(\mathbf{M}))^{-1}\mathbf{L}^H\mathbf{D} \tag{A.1}$$

where $\mathbf{Q}$ is a diagonal matrix with elements

$$Q_{kk} = \frac{1}{(1 + (M_k)^2/\sigma^2)}. \tag{A.2}$$

Using the IRLS algorithm (Scales *et al.*, 1988; Daubechies *et al.*, 2010), the solution at the j^{th} iteration, $\mathbf{M}_j$, can be estimated using the previous iteration of $\mathbf{Q}$, that is, $\mathbf{Q}_{j-1}$,

$$\mathbf{M}_j = (\mathbf{L}^H\mathbf{L} + \mu\mathbf{Q}_{j-1})^{-1}\mathbf{L}^H\mathbf{D}. \tag{A.3}$$

The initial weighting matrix $\mathbf{Q}_0$ is calculated by

$$Q_{0,kk} = \frac{1}{(1 + (M_{0,k})^2/\sigma^2)} \tag{A.4}$$

where the damped least-squares solution provides the initial estimate of $\mathbf{M}_0$,

$$\mathbf{M}_0 = (\mathbf{L}^H\mathbf{L} + \mu\mathbf{I})^{-1}\mathbf{L}^H\mathbf{D}. \tag{A.5}$$

For example,

$$\mathbf{M}_1 = (\mathbf{L}^H\mathbf{L} + \mu\mathbf{Q}_0)^{-1}\mathbf{L}^H\mathbf{D}. \tag{A.6}$$

The iteration stops at a preset number or the convergence is reached at a preset tolerance limit.

The HRRT algorithm is as follow:

procedure RADON($\mathbf{d}$,$\mathbf{x}$,$\mathbf{p}$,μ,σ,n)
  $\mathbf{D}(f,x) = \text{fft}(\mathbf{d}(t,x))$
  for $f = f_{min}$, ..., f_{max} **do**
    $\mathbf{L} = \exp(-i2\pi f \mathbf{x}^T \mathbf{p})$
    $\mathbf{M}_0(f,:) = (\mathbf{L}^H\mathbf{L} + \mu\mathbf{I})^{-1}\mathbf{L}^H\mathbf{D}(f,:)$
    for $j = 1$, ..., n **do**
      $$Q_{j-1,kk} = \frac{1}{(1 + (M_{j-1}(f,k))^2/\sigma^2)}$$
      $\mathbf{M}_j(f,:) = (\mathbf{L}^H\mathbf{L} + \mu\mathbf{Q}_{j-1})^{-1}\mathbf{L}^H\mathbf{D}(f,:)$
    end for(j)
  end for(f)
  Return $\mathbf{M}_{\text{HR}} = \mathbf{M}_n$
end procedure

Appendix B: The Semi-Analytical Finite Element Formulation

B.1 Weak Formulation

In the fluid layers The weak formulation (Hughes, 2000) for the acoustic equation (Equation 4.9) in the soft tissue domain is given by

$$\int_0^{h_1} \delta p_1^*(-\omega^2\rho_1 + k_1^2\bar{K}_1)\tilde{p}_1 dx_2 + \int_0^{h_1} \partial_2\delta p_1^*\bar{K}_1\partial_2\tilde{p}_1 dx_2 - \left[\delta p_1^*\bar{K}_1\partial_2\tilde{p}_1\right]_0^{h_1} = 0 \tag{B.1}$$

where δp_1^* is a test function. By applying the boundary conditions and noting that $\bar{\rho}_1\bar{K}_1 = \rho_1 K_1$, the last term may be calculated by:

$$-\left[\delta p_1^*\bar{K}_1\partial_2\tilde{p}_1\right]_0^{h_1} = \rho_1 K_1\omega^2\delta p_1^*(0)\tilde{u}_2(0). \tag{B.2}$$

Similarly, the weak formulation in the marrow domain for a test function δp_2^* is

$$\int_{-(h_2+h)}^{-h} \delta p_2^*(-\omega^2\rho_2 + k_1^2\bar{K}_2)\tilde{p}_2 dx_2 + \int_{-(h_2+h)}^{-h} \partial_2\delta p_2^*\bar{K}_2\partial_2\tilde{p}_2 dx_2 - \left[\delta p_2^*\bar{K}_2\partial_2\tilde{p}_2\right]_{-(h_2+h)}^{-h} = 0 \tag{B.3}$$

where

$$-\left[\delta p_2^*\bar{K}_2\partial_2\tilde{p}_2\right]_{-(h_2+h)}^{-h} = -\rho_2 K_2\omega^2\delta p_2^*(-h)\tilde{u}_2(-h). \tag{B.4}$$

In the solid layer Upon integrating the Equation 4.13 by parts against a test function $\delta\tilde{\mathbf{u}}^*$, the following is obtained

$$\begin{aligned}\int_{-h}^{0} \delta\tilde{\mathbf{u}}^*\left(-\omega^2\mathbf{A}_1 + k_1^2\mathbf{A}_2 - \mathrm{i}k_1\mathbf{A}_3^T\partial_2\right)\tilde{\mathbf{u}}\, dx_2 + \int_{-h}^{0} \partial_2\delta\tilde{\mathbf{u}}^*\tilde{\mathbf{t}} dx_2 \\ - \left[\delta\tilde{\mathbf{u}}^*\tilde{\mathbf{t}}\right]_{-h}^{0} = 0.\end{aligned} \tag{B.5}$$

where the last term may be calculated by using the condition at interfaces:

$$-\left[\delta\tilde{\mathbf{u}}^*\tilde{\mathbf{t}}\right]_{-h}^{0} = -(1-\mathrm{i}\omega\gamma_1)\delta u_2^*(0)\tilde{p}_1(0) + (1-\mathrm{i}\omega\gamma_2)\delta u_2^*(-h)\tilde{p}_2(-h) \tag{B.6}$$

B.2 Finite Element Formulation

We proceed by placing a finite element mesh in the domain $[-(h_2+h), h_1]$, which contains n_{el} elements Ω_e: $[-(h_2+h), h_1] = \bigcup_e \Omega_e$ $(e = 1...n_{el})$. For this problem, the Galerkin finite element method (Hughes, 2000) using linear elements has been employed. In each element e, the functions $\tilde{p}_\alpha$, $\delta\tilde{p}_\alpha$ $(\alpha = 1, 2)$ and $\tilde{\mathbf{u}}$, $\delta\tilde{\mathbf{u}}$ are approximated by

$$\tilde{p}_\alpha(x_2) = \mathbf{N}_e^f \mathbf{P}_\alpha^e, \quad \delta\tilde{p}_\alpha(x_2) = \mathbf{N}_e^f \delta\mathbf{P}_\alpha^e, \quad (\alpha = 1, 2) \tag{B.7}$$

$$\tilde{\mathbf{u}}(x_2) = \mathbf{N}_e^b \mathbf{U}^e, \quad \delta\tilde{\mathbf{u}}(x_2) = \mathbf{N}_e^b \delta\mathbf{U}^e, \tag{B.8}$$

where $\mathbf{N}_e^f$ and $\mathbf{N}_e^b$ are the shape functions of $\tilde{p}_\alpha$ and of $\tilde{\mathbf{u}}$, respectively; $\mathbf{P}_\alpha^e$, $\delta\mathbf{P}_\alpha^e$ $(\alpha = 1, 2)$ and $\mathbf{U}^e$, $\delta\mathbf{U}^e$ are the nodal solution vectors. Replacing (A.7), (A.8), (A.9) into (A.1), (A.3), (A.5) and assembling the elementary matrices, a linear system of equations can be obtained

$$\begin{bmatrix} \mathbf{K}^{f_2} & \mathbf{K}^{f_2 b} & \mathbf{0} \\ \mathbf{K}^{b f_2} & \mathbf{K}^{b} & \mathbf{K}^{b f_1} \\ \mathbf{0} & \mathbf{K}^{f_1 b} & \mathbf{K}^{f_1} \end{bmatrix} \begin{pmatrix} \mathbf{P}_2 \\ \mathbf{U} \\ \mathbf{P}_1 \end{pmatrix} = \mathbf{0} \tag{B.9}$$

where $\mathbf{U}$ is the global nodal displacement vector,$\mathbf{P}_\alpha$ is the global nodal pressure vector, and

$$\mathbf{K}^{f_\alpha} = -\omega^2 \mathbf{K}_1^{f_\alpha} + k_1^2 \mathbf{K}_2^{f_\alpha} + \mathbf{K}_4^{f_\alpha}, \quad (\alpha = 1, 2) \tag{B.10}$$

$$\mathbf{K}^{b} = -\omega^2 \mathbf{K}_1^{b} + k_1^2 \mathbf{K}_2^{b} + \mathrm{i} k_1 \mathbf{K}_3^{b} + \mathbf{K}_4^{b}. \tag{B.11}$$

The matrices $\mathbf{K}$ are defined by

$$\mathbf{K}_1^{f_\alpha} = \bigcup_e \int_{\Omega_e} \rho_\alpha (\mathbf{N}_e^f)^T \mathbf{N}_e^b \, dx_2, \quad \mathbf{K}_2^{f_\alpha} = \bigcup_e \int_{\Omega_e} \bar{K}_\alpha (\mathbf{N}_e^b)^T \mathbf{N}_e^b \, dx_2, \tag{B.12}$$

$$\mathbf{K}_4^{f_\alpha} = \bigcup_e \int_{\Omega_e} K_\alpha (\mathbf{B}_e^f)^T \mathbf{B}_e^f \, dx_2, \tag{B.13}$$

$$\mathbf{K}_1^{b} = \bigcup_e \int_{\Omega_e} (\mathbf{N}_e^b)^T \mathbf{A}_1 \mathbf{N}_e^b \, dx_2, \quad \mathbf{K}_2^{b} = \bigcup_e \int_{\Omega_e} (\mathbf{N}_e^b)^T \mathbf{A}_2^e \mathbf{N}_e^b \, dx_2, \tag{B.14}$$

$$\mathbf{K}_3^{b} = \bigcup_e \int_{\Omega_e} 2 \left\{ (\mathbf{B}_e^b)^T \mathbf{A}_3^e \mathbf{N}_e \right\}_a dx_2, \quad \mathbf{K}_4^{b} = \bigcup_e \int_{\Omega_e} (\mathbf{B}_e^b)^T \mathbf{A}_4^e \mathbf{B}_e^b \, dx_2, \tag{B.15}$$

in which the notation $\{.\}_a$ is devoted for the anti-symmetric part of the $\{.\}$ and $\mathbf{B}_e^{b,f} = \partial_2 \mathbf{N}_e^{b,f}$. The matrices $\mathbf{K}^{f_1 b}$, $\mathbf{K}^{b f_1}$, $\mathbf{K}^{f_2 b}$, $\mathbf{K}^{b f_2}$ represent the coupled terms between the solid and the fluids. These matrices have only one non-zero elements, which are respectively

$$\left(\mathbf{K}^{f_1 b}\right)_{mn} = \rho_1 K_1, \quad \left(\mathbf{K}^{f_2 b}\right)_{mn} = -\rho_2 K_2, \tag{B.16}$$

$$\left(\mathbf{K}^{b f_1}\right)_{mn} = -(1 - i\omega\gamma_1), \quad \left(\mathbf{K}^{b f_2}\right)_{mn} = (1 - i\omega\gamma_2), \tag{B.17}$$

where m and n are the indices of the degrees of freedom, which are concerned by the continuity conditions.

By noting that all matrices $\mathbf{K}$ described above do not depend on k_1, the equation (B.9) may be represented by

$$\left[\mathbf{K}_1 + k_1^2\mathbf{K}_2 + \mathrm{i}k_1\mathbf{K}_3\right]\mathbf{V} = \mathbf{0} \tag{B.18}$$

where $\mathbf{V} = (\mathbf{P}_2, \mathbf{U}, \mathbf{P}_1)^T$ and

$$\mathbf{K}_1 = \begin{bmatrix} -\omega^2\mathbf{K}_1^{f_2} + \mathbf{K}_4^{f_2} & \mathbf{K}_2^{f_2 b} & \mathbf{0} \\ \mathbf{K}^{bf_2} & -\omega^2\mathbf{K}_1^{b} + \mathbf{K}_4^{b} & \mathbf{K}^{bf_1} \\ \mathbf{0} & \mathbf{K}^{f_1 b} & -\omega^2\mathbf{K}_1^{f_1} + \mathbf{K}_4^{f_1} \end{bmatrix}, \tag{B.19}$$

$$\mathbf{K}_2 = \begin{bmatrix} \mathbf{K}_2^{f_2} & \mathbf{0} & \mathbf{0} \\ \mathbf{0} & \mathbf{K}_2^{b} & \mathbf{0} \\ \mathbf{0} & \mathbf{0} & \mathbf{K}_1^{f_1} \end{bmatrix}, \quad \mathbf{K}_3 = \begin{bmatrix} \mathbf{0} & \mathbf{0} & \mathbf{0} \\ \mathbf{0} & \mathbf{K}_3^{b} & \mathbf{0} \\ \mathbf{0} & \mathbf{0} & \mathbf{0} \end{bmatrix}. \tag{B.20}$$